GRANT AGREEMENT No.: 764902 **Project Acronym: TOMOCON** **Project title: Smart tomographic sensors for advanced industrial process control**	TOMOCON Smart Tomographic Sensors for Advanced Industrial Process Control	
Deliverable Rel. No. **D5.4.**	Lead Beneficiary **TUD**	
EU Del. No. **D18**	Type **Report**	
WP No. **WP5**	Date: **15.10.2021**	Revision: **0**

Innovative Training Network

TOMOCON

Deliverable Title

Lab Demonstration Results

Description

This deliverable is a complete description of the results of the lab-scale demonstrations for all four demonstration cases.

Prepared by:	Susann Riedel / Dr. Luis Portela	S. Riedel / Luis Portela
Approved by:	Prof. Dr. Uwe Hampel	Uwe Hampel
Approved by Supervisory Board:		29.10.2021

Dissemination Level: **Public**

This project has received funding from the European Union's Horizon 2020 research and innovation programme under the Marie Skłodowska-Curie Grant Agreement No. 764902.

Revision Sheet

Revision Number	Purpose of Revision	Effective Date
0	Initial Issue	29.10.2021

Dissemination Level: **Public**

This project has received funding from the European Union's Horizon 2020 research and innovation programme under the Marie Skłodowska-Curie Grant Agreement No. 764902.

Table of Contents

1. Tomography-Controlled Inline Fluid Separation 5
   1.1. Introduction 5
      1.1.1. Application background 5
      1.1.2. Working principle of a controlled inline swirl separator 6
   1.2. Experimental setup 7
      1.2.1. Flow facility 7
      1.2.2. Control loop sensors 10
      1.2.3. Generation of disturbances 10
      1.2.4. Flow conditions 11
   1.3. Wire-mesh sensor results 11
   1.4. Electrical resistance tomography results 12
   1.5. Controller results 13
      1.5.1. Bang-bang (on-off) implementation 13
      1.5.2. PI controller 16
   1.6. Conclusions and perspective 18
   1.7. References 19
2. Tomography-Controlled Microwave Drying 20
   2.1. Objectives 20
   2.2. Experimental facility 20
   2.3. Microwave tomography sensor 21
   2.4. Electrical capacitance sensor 22
   2.5. Control Unit 23
      2.5.1. Closed-loop control structure 23
      2.5.2. Modelling and system identification 24
      2.5.3. Control methods 26
   2.6. Augmented Reality 28
      2.6.1. The AR application 28
   2.7. Results of the lab demo 30
      2.7.1. MWT sensor 30
      2.7.2. ECT sensor 30
      2.7.3. Process model 31
      2.7.4. Controller 33

This project has received funding from the European Union's Horizon 2020 research and innovation programme under the Marie Skłodowska-Curie Grant Agreement No. 764902.

2.7.5. Comparing response of the controlled and uncontrolled microwave drying process 36
2.8. Conclusions and outlook 38
2.9. References....40
3. Tomography-Controlled Continuous Casting 42
3.1. Objectives 42
3.2. Laboratory setup 43
3.3. Contactless inductive flow tomography....44
3.4. Mutual inductance tomography....49
3.5. Control strategies 54
3.6. Results....56
3.7. Conclusions and outlook 59
3.8. References....60
4. Tomography-Controlled Batch Crystallization....61
4.1. Objectives 61
4.2. Experimental facility 61
4.3. ERT....63
4.4. USCT 65
4.5. Control 66
4.5.1. ERT-based process automation implementation for malfunction identification 66
4.6. Results of the lab demo....68
4.6.1. ERT sensitivity analysis and sensor selection....68
4.6.2. Measurements of $CaCO_3$ solid particles addition by ERT electrodes 72
4.6.3. ERT-based malfunction identification....73
4.6.4. Ultrasound tomography: Application of USCT to detect particle beads 80
4.6.5. Characterizing $CaCO_3$ solid particles distribution by USCT 83
4.6.6. Quantification of particle settling time by USCT measurement....85
4.6.7. USCT-based tomographic analysis of the calcium carbonate crystallization process 86
4.7. Conclusions and outlook 89
4.8. References....90

This project has received funding from the European Union's Horizon 2020 research and innovation programme under the Marie Skłodowska-Curie Grant Agreement No. 764902.

1. Tomography-Controlled Inline Fluid Separation

1.1. Introduction

1.1.1. Application background

Cyclones and inline swirl separators are widely applied in the oil industry to separate oil from water, either in the platform to clean the water extracted from the well before disposing it in the ocean, or in downhole applications, where the mixture is separated close to the well in the seabed cutting down costs related to water production (pumping and separation in the platform). Illustrations of the two devices are presented in Fig. 1.

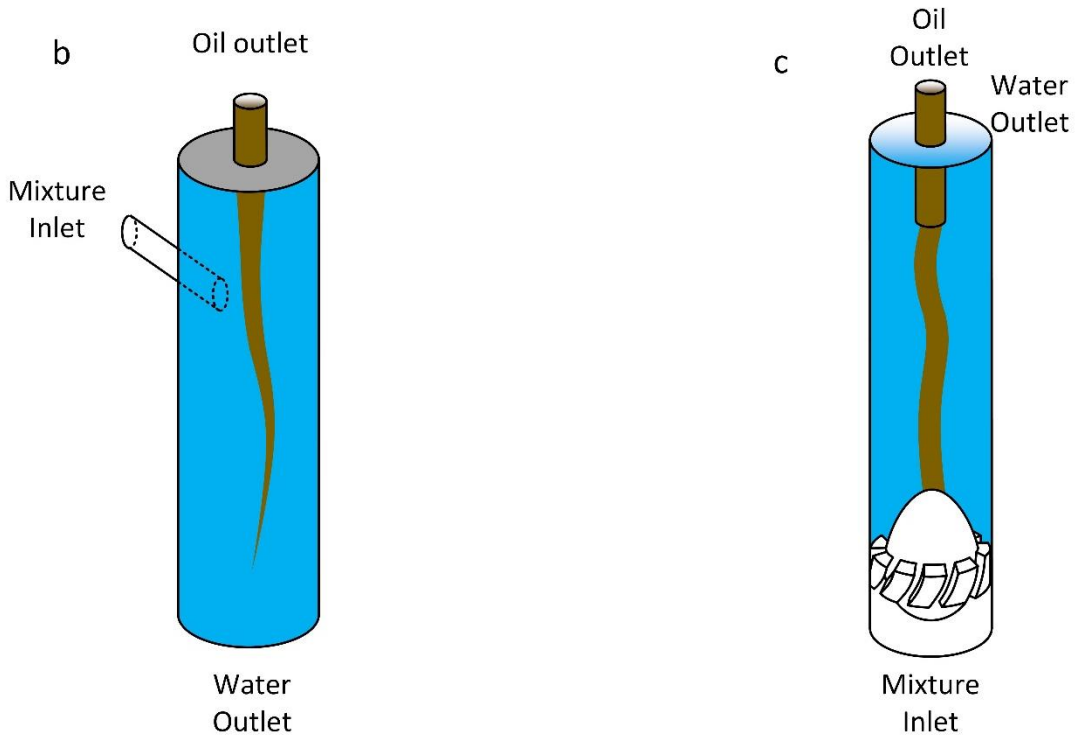

Fig. 1: Oil water cylindrical cyclone (left), Inline swirl separator (right)

Naturally, controllers are applied to the separators to reject disturbances in the upcoming flow and to keep the production stable. So far, the approach found in literature for the control of hydrocyclones is based on the so-called pressure drop ratio, a quantity defined as the ratio between the pressure difference between the oil outlet and the injection and the pressure difference between the water outlet and the injection:

$$PDR = \frac{P_{inj} - P_{oil}}{P_{inj} - P_{water}}, \tag{1}$$

with a reference value for optimal operation between 1.7 and 2 [1].

Dissemination Level: **Public**

This project has received funding from the European Union's Horizon 2020 research and innovation programme under the Marie Skłodowska-Curie Grant Agreement No. 764902.

Although the pressure drop ratio represents the flow split between the two outlets, which is connected to some degree to the separator performance, the use of a pressure drop ratio does not tell with precision about the distribution of fluids inside the equipment, that is deeply connected to its efficiency. For instance, changes in the flow rates of oil and/or water will result in a different oil core size and shape, that will cause a different capture of oil by the pickup tube (oil outlet in Fig. 1) and can impact the performance of the equipment even if the pressure drop ratio is the same. Therefore, a natural parameter to monitor in the device is the distribution of fluids inside the swirl separator, in particular the oil core size and position.

Real-time applications of soft-field tomography can become a reality thanks to the recent progresses in computation power and, in the context of the problem, provide an output of the distribution of fluids inside the device for control applications. The Inline Fluid Separation team of TOMOCON had the following objectives along the past years:

I. Introduce tomography to the context of inline fluid separation.
II. Develop an online wire-mesh sensor to be used in control applications.
III. Develop fast and reliable Electrical Resistance Tomography algorithms to monitor the separation inside cyclones.
IV. Evaluate the use of tomography in the control of an inline swirl separator in terms of tracking the core.
V. Evaluate the impact of the controller in the efficiency of the equipment.

1.1.2. Working principle of a controlled inline swirl separator

The inline swirl separator (Fig. 1, right) relies on centrifugal effects to separate the upcoming mixture. The mixture of fluids of different densities is forced to rotate when crossing the swirl element, which pushes the lighter phase to the center of the domain, creating a continuous core, and the heavier phase towards the wall, creating an annulus. In oil-water separation, the formed annulus is dominated by water and the core by oil.

Dissemination Level: **Public**

This project has received funding from the European Union's Horizon 2020 research and innovation programme under the Marie Skłodowska-Curie Grant Agreement No. 764902.

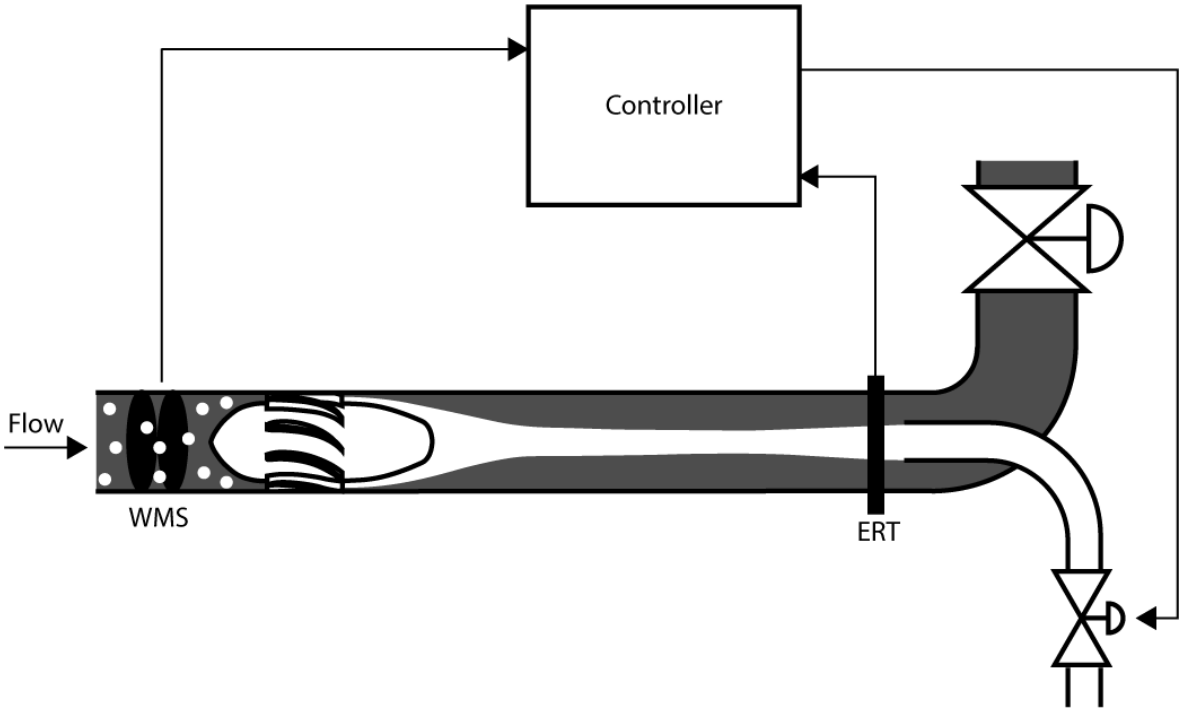

Fig. 2: Schematic drawing of the controlled inline swirl separator

At the end of the device a pickup tube is used to capture the oil (referred in Fig. 1 as oil outlet) and the water flows to the water outlet (or outer tube). Some back pressure has to be applied in one of the two outlets to force the flow to bend to a specific direction, which is performed by valves placed individually at the location (Fig. 2), leading to different values of PDR.

When introducing tomography to the context of the problem, i.e. the ability to see the distribution of fluids in a cross-section of the flow, a natural indicative of performance is the size and position of the light-phase core created by the swirl. Such core is going to be properly captured if it is centered and around the same diameter of the pickup tube; if it is bigger than the pickup tube, the water stream will be contaminated with oil and if it smaller than the pickup tube, a lot of water will be captured by the oil outlet. Both conditions are bad in terms of separation by definition.

As shown in Fig. 2, a controller based on the Electrical Resistance Tomography (ERT) and Wire-Mesh (WMS) sensors can be used to adjust the valves in real time to keep the core size stable. In this report, results of each sensor are presented in terms of predicting (WMS) or monitoring (ERT) the core, and two controllers are presented connecting the pickup tube valve to the core size measured by the ERT.

1.2. Experimental setup

1.2.1. Flow facility

This subsection summarizes the flow facility at TU Delft used in the implementation of the proof of concept controller. Other facilities at HZDR and TU Lodz were also used along the project, and were fundamental in the development of the online Electrical Resistance Tomog-

Dissemination Level: **Public**

This project has received funding from the European Union's Horizon 2020 research and innovation programme under the Marie Skłodowska-Curie Grant Agreement No. 764902.

raphy (ERT) and online Wire-Mesh Sensor (WMS). Details about those facilities can be found in [2,3,4].

The flow loop built at TU Delft consists mainly of DN80 transparent PVC pipelines. It operates with air-water flows, chosen due to the simplicity in working with the fluids in comparison to the original oil-water application. The facility can operate with water flow rates up to 350 L/min ($V_{sl} = 1.3$m/s) and gas flow rates up to 1000 Ln/min ($V_{sg} = 3.3$ m/s at atmospheric conditions). The range covers bubbly, slug and churn flows upstream the swirl element.

Fig. 3 presents the most important section of the loop. A section of 2.73 m is present after the injection of air, which allows the development of the gas-liquid flow patterns before the inline swirl separator. The swirl elements available are DN100 and placed in an expansion-contraction section. An illustration of the four swirl elements available is presented in Fig. 4, where the intensity of the generated swirl increases from the left to the right.

The swirl flow takes place in a region of 1.3 m before the pickup tube captures the air at the center of the equipment, and the swirl is killed in the water outlet by a flow straightener. The valves installed in each of the outlets are pneumatic Stübbe MV 310 diaphragm valves, where the pickup tube valve is DN25 and the outer tube valve is DN50. Details about their behavior were provided in D4.3.

Each outlet is connected to a gravity tank where the water level is controlled. The water and air outflow of each of the tanks is measured via flowmeters, which allow calculating the efficiency of separation achieved by the device, defined in this work as:

$$\eta_{air} = \frac{q_{air,pt}}{q_{air,inj}} \quad (2)$$

$$\eta_{water} = \frac{1-q_{water,pt}}{q_{water,inj}} \quad (3)$$

Dissemination Level: **Public**

This project has received funding from the European Union's Horizon 2020 research and innovation programme under the Marie Skłodowska-Curie Grant Agreement No. 764902.

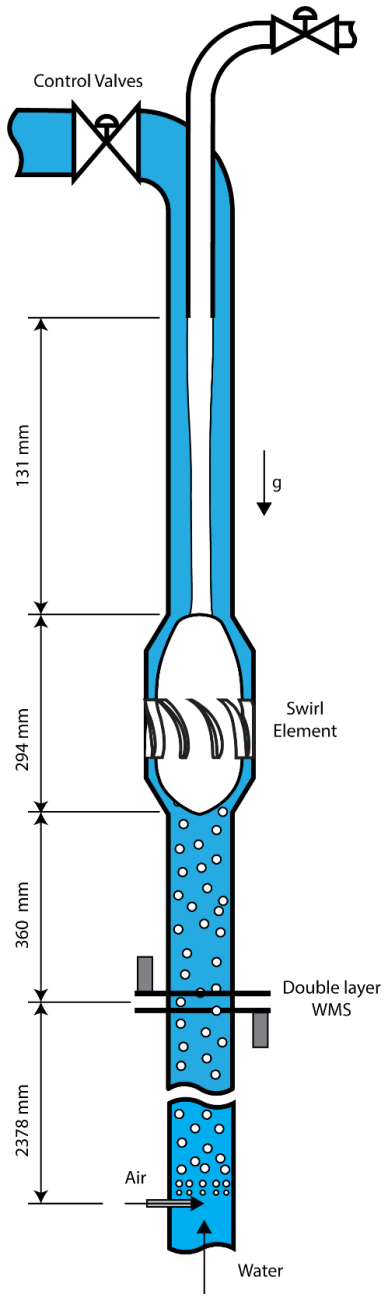

Fig. 3: Main dimensions of the inline swirl separator installed at Delft University of Technology

Dissemination Level: **Public**

This project has received funding from the European Union's Horizon 2020 research and innovation programme under the Marie Skłodowska-Curie Grant Agreement No. 764902.

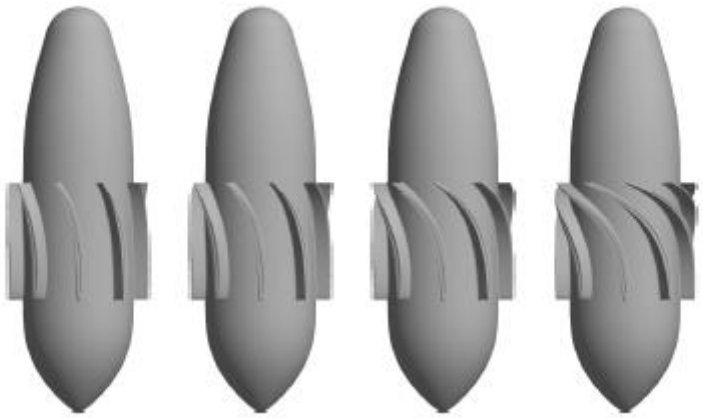

Fig. 4: Swirl elements available [5]. The blade angles are, from left to right: 40.2º, 51.5º, 63.1º and 73º.

1.2.2. Control loop sensors

The loop is monitored by pressure gauges and flowmeters, that allow computing the efficiency of the system and the PDR. Moreover, since the pipelines are transparent, visualization techniques can be applied in the system.

Focusing on the monitoring devices connected to the controller, an online version of the wire-mesh sensor with 2x16x16 grids and a 16-electrodes ERT system was developed by ESRs 1 and 10, respectively (D2.4). The wire-mesh sensor is placed 30 cm upstream the swirl element and the ERT is placed as close as possible to the pickup tube, at around 10 cm from its tip.

Both sensors communicate with the LabVIEW code that controls the flow loop via the UDP protocol. The ERT is set to measure the core size at a frequency of 10 Hz and the wire-mesh sensor operates sending the average void fraction upstream the separator at a frequency of 20 Hz. More details about the devices can be found in Deliverable 2.4.

1.2.3. Generation of disturbances

To disturb the process inputs in the liquid and gas flow rates can be performed, which acts in the order of seconds due to the inertia of the pump and to the output filter of the mass flow controller. Such disturbances are referred to in the context of this report as extrinsic, meaning that they come from changes in the whole flow of the system.

If the response of the system is sufficiently fast, an attempt to control the oscillations present in the gas-liquid flow patterns can be made. In this context, the disturbances are referred to as intrinsic, meaning that they occur even if the flow conditions are nominally the same. This is the case of slug flows, for instance, where the mixture is distributed between Taylor bubbles (with a large amount of air) and liquid slugs (with little air) for a fixed flow rate, and this quasi-periodic oscillations impact the behavior of the gas core, such that it can be seen as a disturbance (in relation to the average amount of air/gas core size).

When considering the intrinsic control, such perturbations (typically dominant for frequencies in the order of Hz) must be filtered out in order to keep the control actions effective. This is achieved in this report via a low pass filter, with a time constant of 1s:

Dissemination Level: **Public**

This project has received funding from the European Union's Horizon 2020 research and innovation programme under the Marie Skłodowska-Curie Grant Agreement No. 764902.

$$F(s) = \frac{1}{s+1} \tag{4}$$

1.2.4. Flow conditions

Due to the fact that the measurements of the ERT system take place at the wall of the pipeline, far from the location where the gas core typically is, there is a limitation in the size of the gas core created inside the separator that the technique can see, i.e. the gas core has to be sufficiently large to be detected by the sensor.

Such large cores require the injection of high quantities of air in the system (from conservation of mass), which only occur for slug and churn flows. This causes the core to be unstable, and continuously oscillate. After some tests, optimal operating conditions were achieved for:

I. $V_{sl} = 0.48$m/s and $V_{sg} = 0.13$m/s
II. $V_{sl} = 0.40$m/s and $V_{sg} = 0.20$m/s

which corresponds in both cases to churn flows (around the slug transition).

1.3. Wire-mesh sensor results

The wire-mesh sensor measures the flow upstream the swirl element. It was successfully implemented to send the average of 500 measurements of void fraction originally achieved at 10 kHz, leading to an output of around 20 Hz.

It was observed in the past that there is a strong connection between the core size and the void fraction upstream the swirl element [6], which comes simply from the conservation of mass; the higher the amount of air that comes to the device, the wider the core size. The relation not only holds for the average void fraction as explored in [6], but also for instantaneous measurements where the gas core in the swirling section is strongly correlated with the upstream void fraction, as presented in Fig. 5.

The delay in the cross correlation of Fig. 5 is deeply connected to convection: The fluctuations in the amount of air that crosses the upstream region takes some time to reach the pickup tube, where it is detected by a camera that measures the core size in this experiment. Therefore, it was observed that the higher the mixture velocity the lower the delay between the two signals, and the peak of the cross-correlation moves towards 0. The results achieved with the wire-mesh sensor allow for two main conclusions:

i. The core size fluctuations can be predicted from the upstream measurements of void fraction, and used in a predictor inside the controller (either as a feedforward term or inside an MPC structure).
ii. The knowledge of the velocity in which the flow moves is fundamental in the prediction of the core size, and it can be measured by a double layer wire-mesh sensor. From partial results the approach seems to get unstable at high frequencies and the velocity is limited to a measurement in the order of seconds.

Dissemination Level: **Public**

This project has received funding from the European Union's Horizon 2020 research and innovation programme under the Marie Skłodowska-Curie Grant Agreement No. 764902.

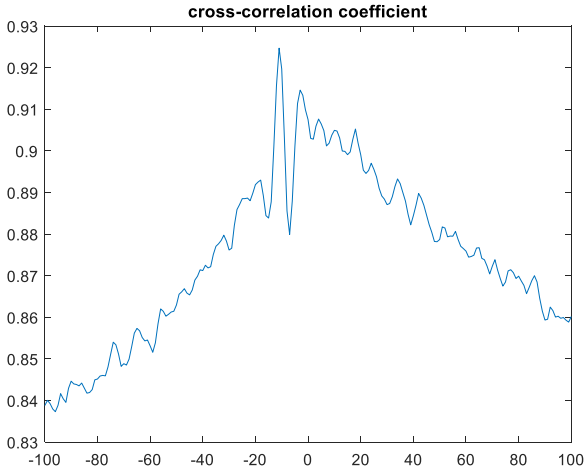

Fig. 5: Cross-correlation coefficient between the core and the WMS. The peak at -11 indicates a lag of 0.55 s.

1.4. Electrical resistance tomography results

A special algorithm was developed for the ERT system focusing on the IFS application, after realizing that the 4 Hz of the previous approach [2] was not enough for the application, especially when targeting the measurement of intrinsic disturbances. It works by analyzing the raw data of current measured by the device to reconstruct based on logic and physics the core size and position. Due to its simplicity, this fast algorithm allowed the device to operate at above 10 Hz [3].

The algorithm is calibrated against phantoms, that generates a polynomial curve between the phantom size and the mean electric current measured by the device. When compared to a camera, the ERT shows a very good match both in the time-series and spectra, as presented in Fig. 6 and 7.

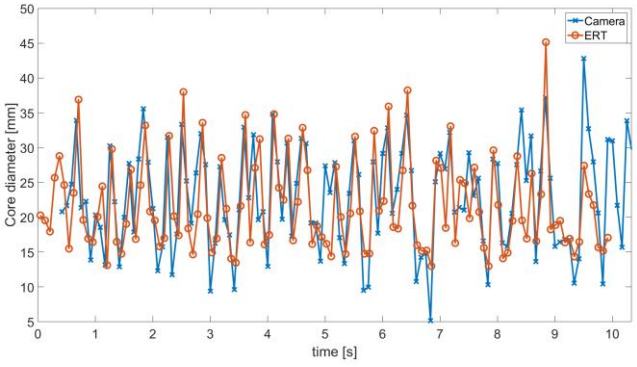

Fig. 6: ERT and camera time series measured during the same experiment

Dissemination Level: **Public**

This project has received funding from the European Union's Horizon 2020 research and innovation programme under the Marie Skłodowska-Curie Grant Agreement No. 764902.

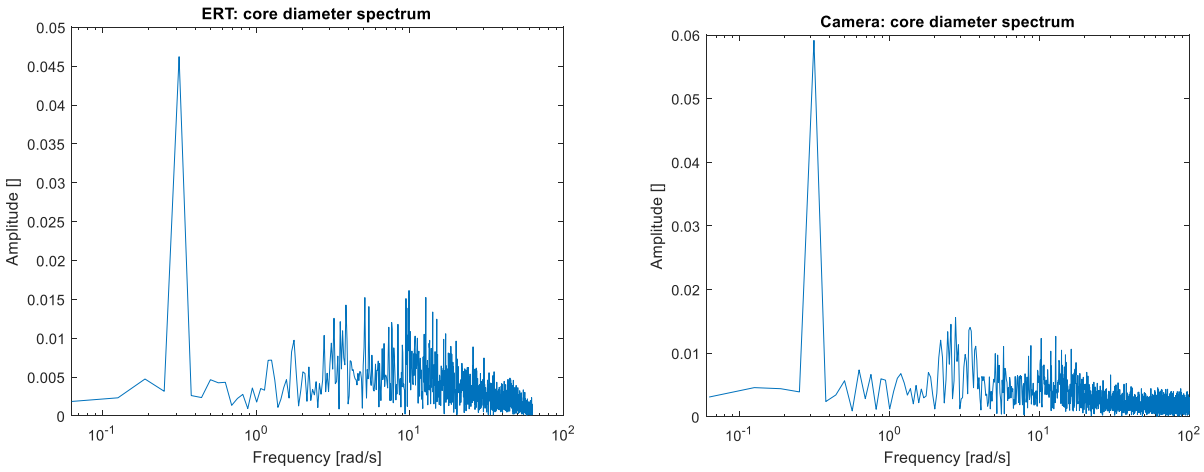

Fig. 7: ERT (left) and camera (right) spectra of the core when acting at 0.01 Hz on the valve. Data for distinct experiments at the same conditions.

When further extending the analysis to the Bode plots of the camera and the ERT for the same actions of the valve, a latency of 0.2 s in the ERT signal is observed when compared to the camera, most likely due to the several data transfers that occur in the process of measurement. This can be improved in future works by improving the data transfer between the device and the controller.

1.5. Controller results

Two controllers were implemented in the loop, a bang-bang controller and a PI controller. This report initially focuses on the bang-bang results, and later describes the results achieved with the PI controller.

1.5.1. Bang-bang (on-off) implementation

To illustrate the potential of the approach, a bang-bang controller was implemented considering the flow conditions of $V_{sl} = 0.48$m/s and $V_{sg} = 0.13$m/s and $V_{sl} = 0.48$m/s and $V_{sg} = 0.27$m/s. It is implemented in two steps: i) Finding the settings that maximize the efficiency for two nominal flow rates of air and water, ii) Checking the ERT size during this behavior and iii) Implementing a switch based on the ERT signal.

Choice of the two states of the switch

Setting the condition of $V_{sl} = 0.48$m/s and $V_{sg} = 0.13$m/s as reference, the efficiency of separation is maximized when the valve is at around 50 % of the maximum input, where 0 corresponds to the valve fully open and 100 % to fully closed. Fig. 8 presents the air and water efficiencies as a function of the input to the valve, and it can be seen that the amount of air captured by the pickup tube decays as the pickup tube valve closes, causing the efficiency to decay, while the amount of water captured by the pickup tube decays as the valve closes, causing the increase in efficiency observed in Fig. 8.

Dissemination Level: **Public**

This project has received funding from the European Union's Horizon 2020 research and innovation programme under the Marie Skłodowska-Curie Grant Agreement No. 764902.

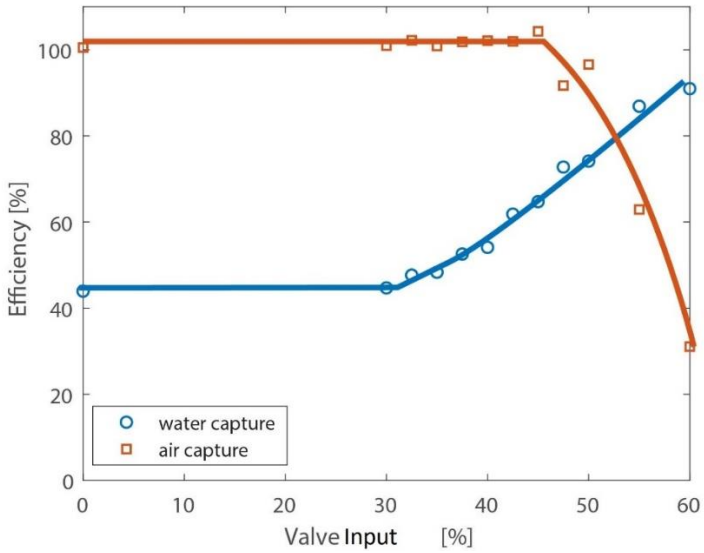

Fig. 8: Separation efficiency as a function of the valve input for $V_{sl} = 0.48$m/s and $V_{sg} = 0.13$m/s.

For the $V_{sl} = 0.48$m/s and $V_{sg} = 0.27$m/s condition, that has a higher flow rate of air and therefore a wider core, the separation is maximized for a lower valve input, 40 %, as presented in Fig. 9.

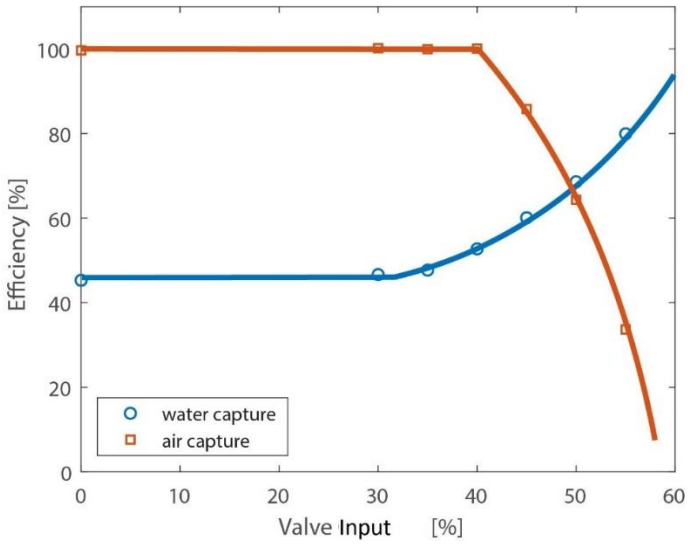

Fig. 9: Separation efficiency as a function of the valve opening for $V_{sl} = 0.48$m/s and $V_{sg} = 0.27$m/s

Choice of the reference core size

To check the change in the size of the gas core when alternating between the flow rates, the valve was kept at a 50 % input, and a step in the gas flow rate from the lower to the higher value was performed. The response is presented in Fig. 10.

Dissemination Level: **Public**

This project has received funding from the European Union's Horizon 2020 research and innovation programme under the Marie Skłodowska-Curie Grant Agreement No. 764902.

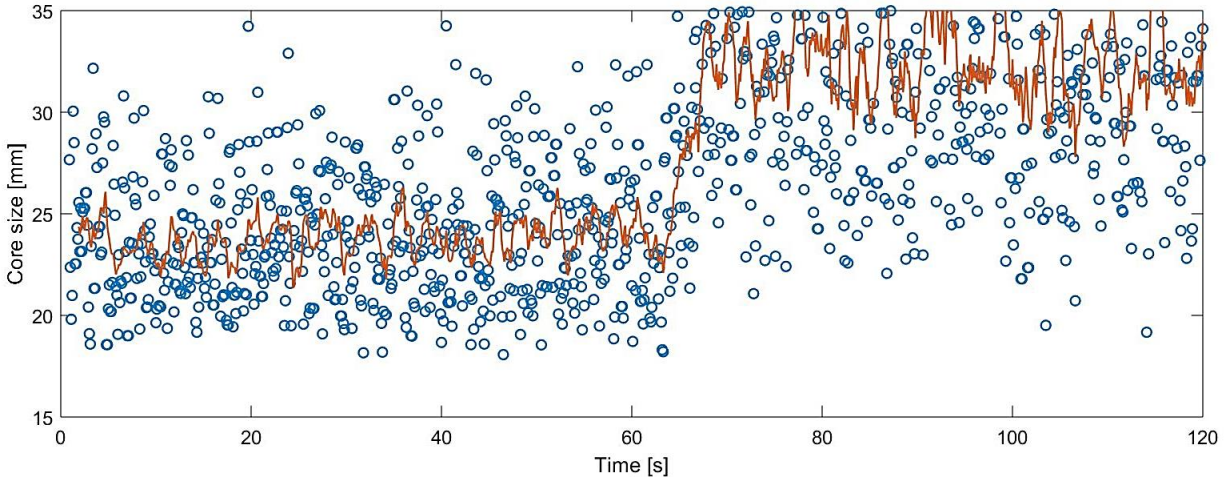

Fig. 10: Gas core size when changing the gas flow rate for a valve input of 50 %

In Fig. 10, the blue dots represent the raw ERT signal and the orange line represents a moving average of 10 samples. It can be clearly seen in the moving average that the gas core increases in size from around 25 mm to around 33 mm when increasing the gas flow rate. Moreover, it can be seen in the blue dots that the oscillations in the core are considerable. Those fluctuations are not noise of the sensor, but the natural oscillations of the core due to the upstream churn flow, causing a huge impact in the efficiency of separation. It is reasoned that such fluctuations are the main reason for the core size that maximizes efficiency to be relatively far from the pickup tube size, with an inner diameter of 36 mm.

When repeating the procedure with the valve at 40 % input, the core observed for the high flow rate condition is also at around 25 mm, which indicates that the efficiency of separation is maximized around that core size. Therefore, the value is used as reference for a bang-bang controller.

Bang-bang response

The bang-bang controller is implemented based on the size of the gas core. If the measured value by the ERT is bigger than 25 mm, then the valve is set to 40 %, in order to capture the increase in the amount of gas in the system. Otherwise, the valve is set to 50 %, which is optimal for the low flow rate condition.

When implemented, the controlled gas core size obtained for a step in the gas flow rate at 60 s is presented in Fig. 11. It is clear in the figure that the controller keeps the core size at around 25 mm even with the change in the flow rates.

Dissemination Level: **Public**

This project has received funding from the European Union's Horizon 2020 research and innovation programme under the Marie Skłodowska-Curie Grant Agreement No. 764902.

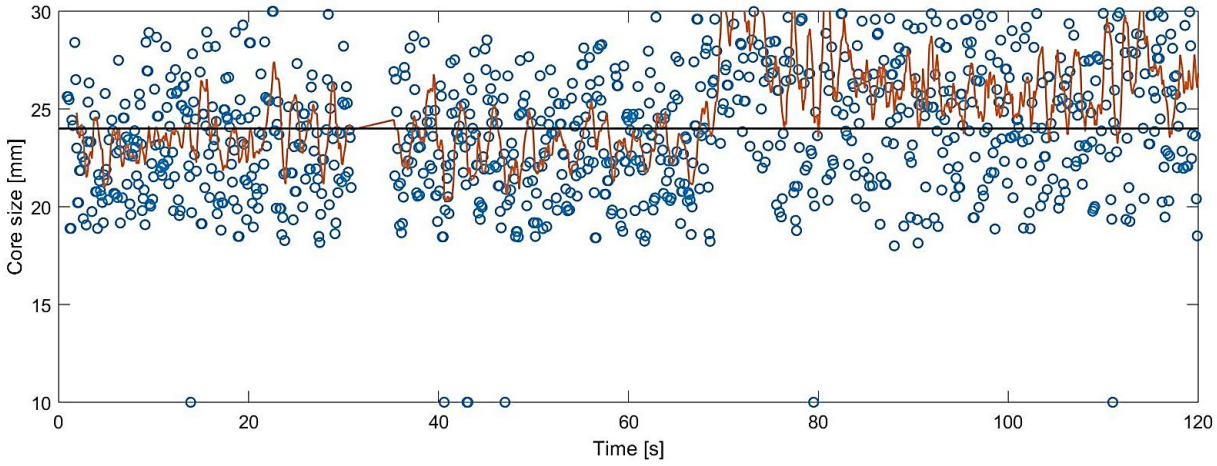

Fig. 11: Controlled gas core size

The efficiencies of separation for the uncontrolled and controlled scenarios, with core sizes presented in Fig. 10 and 11, are presented in Table 1. When applying the step change in the gas flow rate without adjusting the valve, the gas core increases in size pushing the water to the outer outlet. This results in a poor performance in the capture of air but a good efficiency in the capture of water, as a higher portion of the phase is pushed to the outer tube. When switching the controller on the efficiency of water decays in relation to the uncontrolled case, as now the core shrinks when adjusting the valve, which causes more water to reach the pickup tube. Due to the shrinking of the core, however, the capture of air increases substantially, such that there is an overall gain in efficiency (summing the two values) of 14 %, which is remarkable considering the simplicity of the controller implemented.

Table 1: Water and air efficiencies of the bang-bang controller

	Uncontrolled	Controlled
Water efficiency	73 %	61 %
Air efficiency	69 %	95 %

1.5.2. PI controller

A PI controller was also implemented on the loop, but now considering the 1 s low pass filter described in 2.2.3 instead of the moving average filter. In order to design such a controller, a Bode plot of the flow when acting on the pickup tube valve was experimentally achieved for the middle point between the bang-bang conditions and is presented in Fig. 12. A gap in the system response is observed that resembles a band-stop filter.

During the procedure of obtaining the efficiency curves and the Bode plot for the new conditions, a core size of 16.3 mm was observed to be optimal, which is smaller than the 25 mm of the bang-bang controller. Possible reasons are changes in the geometry of the outlets between the experiments or a better calibration of the ERT in the new dataset.

Dissemination Level: **Public**

This project has received funding from the European Union's Horizon 2020 research and innovation programme under the Marie Skłodowska-Curie Grant Agreement No. 764902.

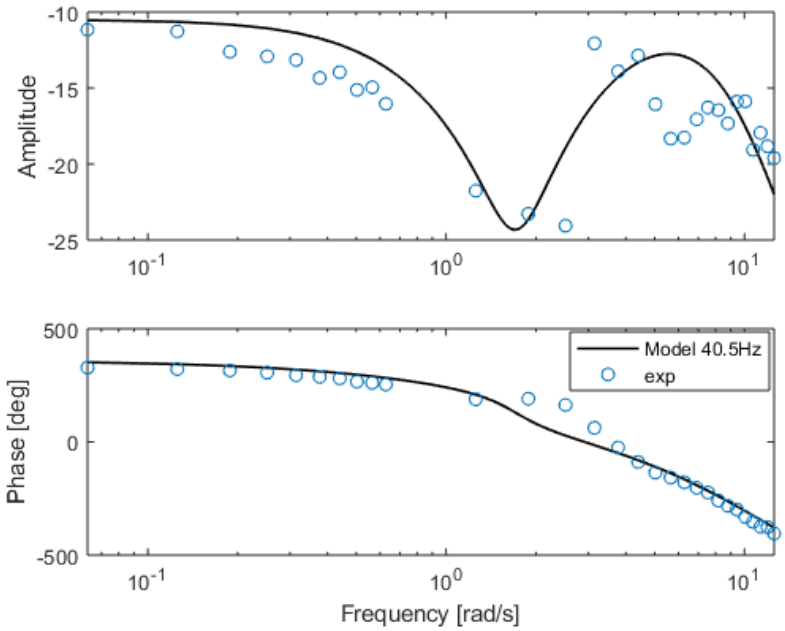

Fig. 12: Bode plot of the core size when acting on the pickup tube valve (open loop)

From the fit of the Bode plot, a discrete time PI controller ($T_s = 0.1s$) was designed and implemented targeting a response time of around 10 s while still keeping the system robust. After some experimental tuning of the constants and the verification of them based on the model, an optimal performance was achieved for $K_p = 1$ and $T_i = 2s$. The core size with and without the controller on, for the same a square wave between the bang-bang flow rates is presented in Fig. 13.

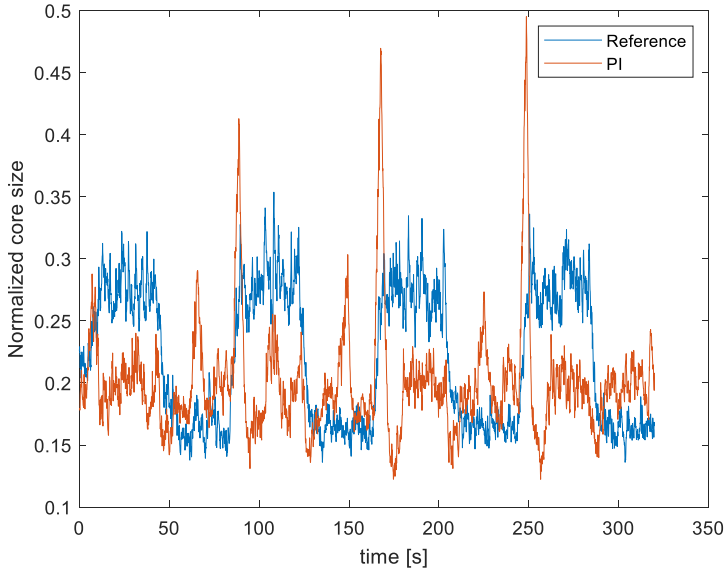

Fig. 13: Filtered core size without acting on the valve (blue) and using the PI controller (orange)

Dissemination Level: **Public**

This project has received funding from the European Union's Horizon 2020 research and innovation programme under the Marie Skłodowska-Curie Grant Agreement No. 764902.

It is observed in Fig. 13 that the ERT signal after the low pass filter follows a square wave in the blue signal, but it is kept around 0.2 in the orange signal. The exception is right after the change of the disturbance, where a peak shows up in the core size by the controller. This is due to the fact that the valve was almost fully closed to handle the low air flow rate configuration, and when the step occurs, the valve takes some time to act because of its hysteresis, not moving directly according to the input of the controller. Therefore, between the increase of the air flow rate and the valve movement, the core grows considerably and a lot of air is lost to the water outlet.

When analyzing the statistics of the two signals, the average core size went from 0.22 in the reference to 0.20 in the controlled core, and its standard deviation from 0.0549 to 0.0453. Therefore, not only the value was close to the reference, but the deviations were also minimized. In terms of efficiency, the reference has $\eta_{air} = 0.76$ and $\eta_{water} = 0.74$ and the controlled device has $\eta_{air} = 0.81$ and $\eta_{water} = 0.69$. The combination does not result in a clear increase in the system efficiency as in the bang-bang controller.

A possible explanation for the on-off controller to work better than the PI is that it does not force a core size, but just a change in the valve according to a certain threshold, i.e. for a low flow rate of air, the valve still goes to the maximum performance even if the core after the action stills smaller than the reference of the switch. The same reasoning is valid for a high flow rate of air, where the valve goes to the optimal condition in terms of performance as long as the core is bigger than the threshold, even if this means being far from it. This kind of action better accommodates the dependency of the core size in the flow rate of air via conservation of mass, as it avoids over-closing the valve to try to impose a core size that is far from the "natural" size from mass balance, which in many scenarios causes it to become unstable and fluctuate more (as the valve becomes almost fully closed).

1.6. Conclusions and perspective

The results of the final demonstration show that:

I. The developed wire-mesh sensor successfully sends the upstream void-fraction to the controller at 20 Hz.
II. This void fraction is deeply connected to fluctuations in the core size, and the delay between those is determined by the flow velocity.
III. The developed ERT system is able to well represent the core dynamics in both the time and frequency domains.
IV. The ERT signal has to be filtered to remove the high frequencies connected to the upstream churn flow when targeting external perturbations.
V. The application of tomography in control of inline swirl separators has a huge potential, as illustrated by the bang-bang controller with an overall gain of 14 % in the efficiency of separation.
VI. Due to the fluctuations in the core size, a single value (as a reference) seems to be insufficient to fully represent performance, and controlling the core size does not mean gaining efficiency, as shown in the PI controller results.
VII. A successful combination of tomography and control in the context of inline fluid separation was achieved in the Inline Fluid Separation group.

Dissemination Level: **Public**

This project has received funding from the European Union's Horizon 2020 research and innovation programme under the Marie Skłodowska-Curie Grant Agreement No. 764902.

1.7. References

[1] M. V. Bram, A. A. Hassan, D. S. Hansen, P. Durdevic, S. Pedersen, Z. Yang, Experimental Modeling of a Deoiling Hydrocyclone System. *IEEE Xplore*, 2015.

[2] M. A. Sattar, M. M. Garcia, R. Banasiak, L. M. Portela, L. Babout, Electrical Resistance Tomography for Control Applications: Quantitative Study of the Gas-Liquid Distribution inside A Cyclone. *MDPI Sensors*, 2020.

[3] M. A. Sattar, M. M. Garcia, L. M. Portela, L. Babout, Electrical Resistance Tomography Raw Data Processing Algorithm for Real Time Monitoring of Two-Phase Swirling Flows. Submitted to the special issue of *MDPI Sensors*.

[4] B. Sahovic, H. Atmani, M. A. Sattar, M. M. Garcia, E. Schleicher, D. Legendre, E. Climent, R. Zamansky, A. Pedrono, L. Babout, R. Banasiak, L. M. Portela, U. Hampel, Controlled Inline Fluid Separation Based on Smart Process Tomography Sensors. *Chemie Ingenieur Technik*, 2020.

[5] S.K. Star, Pressure distribution in a liquid-liquid cyclone separator, MSc Thesis, *Delft University of Technology*, 2016.

[6] B. Sahovic, H. Atmani, P. Wiedemann, E. Schleicher, D. Legendre, E. Climent, R. Zamanski, A. Pedrono, U. Hampel, A study on the relationship between upstream and downstream conditions in swirling two-phase flow, *Flow Measurement and Instrumentation*, 2020.

This project has received funding from the European Union's Horizon 2020 research and innovation programme under the Marie Skłodowska-Curie Grant Agreement No. 764902.

2. Tomography-Controlled Microwave Drying

2.1. Objectives

Microwave drying is an emerging technology in the industry for batch and continuous processing due to the possibility of volumetric and selective heating. Interaction of high-power microwaves for drying of materials with certain moisture content results in significant energy and time-saving as compared to conventional, convective, and radiative heating. In the drying application, the objective is to dry the foam uniformly with the final target to keep the moisture in a certain level inside the polymer foam at the end of the heating process. To achieve the objective, a novel idea is to apply tomography based intelligent control by integrating microwave tomography (MWT) and electrical capacitance tomography (ECT) with the control unit of the high power industrial microwave drying system to increase its efficiency and processing quality. The schematic of the tomography-controlled microwave drying is depicted in Fig. 14. The system is equipped with a conveyor belt to enable the continuous processing. The MWT is installed at the inlet of the heating system, while the ECT is installed at the outlet to estimate the moisture level in the polymer foam and is integrated with a control unit. The details of each module are provided in the next sections.

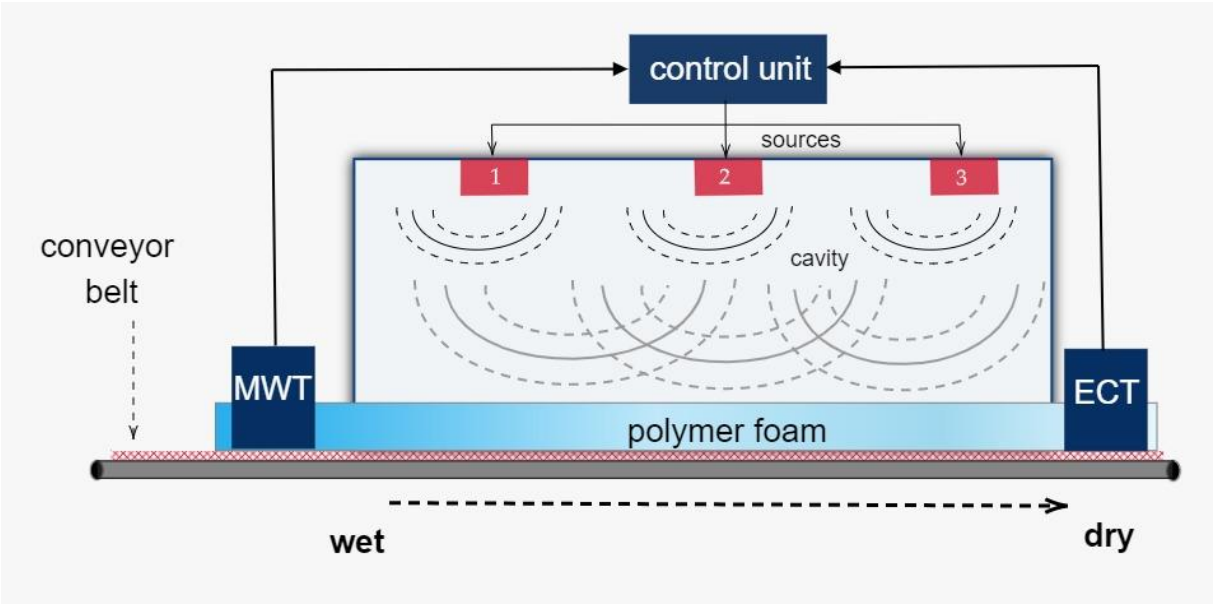

Fig. 14: A schematic of the tomography-controlled microwave drying

2.2. Experimental facility

The microwave drying system which we are currently working with is named HEPHAISTOS (shown in Fig. 15) located at Karlsruhe Institute of Technology, Germany and manufactured by Weiss Technik Gmbh, Reiskirchen, Germany. This industrial microwave applicator has a patented hexagonal cross-section design delivering high electromagnetic field homogeneity during the drying process. A conveyor belt is installed that enables a continuous drying process. Material processing, for instance, thermal curing of fiber composites and drying of pol-

Dissemination Level: **Public**

This project has received funding from the European Union's Horizon 2020 research and innovation programme under the Marie Skłodowska-Curie Grant Agreement No. 764902.

ymer foams, are some main target applications. The IR camera is limited to providing surface temperature and, fiber optic sensors are not applicable in a running belt process. The MWT and ECT systems are designed and integrated with the HEPHAISTOS to recover the volumetric information of the moisture location and its level during the drying process of the polymer foam. The power level and pulse duration of the magnetrons will be adjusted based on the information from MWT and ECT.

Fig. 15: A side view of the HEPHAISTOS microwave oven system. The main modules of the oven are represented by number tags 1, 2, 3, 4, 5. Tag 5 and Tag 1 represent the entrance of the wet foam and exit doors for the dry foam on the conveyor belt, respectively. Tags 2, 3, 4 indicate the three modular heating systems which inbuilt the hexagonal cavity with high power microwave heating sources and control system block. The MWT and ECT imaging modules are installed at the entrance (Tag 5) and exit (Tag 1) doors, respectively.

2.3. Microwave tomography sensor

An MWT module is installed at the inlet of the HEPHAISTOS industrial drying system, as shown in Fig. 16. The imaging modality is applied to estimate the moisture level in a polymer foam. The MWT setup consist of 11 WR90 open-ended waveguide antennas (VSWR $1.03{:}\,1$) connected (with the phase stable cables with a phase stability $3°$ at maximum frequency) to the Agilent N5224A VNA with a P9164C 2×16 solid state switch matrix. The data is acquired from 8 GHz to 12 GHz with 5 MHz frequency steps. Communication between the VNA, switch, and the controlling computer is accomplished through the local area network (LAN).

The data acquisition process is entirely automated using MATLAB. The data acquisition time for the MWT sensor is from 1 to 2 seconds. The moisture level in the foam from the MWT imaging algorithm is reconstructed in real-time and given as an input to the control system. The developed algorithms are i) multistatic uniform diffraction tomography (MUDT) [1,2], ii) time reversal (TR) [3], iii) Bayesian inversion (BI) [4,5], iv) MUDT-BI [6,7], and v) neural network (NN) [8,9].

Dissemination Level: **Public**

This project has received funding from the European Union's Horizon 2020 research and innovation programme under the Marie Skłodowska-Curie Grant Agreement No. 764902.

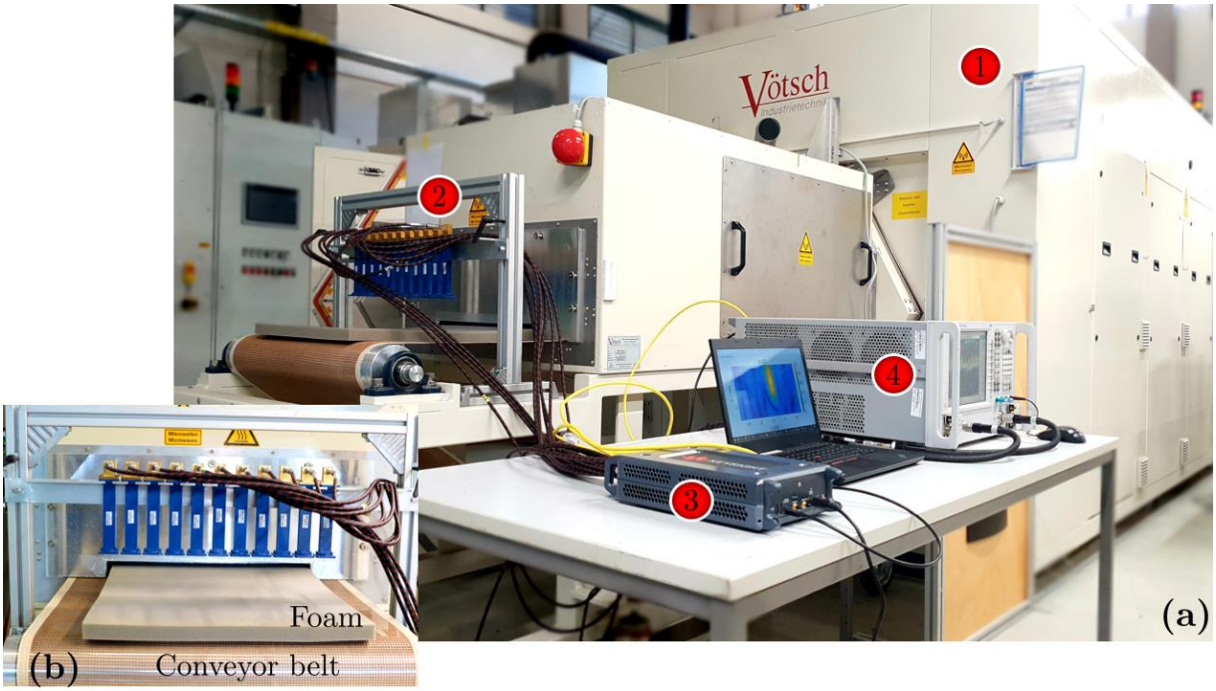

Fig. 16: (a) MWT system and its integration with the HEPHAISTOS (number Tag 1) is shown. The number Tags 2, 3, and 4 show the MWT system, Solid state switch, and VNA respectively. (b) shows the enlarged view of the MWT sensor array of X-band open-ended waveguide antennas.

2.4. Electrical capacitance sensor

Electrical capacitance tomography is an attractive tool for monitoring moisture distribution in several applications since it is non-invasive, fast and inexpensive. Fig. 17 shows an illustration of the designed ECT sensor for the microwave drying process. The sensor has six measuring electrodes on the top surface and six measuring electrodes on the bottom surface.

The measurement procedure involves applying an electrical voltage to excite one of the measuring electrodes while the rest are grounded. The electrical capacitance between the exciting electrode and the other grounded ones is measured, and then the same operation is repeated to the other measuring electrodes. It should be noted that there is a narrow electrically grounded electrode installed between every adjacent measurement electrode to improve the sensitivity of the measurements. However, they are not involved in the measurement procedure.

The ECT sensor was built and installed at the exit of the microwave oven and aimed to estimate the moisture distribution of polymer foams after the drying process, as shown in Fig. 18. The sensor was connected to a measurement device built by Rocsole Ltd. Kuopio, Finland. Each frame of measurement in ECT takes almost 720 ms. The measurements were transferred to a computer connected to the device. Based on the collected measurements, the permittivity distribution of the foam, which correlated with the material moisture, was reconstructed using the difference imaging method.

Dissemination Level: **Public**

This project has received funding from the European Union's Horizon 2020 research and innovation programme under the Marie Skłodowska-Curie Grant Agreement No. 764902.

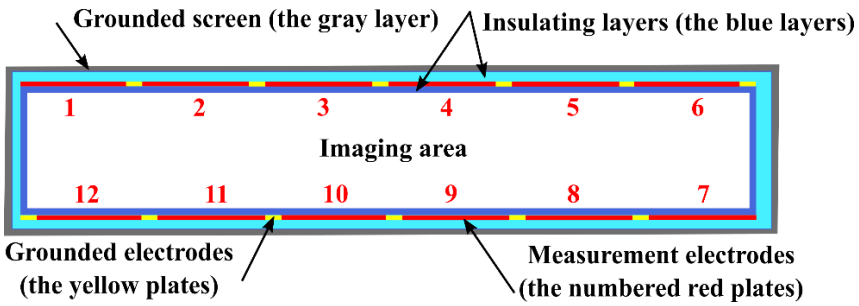

Fig. 17: An illustration of the ECT sensor: The target material (foam) is placed in the imaging area.

Fig. 18: The ECT sensor installed at the outlet of the HEPHAISTOS oven

2.5. Control Unit

2.5.1. Closed-loop control structure

In the microwave drying process, the wet foam with a high moisture value enters the oven, passes through the oven while being heated by 18 magnetrons with a maximum total power of 36 kW, and exits from the other side of the system with a lower moisture level. The controller aimed to adjust the power level of the magnetrons such that the output foam had a certain level of moisture.

The magnetrons were the actuators in the microwave drying process, and the control system acted upon them to reach the desired goal. On the other hand, the system output needed to

This project has received funding from the European Union's Horizon 2020 research and innovation programme under the Marie Skłodowska-Curie Grant Agreement No. 764902.

attain the desired setpoint was the permittivity distribution of the foam, estimated by the ECT sensor. The material permittivity is correlated with the material moisture distribution of the material, so we can control the moisture by controlling the permittivity. In addition to the power level of magnetrons, the input foam moisture also affected the system output. Although the ideal scenario was to keep the input foam moisture as constant as possible, the practical limitations did not allow constant input moisture. Therefore, the unwanted change in the input foam moisture was taken as the disturbance to the process and was measured by the MWT sensor. The disturbance measurement was helpful in the control strategies that had a disturbance rejection mechanism.

Fig. 19 shows the connections between the controller, oven and sensors. The controller code was implemented on MATLAB software installed on a computer connected to the microwave oven. The ECT sensor was connected via Ethernet cable to the same computer, and the reconstructions were done in real-time in MATLAB and sent to the controller. Moreover, the MWT data was accessible by the MATLAB program in real-time.

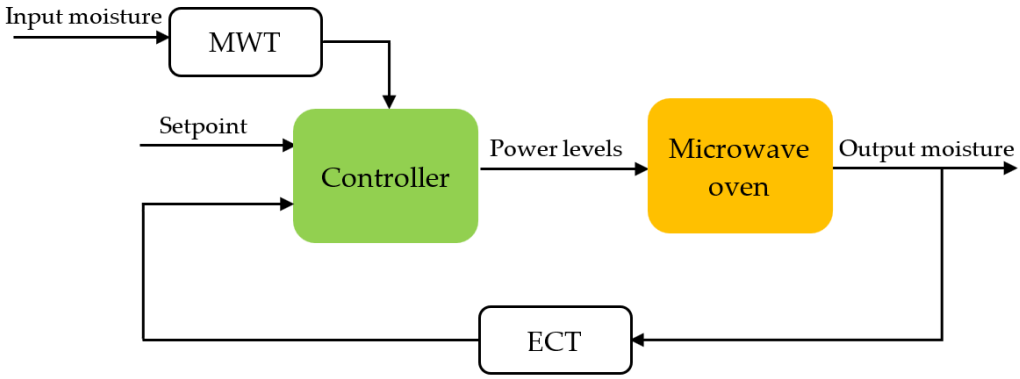

Fig. 19: A schematic of the controller structure and the tomographic sensors connections

2.5.2. Modelling and system identification

One of the requirements of developing an advanced control method was obtaining a dynamic model of the process. Since modeling the microwave process was a complex and time-consuming task, and the exact parameters of the heat and moisture transfer model were not available for the polymer foams, system identification methods were employed to obtain a model of the process. The problem was simplified by finding a single-input single-output (SISO) model of the process. It was assumed that the same power level ($P_l = P, l = 1, \cdots, 18$) was given to all magnetrons, and the average permittivity of the foam after the drying process was taken as the single output.

Different experiments were conducted by giving three standard inputs to the process, and the corresponding output from the ECT sensor was collected. The given inputs to the magnetrons were pseudorandom binary sequence (PRBS) signal, amplitude-modulated pseudorandom binary sequence (APRBS) signal, and a step signal with increasing and decreasing levels (staircase).

Dissemination Level: **Public**

This project has received funding from the European Union's Horizon 2020 research and innovation programme under the Marie Skłodowska-Curie Grant Agreement No. 764902.

The collected input-output data were used in the system identification algorithms to fit a state-space model of the order of eight for the microwave drying process. The derived model had two inputs: The power level percentage of the magnetrons as the control variable and the input foam moisture percentage on a wet basis as the disturbance to the process. The model output was the average permittivity change on a wet basis, $\Delta\epsilon_w$, which was calculated as:

$$\Delta\boldsymbol{\epsilon_d} = \frac{\overline{\Delta\boldsymbol{\epsilon}}}{\boldsymbol{\epsilon_{\mathrm{ref}}}} \times \mathbf{100}, \tag{5}$$

$$\Delta\boldsymbol{\epsilon_w} = \frac{\Delta\boldsymbol{\epsilon_d}}{\mathbf{100} + \Delta\boldsymbol{\epsilon_d}} \times \mathbf{100}, \tag{6}$$

where $\overline{\Delta\epsilon}$ is the average value of $\Delta\epsilon$ at the n nodes in the 2D discretization mesh, $\Delta\epsilon$ is the reconstructed permittivity change calculated using the ECT measurements, ϵ_{ref} is the best homogenous estimate of the dry foam permittivity, and $\Delta\epsilon_d$ is the dry basis permittivity change (in percentage).

The input channels in the estimated model had a considerable time delay since the ECT sensor was installed after the process, and the conveyor belt speed was relatively slow. The input delay for the control variable (power level percentage) was 261 seconds, while it was 1129 seconds for the input disturbance (input foam moisture). Fig. 20 shows an illustration of the process where several foam sheets were sent right after each other to the oven to conduct a continuous process for the purpose of process modeling and then later for evaluating the control methods. The first dataset with the PRBS input signal was used as the training dataset to find the model parameters, and the other datasets were used to validate the model. The results from the system identification of the microwave drying using the ECT sensor data are submitted to the TOMOCON special issue of MDPI sensors and are under review [11].

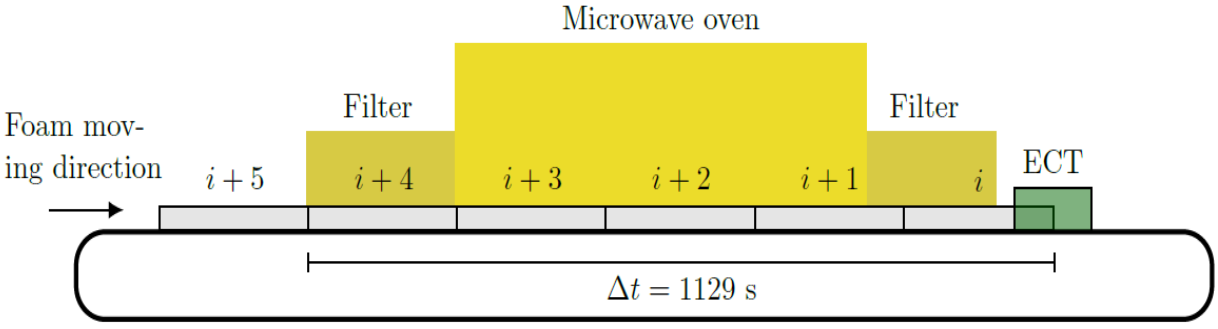

Fig. 20: The schematic of the continuous drying process of polymer foams. The gray rectangles indicate the polymer foams with the length of 150 cm and the thickness of 3 cm while passing first through the oven and then the ECT sensor with a speed of 40 cm/min. It takes 1129 s for every foam from the entrance point until it reaches the ECT sensor.

Dissemination Level: **Public**

This project has received funding from the European Union's Horizon 2020 research and innovation programme under the Marie Skłodowska-Curie Grant Agreement No. 764902.

2.5.3. Control methods

Five different control strategies were designed and investigated in both simulations and experiments for the microwave drying process. The input delay in the estimated model for this process made the controller design procedure very challenging. The first three designed controllers were PI controller, fuzzy PI controller, and LQG servo controller. In these controllers, only the permittivity estimation by the ECT sensor was used as feedback to the controller. The other two controllers were a combined feedback-feedforward controller and a generalized predictive controller (GPC). These two controllers had a disturbance rejection scheme, so the MWT sensor measurement from the input foam moisture was used to reject the input disturbance. The designed controllers are described in more detail as follows.

PI controller

The PI controller is a very common industrial controller that has been considered very efficient in most applications. The average permittivity value of the output foam was estimated based on the ECT measurements, and a tracking error was calculated by comparing this value to the desired setpoint. The PI controller calculated the power levels of the magnetrons based on the tracking error such that this error reaches zero. A schematic of the closed-loop control with PI controller is shown in Fig. 21.

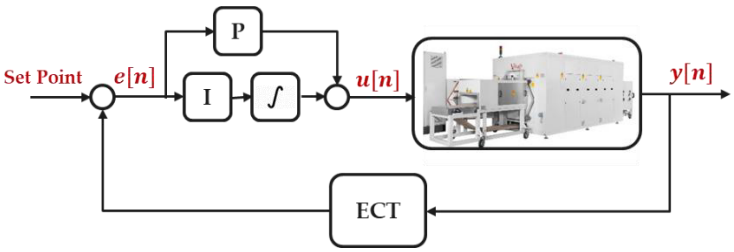

Fig. 21: A schematic of the PI controller for the microwave drying process

Linear quadratic Gaussian servo controller

The Linear–quadratic–Gaussian (LQG) controller is a model-based controller consisting of a Kalman filter to estimate the system state vector and a linear–quadratic regulator (LQR) controller that uses the estimated state vector to compute the control command. LQG servo controller uses an integral mechanism to track the desired setpoint. The connections between the integrator, Kalman filter, and the LQR controller (the K gain) are shown in Fig. 22. An LQR controller was previously designed and tested in simulations for the microwave drying process, and the results were published in [12].

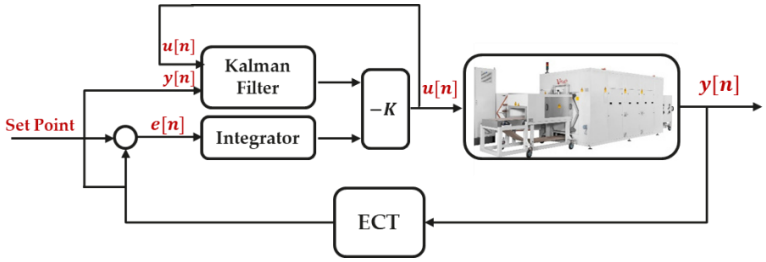

Fig. 22: A schematic of the LQG controller for the microwave drying process

Dissemination Level: **Public**

This project has received funding from the European Union's Horizon 2020 research and innovation programme under the Marie Skłodowska-Curie Grant Agreement No. 764902.

Fuzzy PI

The fuzzy PI controller is a type of PI controller in which the coefficients for the gain and integrator actions are not constant, and they are determined by a fuzzy interface that acts on the tracking error, as shown in Fig. 23. In principle, the amount of the tracking error at each time instant affects the PI coefficients. This way, the controller can have a higher performance.

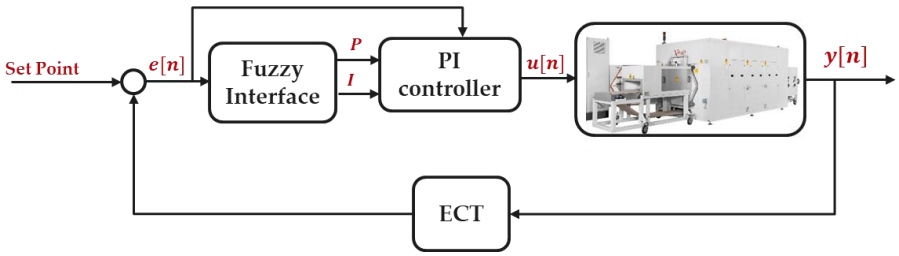

Fig. 23: A schematic of the Fuzzy PI controller for the microwave drying process

Combined feedback-feedforward controller

A combined feedback-feedforward controller has the advantage of a feedback loop designed to track a setpoint and a feedforward loop to reject the input disturbance. The designed PI controller was used as the feedback controller, and an additional feedforward controller was developed based on the known dynamics between the input disturbance and the output permittivity to eliminate the impact of the input disturbance. The input disturbance in this scenario was the input foam moisture that was measured by the MWT sensor. A schematic of the combined feedback-feedforward controller for the microwave drying process is illustrated in Fig. 24.

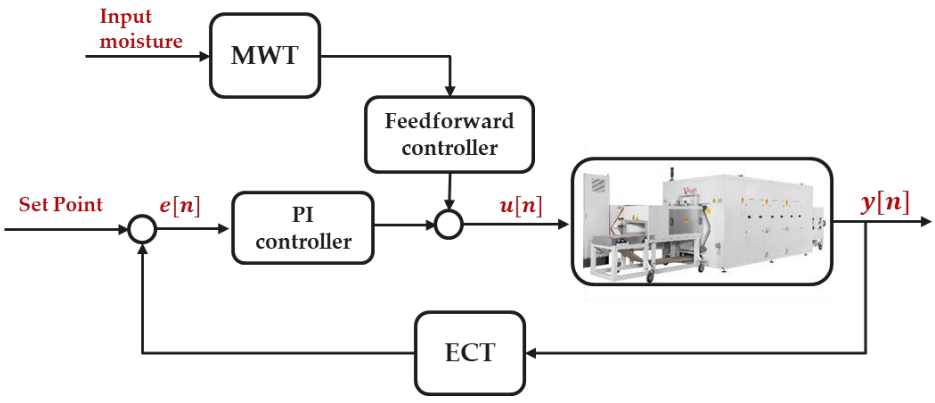

Fig. 24: A schematic of the combined feedback-feedforward controller for the microwave drying process

Generalized predictive controller

The generalized predictive controller (GPC) is a type of model predictive control (MPC) that has been widely implemented as an advanced controller in the process industries. GPC

Dissemination Level: **Public**

This project has received funding from the European Union's Horizon 2020 research and innovation programme under the Marie Skłodowska-Curie Grant Agreement No. 764902.

gives the possibility of tuning the control parameters and prediction horizons, adding the control signal rate to the cost function, and explicitly considering constraints.

2.6. Augmented Reality

In the final demonstration, we propose a novel augmented reality (AR) system in supporting onsite analysis with interactivity and mobility for the demo. In addition, it can provide information richness of volumetric visualization regarding the industrial process tomography (IPT) processes to support the mutual collaboration of users. The critical information of the industrial process is visualized in our mobile AR App which is built on iOS/Android devices as an early-stage setup [13,14]. The proposed system has three main components, as displayed in Fig. 25:

- Industrial process: MWT-controlled industrial microwave drying process: A unique heating and drying process operated in a confined chamber with sophisticated industrial settings. In our study, the target is a microwave drying process for polymer foams undergone by the precise HEPHAISTOS microwave oven system shown in Fig. 26.
- Users: Operators who control and run the drying equipment or researchers who take onsite observations and collect data for further analysis.
- AR App: The core part of our proposed system. As a preliminary stage, the application is manifested as a mobile App run on iOS/Android mobile devices and used for interactive and collaborative volumetric visualization and analysis. In comparison with our previous work [6], a multiple floating interface provided and overlaid in a real environment and containing information from our proposed data workflow is the main component of the application.

2.6.1. The AR application

The principal part of the initiated AR system is a mobile App developed to visualize the necessary information revealed from the data processing and visualizing pipeline, while it supports interactive and collaborative onsite data analysis. This App serves as an intermediary tool between the users and the precise experimental equipment used for displacing the visualized information regarding the ongoing process. The users, for example, operators, can interact with the visualizations projected on the AR interface, with the mobility of merely holding a mobile device alongside the bulky equipment. As Fig. 25 illustrates, people from different communities, such as practical operators or academic researchers, have the capacity to interactively and instantly observe the information related to the process by simply activating the App without initiating other facilities. The App was developed via Unity and Vuforia engines, aiming at the present stage for iOS/Android portable devices such as smartphones and tablets. By pointing the camera of the devices towards the precise equipment (the HEPHAISTOS system) used for performing drying and heating, the App will then be activated, displaying a floating interface with the necessary information (figures, images, etc.) virtually superimposed. Compared to our previous work, the application itself has been ameliorated to not only a single interface but on-site multiple interfaces containing various visualizations obtained from the data pipeline. Users are able to switch to the visualizations they require for the desired analyses. As shown in Fig. 26, some different floating interfaces incorporating different modalities of visualizations are presented and supported by switching after activating the App. The mobility of the AR interface provides users with ongoing visualizations as they move around the equipment that runs the designated process.

Dissemination Level: **Public**

This project has received funding from the European Union's Horizon 2020 research and innovation programme under the Marie Skłodowska-Curie Grant Agreement No. 764902.

.

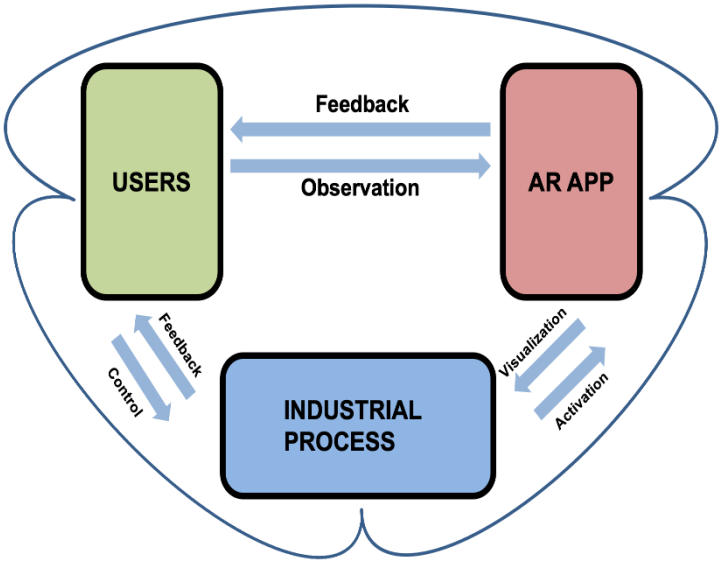

Fig. 25: The proposed AR system framework. Industrial process block: This covers the whole running procedure of the industrial drying process, providing data and elements used for analysis. Users block: This represents the people involved in this context. The operators who control and run the process and the researchers who observe and analyze the process are the main composition of this part. **AR App** block: This entails the AR implementation, which was a mobile AR App developed on iOS/Android platform at the initial stage. The App allows different communities of people to get access to the volumetric data visualized interactively and to conduct the onsite analysis collaboratively.

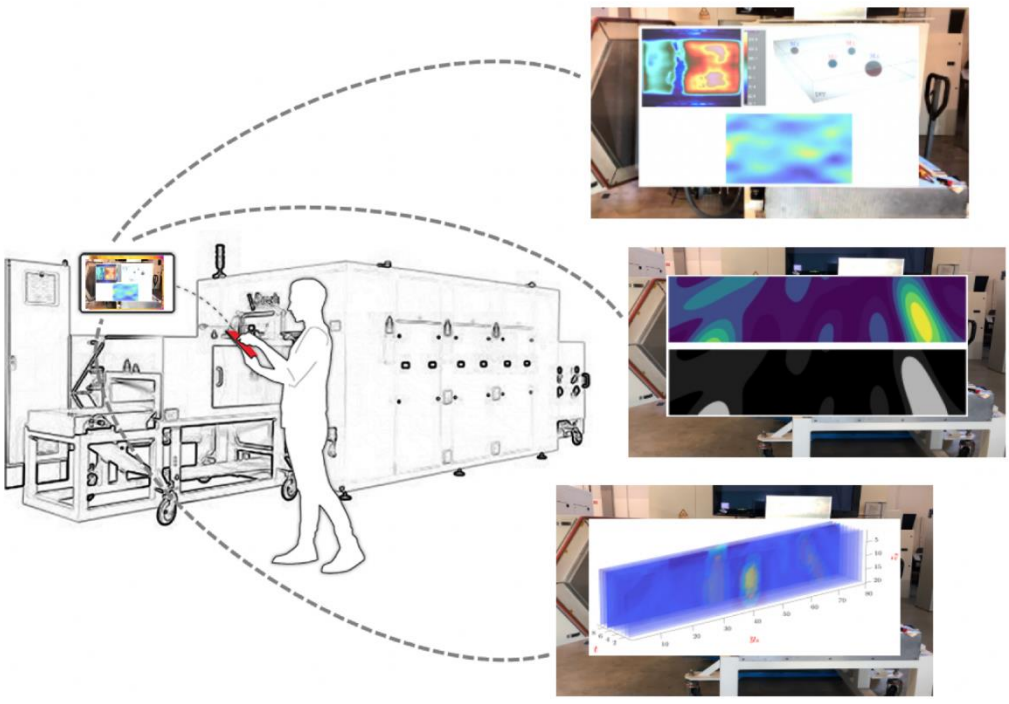

Fig. 26: The realization of the proposed AR system. Users hold the handheld smartphones/tablets to run the AR App alongside the industrial setting. After the App activation, users can then observe the visualizations displayed on the AR interfaces. At present, the App is supported on iOS/Android mobile devices. Users are empowered to switch to different visualizations regarding different phases of the process. The visualizations shown on the interfaces are multimodal, including the infrared image showing the condition of the process and the 3D/2D reconstruction of the MWT images (the upper left small figure on the floating interface in the upper right subfigure); the reconstructed MWT images with their segmented results to show the high moisture areas (the middle right subfigure); the volumetric visualization (the bottom right subfigure).

2.7. Results of the lab demo

The laboratory demonstration was conducted by integrating both tomography sensors (MWT and ECT) measurements into the controller. The controller was implemented in MATLAB and had access through an interface to the oven and could adjust the power levels of the magnetrons. In the following sections, the experimental results from each sensor are given individually, and the derived model is validated with the collected experimental datasets. Eventually, the experimental results from the closed-loop control system integrated with the sensors are demonstrated.

2.7.1. MWT sensor

An example of the estimated moisture distribution using the NN method during the drying process is presented in Fig. 27. The moisture percentage is based on the wet basis, and estimated moisture levels are shown for different time-shots. Note that only average of the estimated moisture level is used for the current control strategies.

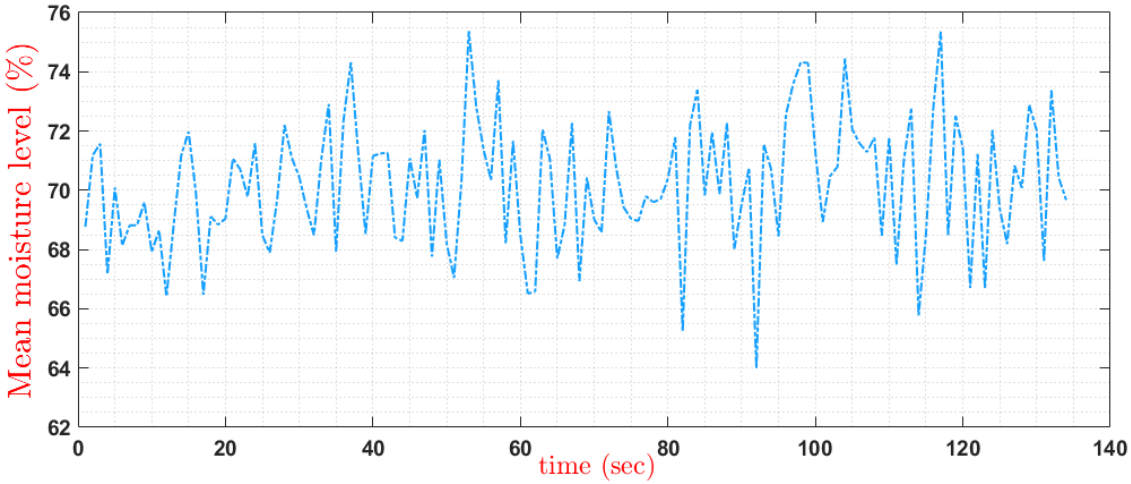

Fig. 27: Estimated mean moisture level at the inlet

2.7.2. ECT sensor

The ECT sensor performance was evaluated through different experiments with stationary and moving foams. The results from one of the experiments with the ECT sensor while a foam sheet was moving on the conveyor belt through the sensor are presented in this section. The microwave power sources were off in this experiment, and the belt speed was 40 cm/min. Fig. 28 shows the sample foam tested in this experiment. It contained 14 different pieces, which were cut, moisturized to specific amounts, and returned to their original locations in nine rows. 2D reconstructions were calculated at each time instant while the foam was moving through the electrode plane of the ECT sensor. The reconstructions were stacked together to form a 3D visualization illustrated in Fig. 29. The reconstruction results with the ECT sensor are published in [10].

Dissemination Level: **Public**

This project has received funding from the European Union's Horizon 2020 research and innovation programme under the Marie Skłodowska-Curie Grant Agreement No. 764902.

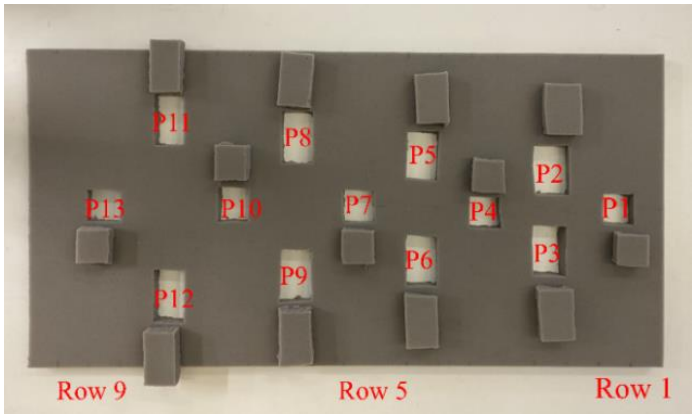

Fig. 28: The sample foam tested for the measurements with 13 separate moisture locations

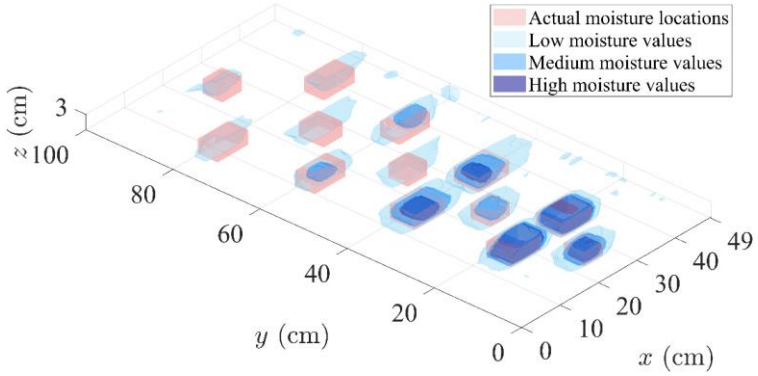

Fig. 29: 3D visualization of the experiment results with a conveyor belt speed of 40 cm/min while the microwave sources were off

2.7.3. Process model

In this section, the derived model output is compared with the experimental data to evaluate the model accuracy. Fig. 30 shows the collected input and output data with the PRBS input signal. This dataset was used to estimate the model parameters. As can be seen, the calculated model output follows the actual experimental data from the ECT sensor with good accuracy. The fit value calculated using the normalized mean squared error (NMSE) cost function for this dataset was 96.17 %, which is very accurate.

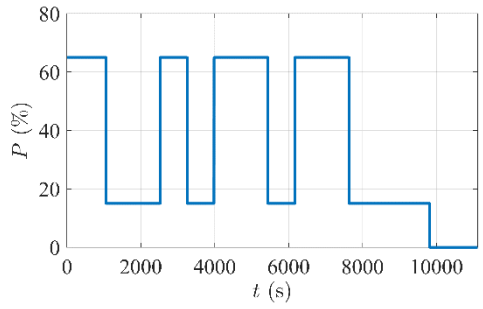

(a)

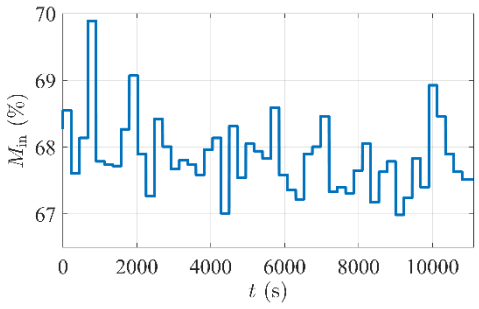

(b)

Dissemination Level: **Public**

This project has received funding from the European Union's Horizon 2020 research and innovation programme under the Marie Skłodowska-Curie Grant Agreement No. 764902.

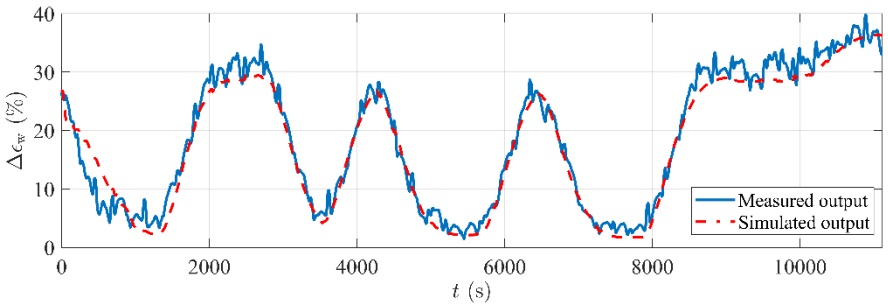

(c)

Fig. 30: The input-output dataset with the PRBS input signal used for estimating the process model: (a) The applied input power percentage to the microwave sources. (b) The input foam moisture variations. (c) Comparison between the actual measurements and the model output.

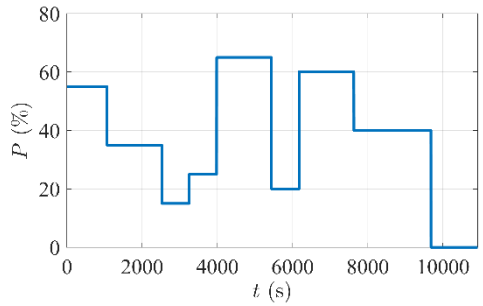

(a)

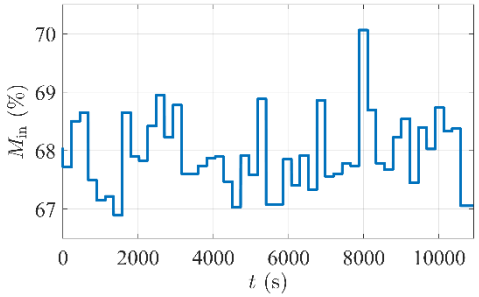

(b)

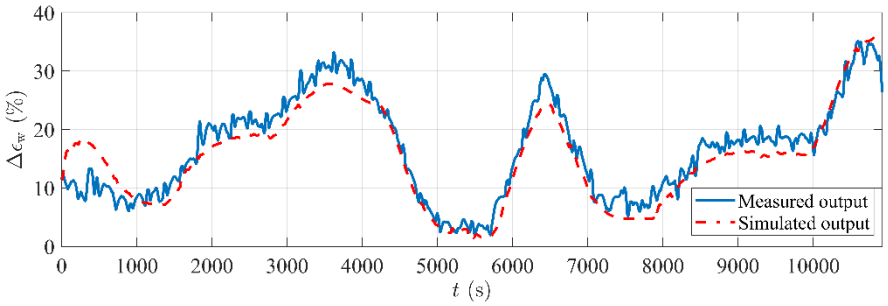

(c)

Fig. 31: The input-output dataset with the APRBS input signal used for validation of the process model: (a) The applied input power percentage to the microwave sources. (b) The input foam moisture variations. (c) Comparison between the actual measurements and the model output.

Since the PRBS input dataset was used in the model estimation, another dataset with the APRBS input signal was used to validate the model. The inputs and output data with this dataset are shown in Fig. 31. As can be seen, although the input signal has different behavior compared to the previous dataset, the model output can still follow the experimental process output. The fit value for this dataset was calculated as 87.8 %, which is a great fit for a validation dataset.

Dissemination Level: **Public**

This project has received funding from the European Union's Horizon 2020 research and innovation programme under the Marie Skłodowska-Curie Grant Agreement No. 764902.

2.7.4. Controller

Five different controllers were designed and implemented, as explained in Section 2.5.3. The main aim of the controller was to adjust the power level percentage of the magnetrons such that the polymer foam after the drying process had a certain level of moisture. Since the ECT sensor reconstructed the permittivity value of the foam and not the moisture, to avoid calibration errors, the permittivity change on a wet basis ($\Delta\epsilon_w$) was taken as the system output to be controlled.

As the first controller, the PI controller was implemented to control the output foam permittivity. The reconstruction result from the system output, measured by the ECT sensor while the PI controller was implemented, is shown in Fig. 32 (a). The setpoint for the first 2 hours of the experiment was 20 %, while we changed it to 10 % for the rest of the experiment. As can be seen, the process output, $\Delta\epsilon_w$, has followed the setpoint in both cases with reasonable accuracy. The PI controller output in this experiment which was the command power level for the magnetrons is illustrated in Fig. 32 (b).

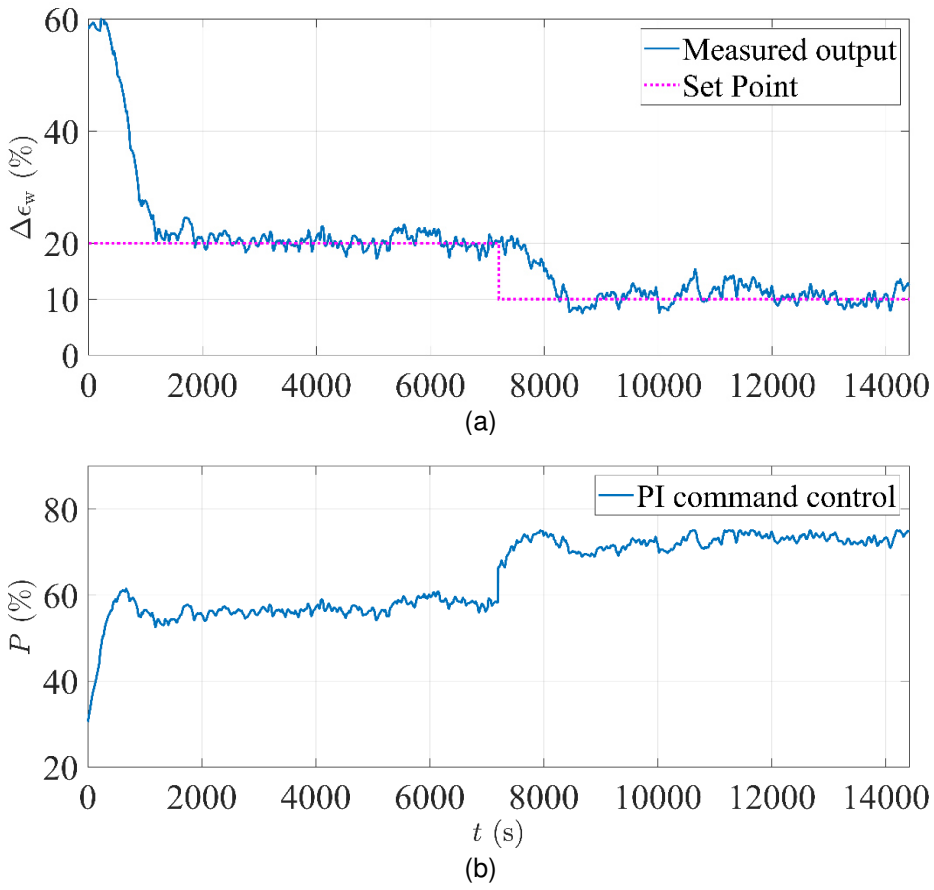

Fig. 32: The experimental results with the designed PI controller: (a) The average permittivity change on a wet basis reconstructed from the ECT measurements. (b) The PI controller output that is the power level percentage of the magnetrons.

Dissemination Level: **Public**

This project has received funding from the European Union's Horizon 2020 research and innovation programme under the Marie Skłodowska-Curie Grant Agreement No. 764902.

The polymer foams were put on a digital scale before and after the drying process to measure the actual moisture on a wet basis. Note that only the average value for each foam sheet could be calculated. The recorded moisture percentages of the polymer foams in the experiment with the PI controller are illustrated in Fig. 33.

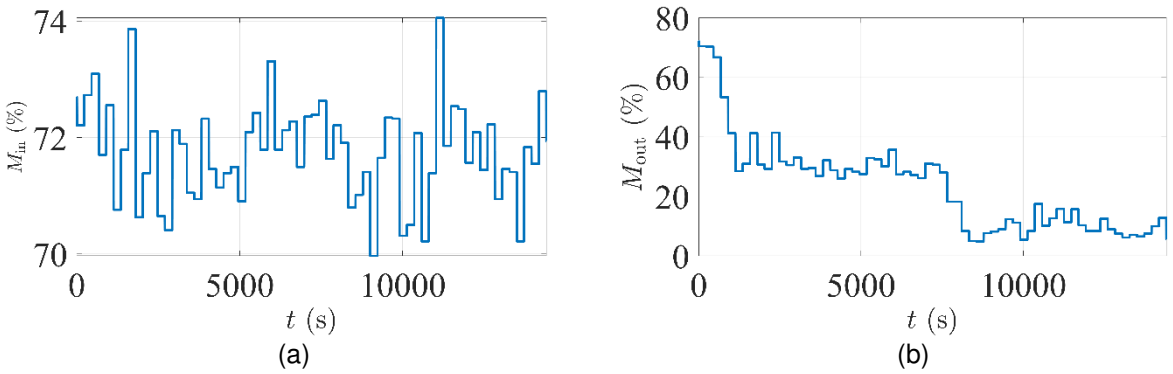

Fig. 33: The foam moisture on a wet basis while the PI controller was implemented. (a) The input foam moisture (before the drying) (b) The output foam moisture (after the drying).

In the second experiment, the LQG controller was implemented. The process output with the LQG controller is presented in Fig. 34 (a). The desired setpoint changed from 20 % to 10 % and then from 10 % to 25 % in this experiment to evaluate the controller performance in tracking multiple setpoints. As shown, the system output was able to follow the setpoint, although it had some fluctuations.

It should be noted that the LQG controller is a model-based and linear controller. That means that the modeling error can highly affect the system performance. The results show that although a linear model was fit to a highly nonlinear process, the controller could still follow the setpoint. The corresponding power level percentage with the designed LQG controller is shown in Fig. 34 (b). As can be seen, the command control calculated by the LQG controller has a smooth curve and stays within the control constraints. The recorded moisture percentages for the polymer foams before and after the process in this experiment are illustrated in Fig. 35. The experimental results with the PI and LQG controller will be submitted to Control Engineering Practice [15].

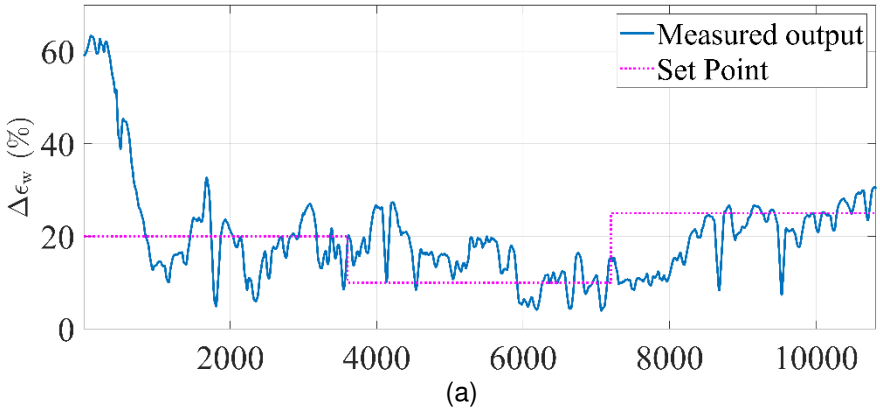

Dissemination Level: **Public**

This project has received funding from the European Union's Horizon 2020 research and innovation programme under the Marie Skłodowska-Curie Grant Agreement No. 764902.

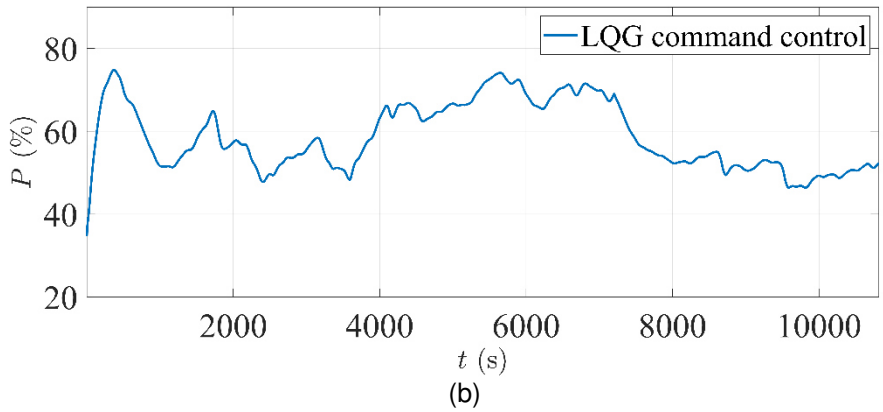

(b)

Fig. 34: The experimental results with the designed LQG controller: (a) The average permittivity change on a wet basis reconstructed from the ECT measurements. (b) The LQG controller output that is the power level percentage of the magnetrons.

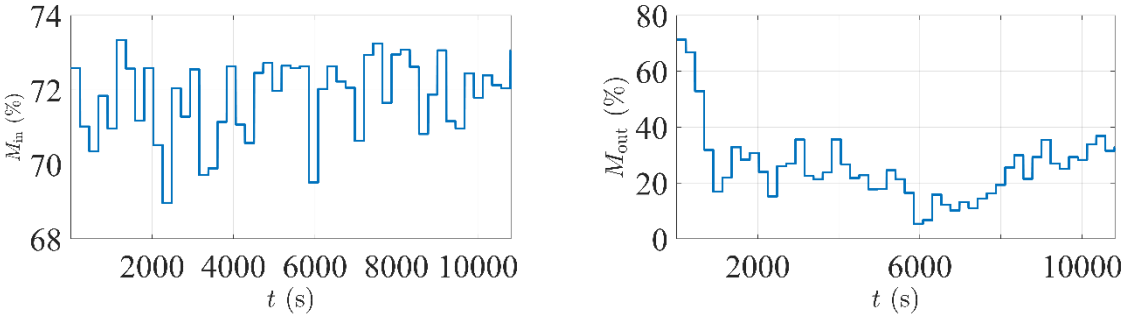

(a) (b)

Fig. 35: The foam moisture on a wet basis while the LQG controller was implemented. (a) The input foam moisture (before the drying) (b) The output foam moisture (after the drying).

The standard PI controller had very good results; therefore, the idea of a fuzzy PI controller was investigated as the next step to enhance its performance even more. Fig. 36 shows the experimental results with the fuzzy PI controller. As can be seen, the system output is trying to follow the setpoint, although the fluctuations are relatively high. The experimental results suggest that the intended performance for the fuzzy PI was not achieved, and the standard PI had a better performance.

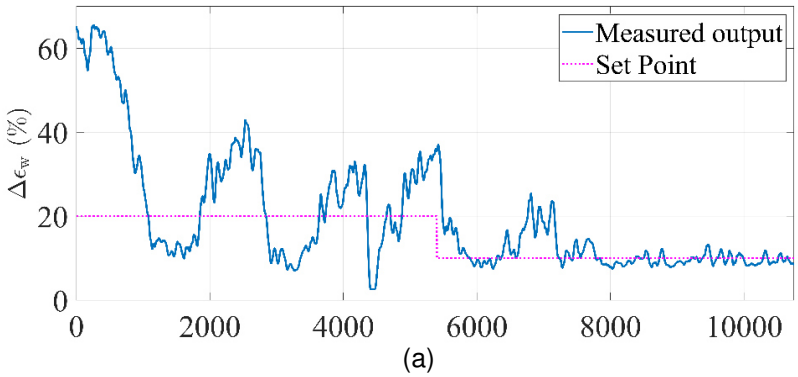

(a)

Dissemination Level: **Public**

This project has received funding from the European Union's Horizon 2020 research and innovation programme under the Marie Skłodowska-Curie Grant Agreement No. 764902.

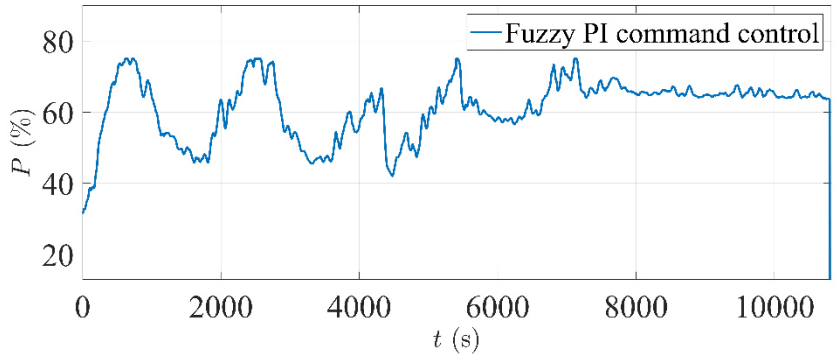

(b)

Fig. 36: The experimental results with the designed fuzzy PI controller: (a) The average permittivity change on a wet basis reconstructed from the ECT measurements. (b) The fuzzy PI controller output that is the power level percentage of the magnetrons

This report does not present the experimental results from the other two controllers (Combined feedback-feedforward controller and the GPC) as the experiments with those controllers were not successful.

2.7.5. Comparing response of the controlled and uncontrolled microwave drying process

In this section, the simulation results of two scenarios are presented to evaluate the response of the microwave system when it has a PI controller compared to an uncontrolled case. As mentioned in Section 2.7.4, the controller adjusts the power levels of the magnetrons according to the setpoint. The alternative could be finding the appropriate power level without a controller by conducting several experiments to find the right power level based on trial and error. Therefore, the first advantage of having a controller is automatically adjusting the power levels and saving time and energy by avoiding the trial and error process.
Another advantage of having a controller in the loop is automatically reacting to any changes in the process conditions. Without a controller in the loop and monitoring the process output, the power levels cannot be adjusted according to changes. An example was examined by simulating the conducted experiment with the PI controller and using the same input foam moisture as Fig. 33 (a). Fig. 37 shows the simulated process output with the PI controller while the setpoint had changed from 20 % to 10 % in the middle of the experiment.

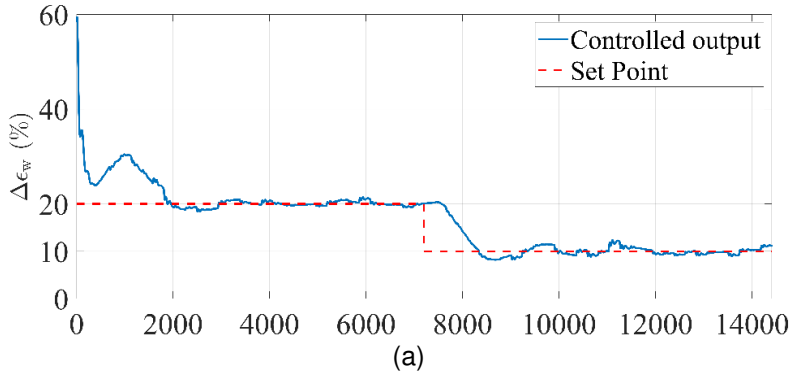

(a)

Dissemination Level: **Public**

This project has received funding from the European Union's Horizon 2020 research and innovation programme under the Marie Skłodowska-Curie Grant Agreement No. 764902.

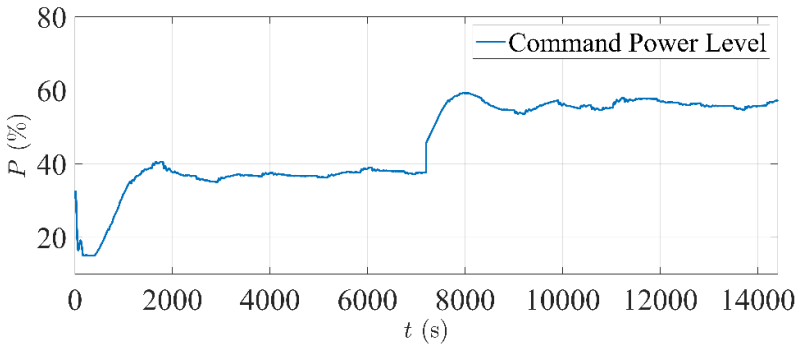

(b)

Fig. 37: The simulation results with the designed PI controller: (a) The average permittivity change on a wet basis calculated from the process model. (b) The power level percentage of the magnetrons calculated by the PI controller.

The controller was removed in the next step, knowing the appropriate power level to reach the desired setpoints. Based on Fig. 37 (b), a constant power level of 37 % and 56 % was chosen to achieve a 20 % and 10 % set point, respectively. To compare the performance of the process with and without the controller, we changed the process condition by decreasing the input foam moisture by only 5 %. Fig. 38 shows the simulation results of the comparison. As can be seen, the system with the PI controller recognized the change in the input moisture and decreased the power levels accordingly.

On the other hand, the system without the controller had resulted in an over-dry foam. The mean squared error (MSE) jumped from 5.7 to 15.2 by removing the controller, and 12 kWh more energy was used during the whole experiment in the uncontrolled case than the controlled system (around 21 % more). The simulation results show the importance and benefits of having a moisture controller designed for the microwave drying process.

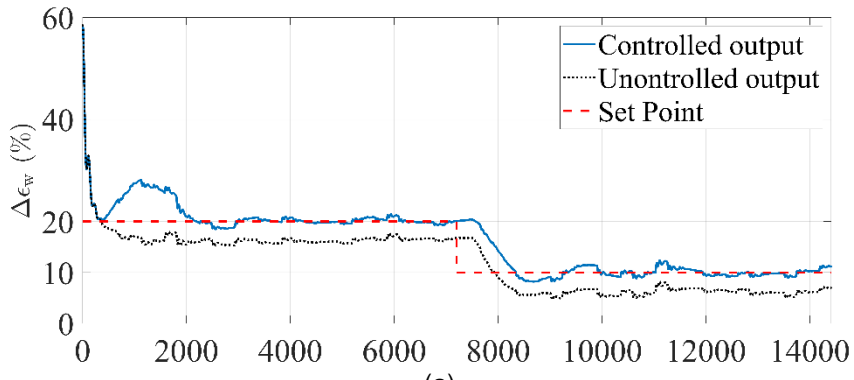

(a)

Dissemination Level: **Public**

This project has received funding from the European Union's Horizon 2020 research and innovation programme under the Marie Skłodowska-Curie Grant Agreement No. 764902.

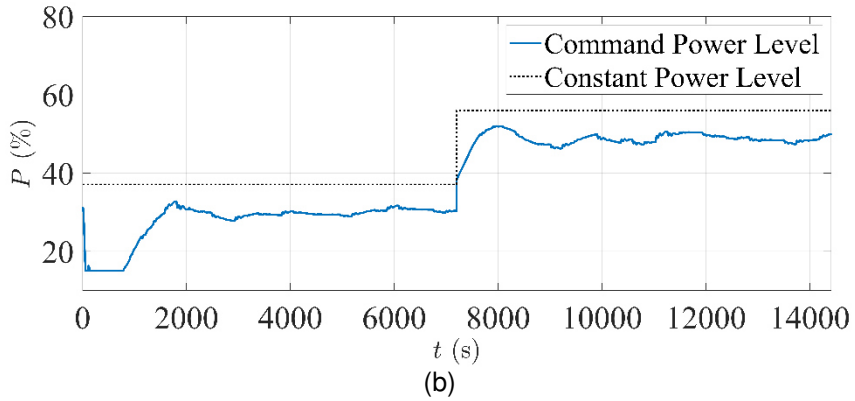

(b)

Fig. 38: The simulation results of an uncontrolled process compared to the controlled process with the designed PI controller: (a) The average permittivity change on a wet basis calculated from the process model in both controlled and uncontrolled process cases. (b) The power level percentage of the magnetrons calculated by the PI controller compared with a constant power level.

2.8. Conclusions and outlook

The application of two tomography sensors (MWT and ECT) was investigated for the microwave drying process. Both sensors were designed, built, and installed on the microwave system. The MWT sensor was installed at the entrance of the microwave oven, estimating the input foam moisture, while the ECT sensor was located at the exit of the oven and estimated the output foam moisture. A process model was derived for the microwave drying process, and the integration of tomography sensors with a designed moisture controller was studied.

MWT sensor and Augmented Reality

We have designed and developed the MWT imaging system consisting of open-ended waveguide antennas working in X-band frequency. The imaging modality is applied to estimate the initial moisture information in the polymer foam. For the estimation of the moisture, reconstruction algorithms based on diffraction tomography, statistical inversion theory, and neural-network were formulated and successfully tested for different moisture conditions. All the developed algorithms can give volumetric information of the moisture distribution. However, considering the preliminary controller strategy employed in this work, only neural-network was used to estimate the average initial moisture content in the foam. The integration of the MWT and its output information support to the control unit is indecisive in the present controller strategies and shall be the subject of future studies.

From the AR point of view, the priority will be bringing more informative visualizations [16] into the data pipeline, for instance, getting more categories and more formats of volumetric visualizations that would give users a better comprehension of the process output. Furthermore, involving constructive usability and usage testing is another critical concern, for example, designing a systematic user study by engaging adequate people to perform specific tasks in our AR system, collecting feedback, and revising the system correspondingly. In addition, prototyping on advanced AR equipment such as Microsoft HoloLens 2 or Magic Leap headsets will be another concentration, which should break the limit in screen displaying and yield higher interactivity and immersivity for targeted users.

Dissemination Level: **Public**

This project has received funding from the European Union's Horizon 2020 research and innovation programme under the Marie Skłodowska-Curie Grant Agreement No. 764902.

ECT

The ECT sensor was designed and built using 12 measuring electrodes and employed the difference imaging method as the reconstruction algorithm. The ECT sensor was able to estimate the moisture locations and the moisture levels with good accuracy. The average relative estimation error for the ECT sensor based on several experiments was 7.6 %, sufficient for control purposes.

Modeling and control

A state-space model was derived for the microwave drying process, and the model accuracy was validated with different collected datasets. The estimated model was SISO, and the average permittivity value of the output foam was taken as the process output. Five different controllers were designed and experimented on the microwave drying process. The standard PI controller and the LQG controller had better experimental results compared to the other controllers. With the designed PI and LQG controller, the process was able to follow different desired setpoints as the average permittivity value in a 2D cross-section.

In future studies, a multi-input multi-output (MIMO) model of the process can be derived. The aim of having a MIMO model is to use the reconstructed permittivity distribution instead of an average value and adjust the power levels of the magnetrons individually to reach homogenous moisture in the polymer foam after the drying process. Furthermore, more experiments with the designed controller can be conducted to find the best design parameters for these controllers and enhance the performance. Other control strategies suited for the microwave drying process, like the neural network controllers, can also be investigated.

Dissemination Level: **Public**

This project has received funding from the European Union's Horizon 2020 research and innovation programme under the Marie Skłodowska-Curie Grant Agreement No. 764902.

2.9. References

[1] A. Omrani, G. Link, J. Jelonnek, A Multistatic Uniform Diffraction Tomographic Algorithm for Real-Time Moisture Detection. *2020 IEEE Asia-Pacific Microwave Conference (APMC)*, Hong Kong, pp. 437-439 (2020).

[2] A. Omrani, R. Yadav, G. Link, J. Jelonnek, A Multistatic Uniform Diffraction Tomography Algorithm for Microwave Imaging in Multilayered Media for Microwave Drying. *Unpublished*.

[3] A. Omrani, R. Yadav, G. Link, J. Jelonnek, A Time Reversal Imaging Algorithm for Localization and Moisture Level Detection in the Polymer Foam in an Industrial Microwave Drying System. *Ampere 2021*.

[4] R. Yadav, A. Omrani, M. Vauhkonen, G. Link, T. Lähivaara, Microwave tomography for moisture level estimation using Bayesian framework. *15th European Conference on Antennas and Propagation, EuCAP 2021.*

[5] R. Yadav, A. Omrani, G. Link, M. Vauhkonen, T. Lähivaara, Correlated Sample-based Prior in Bayesian Inversion Framework for Microwave Tomograph. *IEEE Transaction on Antennas & Propagation*, *Unpublished*.

[6] A. Omrani, R. Yadav, G. Link, T. Lahivaara, M. Vauhkonen, J. Jelonnek, A Bayesian inversion framework coupled with Diffraction tomography in microwave imaging of moisture in a polymer foam for the industrial drying system. *IEEE Transaction on Antennas & Propagation*, *Unpublished*.

[7] A. Omrani, R. Yadav, G. Link, M. Vauhkonen, T. Lähivaara, J. Jelonnek, A combined microwave imaging algorithm for localization and moisture level estimation in multilayered media. *15th European Conference on Antennas and Propagation, EuCAP 2021.*

[8] R. Yadav, M. Vauhkonen, G. Link, S. Betz, T. Lähivaara, Microwave tomography for estimating moisture content distribution in porous foam using neural networks. *2020 14th European Conference on Antennas and Propagation (EuCAP)*, pp. 1-5 (2020), doi: 10.23919/EuCAP48036.2020.9135296.

[9] T. Lähivaara, R. Yadav, G. Link, M. Vauhkonen, Estimation of Moisture Content Distribution in Porous Foam Using Microwave Tomography With Neural Networks. *IEEE Transactions on Computational Imaging*, Vol. 6, pp. 1351-1361 (2020).

[10] M. Hosseini, A. Kaasinen, G. Link, T. Lähivaara, M. Vauhkonen, Electrical Capacitance Tomography to Measure Moisture Distribution of Polymer Foam in a Microwave Drying Process. *IEEE Sensors Journal,* doi: 10.1109/JSEN.2021.3085762.

[11] M. Hosseini, A. Kaasinen, G. Link, T. Lähivaara, M. Vauhkonen, System identification of microwave drying process of polymer foams using electrical capacitance tomography. *Sensors*, *Under review.*

[12] M. Hosseini, A. Kaasinen, G. Link, T. Lähivaara, M. Vauhkonen, LQR Control of Moisture Distribution in Microwave Drying Process Based on a Finite Element Model of Parabolic PDEs. *IFAC-PapersOnLine,* 53 (2), pp. 11470-11476 (2020).

This project has received funding from the European Union's Horizon 2020 research and innovation programme under the Marie Skłodowska-Curie Grant Agreement No. 764902.

[13] Y. Zhang, R. Yadav, A. Omrani, M. Fjeld, A Novel Augmented Reality System To Support Volumetric Visualization In Industrial Process Tomography. *Proceedings of the 2021 Conference on Interfaces and Human Computer Interaction,* pp. 3–9 (2021).

[14] Y. Zhang, Y. Ma, A. Omrani, R. Yadav, M. Fjeld, M. Fratarcangeli, Automated Microwave Tomography (MWT) Image Segmentation: State-of-the-Art Implementation and Evaluation. *Journal of WSCG*, Vol. 28, pp. 126-136 (2020).

[15] M. Hosseini, A. Kaasinen, G. Link, T. Lähivaara, M. Vauhkonen, Modeling and tomography-assisted control of a microwave drying process with the application of LQG and PI control. *Control Engineering Practice, To be submitted*.

[16] Y. Zhang, A. Omrani, R. Yadav, M. Fjeld, Supporting Visualization Analysis in Industrial Process Tomography by Using Augmented Reality—A Case Study of an Industrial Microwave Drying System. *Sensors,* 21, p. 6515 (2021).

[17] R. Yadav, A. Omrani, M. Vauhkonen, G. Link, T. Lähivaara, Microwave Tomography using Neural Networks for its Application in an Industrial Microwave Drying System. *Sensors 2021*, *Under review.*

[18] A. Omrani, R. Yadav, G. Link, T. Lähivaara, M. Vauhkonen, J. Jelonnek, An Electromagnetic Time-Reversal Imaging Algorithm for Moisture Detection in Polymer Foam in an Industrial Microwave Drying System. *Sensors* 2021, *Under review.*

This project has received funding from the European Union's Horizon 2020 research and innovation programme under the Marie Skłodowska-Curie Grant Agreement No. 764902.

3. Tomography-Controlled Continuous Casting

3.1. Objectives

In continuous casting the amplitude of the magnetic field generated by electromagnetic actuators is defined by the production receipt and is currently not dependent on the present flow condition in the mould. Due to the lack of appropriate flow measurement techniques, examples of control strategies of the electromagnetic brakes (EMBrs) based on flow measurements were not investigated yet and have to be designed from scratch. Therefore, the first objective was to identify flow instabilities of the flow in the demonstrator, for which an appropriate control can be developed. In an industrial caster, typical disturbances of the flow are the injection of argon gas and clogging of the Submerged Entry Nozzle (SEN). In the process of clogging, small non-metallic inclusions, which are floating in the liquid steel, stick to the wall of the SEN and build up a plug. The reduction of the cross section or the ports of the SEN may lead to an asymmetric flow in the mould. Sometimes, these plugs detach from the SEN and flow into the mould, leading to a sudden increase of the flow rate. In order to reduce clogging, Argon gas is injected into the SEN via the stopper rod or a porous region in the upper part of the SEN.

Velocity measurements by the means of Ultrasound Doppler Velocimetry (UDV) of the flow in the mould of the demonstrator revealed that the flow is quite stable. However, it turned out that the effects of a small plug, which accidentally was built up during the experiments by depositing oxides in the SEN close to the stopper rod, was clearly detectable in the UDV flow field measurements and a control loop was developed in the course of the project. The focus was on the control of the impingement position of the jet at the narrow faces and the maximum velocity at the free surface. Recently, we experimentally studied the effects of argon gas injection via the stopper rod on the flow in the mould of the demonstrator. Contrary to previous measurements with a smaller mould, we only observed a reduction of the liquid metal flow rate with the present operating parameters but no instabilities of the flow, which could be influenced by the EMBr. Therefore, we decided not to include two-phase flows and to model only clogging of one port of the SEN by inserting an obstacle close to the port (see section of control strategies).

The development of CIFT in presence of the electromagnetic brake required more time as expected, because the effect of changing the amplitude of the EMBr on the CIFT measurement system has to be compensated in an appropriate way. The challenge is the hysteresis of the ferromagnetic material of the pole shoes. Therefore, the compensation does not only depend on the electrical current through the coils of the brake but also on the history of the changes. This compensation was first developed as a post-processing step and then later extended to a real-time compensation procedure. Therefore, we started in the beginning of the project to develop different control strategies based on UDV measurements in the demonstrator. When the CIFT measurement system became available for the present setup with the EMBr, two challenges appeared: (i) The spatial resolution of the CIFT reconstruction is less precise than the UDV measurements so that a new approach for designing the flow feature extraction for the flow feature extraction is required, and (ii) during the change of the strength of the electromagnetic brake no flow measurements is possible. These limitations prevent the direct use of the developed control loops based on UDV measurements and would require a major change of the models. Thus, we decided to develop a controller which

Dissemination Level: **Public**

This project has received funding from the European Union's Horizon 2020 research and innovation programme under the Marie Skłodowska-Curie Grant Agreement No. 764902.

detects left/right asymmetries of the jet impingement position and switches the brake on or off.

The main objective was a proof of concept that inductive methods allow the real-time control of the flow in the mould using an EMBr. This includes the demonstration of the ability of CIFT to detect major flow features in the mould in real time, even while the strength of the EMBr is changed. In the experiments we could show that clogging in combination of an operating brake leads to an undesired asymmetric flow in the mould which can be avoided by switching off the brake. Due to the fact that two-phase flows do not strongly affected the flow, the MIT sensor was not included into the control loop development yet.

In order to describe the results of this final experiments in more detail, we first give a short overview of the demonstrator and will describe the latest developments of both measurement techniques, Contactless Inductive Flow Tomography (CIFT) and Mutual Inductance Tomography (MIT). Then, a detailed description of the experiment parameters and the action of the control loop is given.

3.2. Laboratory setup

Experiments were performed at the Mini-LIMMCAST facility at Helmholtz-Zentrum Dresden-Rossendorf. Additionally, design and optimization experiments for MIT sensor design and operation were performed in the tomography laboratory at the University of Bath.

Mini-Limmcast is a 1:5 scaled isothermal model of a continuous caster to investigate flow phenomena. It is operated with the eutectic alloy Galium-Inidium-Tin (GaInSn) which is liquid at room temperature. High electrical conductivity of GaInSn enables the use of electromagnetic actuators to alter the flow to achieve the desired flow structure in the mould.

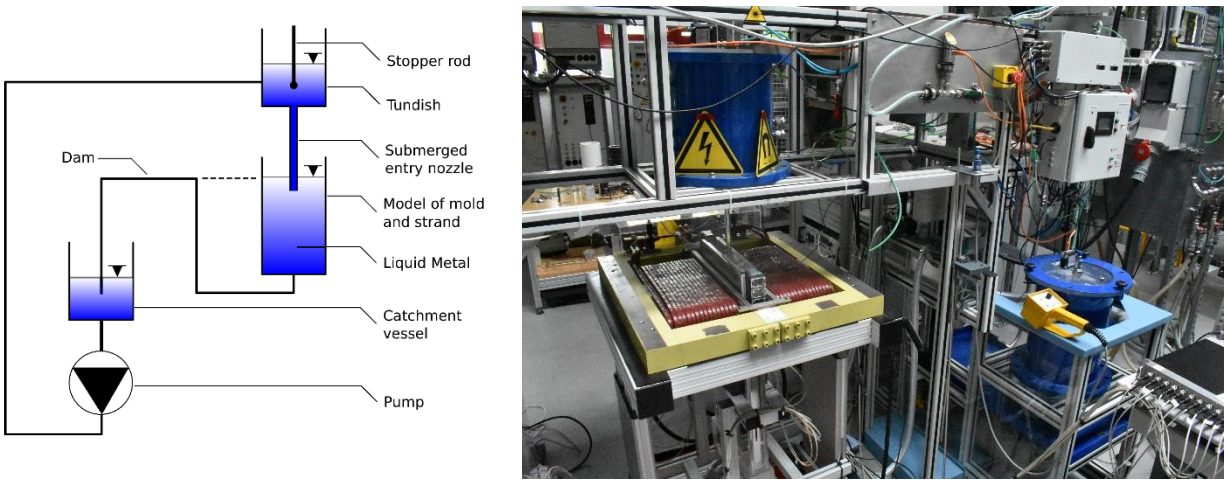

(a) (b)

Fig. 39: (a) Sketch of the liquid metal loop. (b) Photography of the demonstrator setup

The liquid metal is pumped from the storage tank to the tundish, where the inflow is regulated in order to keep a constant level of the liquid metal in the tundish. From the tundish, the liquid metal flows through the SEN. The flow rate is regulated by the opening position of the stop-

Dissemination Level: **Public**

This project has received funding from the European Union's Horizon 2020 research and innovation programme under the Marie Skłodowska-Curie Grant Agreement No. 764902.

per rod at the SEN inlet. Liquid metal flows from the SEN in the mould which has a 300×35 mm^2 profile. About 600 mm below the free surface of the liquid, the mould has an outlet port at the bottom to which an overflow is connected by two hoses. The overflow is connected to the storage tank. The position of the overflow is adjustable and at atmospheric pressure in order to keep the liquid metal at a constant level in the mould. Fig. 39 represents the sketch of the liquid metal loop and a photography of the demonstrator setup.

An electromagnetic brake (EMBr) is used as an actuator to alter the flow structure in the mould. Additionally, Argon gas can be injected via the tip of the stopper rod to better simulate the conditions during the continuous casting process.

3.3. Contactless inductive flow tomography

Experiments with Contactless Inductive Flow Tomography were conducted in several stages. The final design of the CIFT setup consists of two excitation coils, one below and one above the ferromagnetic yoke of the EMBr. The flow induced magnetic field is measured by 14 sensors, seven on each narrow side of the mould. Combination of stainless steel and hard plastic casing is used to achieve sufficient mechanical robustness of the measurement setup. Fig. 40 depicts the CIFT setup arrangement in relation to the mould and the close up photograph of the assembled CIFT setup.

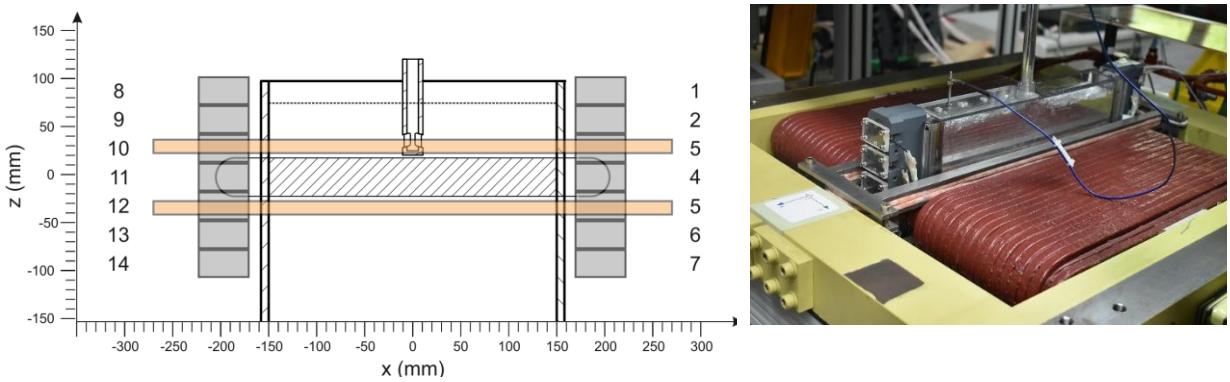

(a) (b)

Fig. 40: (a) Sketch of the liquid metal loop. (b) Photography of the demonstrator setup.

Following the design and manufacturing a custom sensor setup, first validation measurements of the magnetic field were conducted to assess the fit of the magnetic field to the numerical simulations. Fig. 41 shows the measured and simulated magnetic field along the center axis. The simulation is in good agreement with the measurement.

This project has received funding from the European Union's Horizon 2020 research and innovation programme under the Marie Skłodowska-Curie Grant Agreement No. 764902.

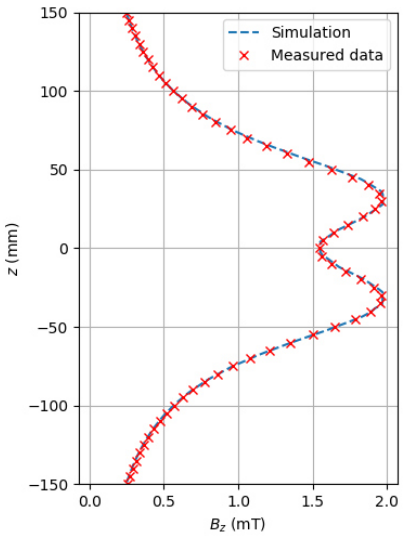

Fig. 41: Simulated and measured vertical component of the magnetic field along the z-axis

The CIFT measurement setup was then fitted to the demonstrator to perform the flow measurements with and without operating the EMBr. The EMBr in both cases was present but was not always in use. Fig. 42 depicts the measured flow induced magnetic field in dependence of the time. At the beginning of the measurement t=0s the values are normalized to 0, and any deviation is a result of the fluid velocity perturbing the excitation magnetic field. At t = 60 s the flow starts and we detect a change of the measured flow induced magnetic field. In this case, the flow induced magnetic field has a value up to 80 nT.

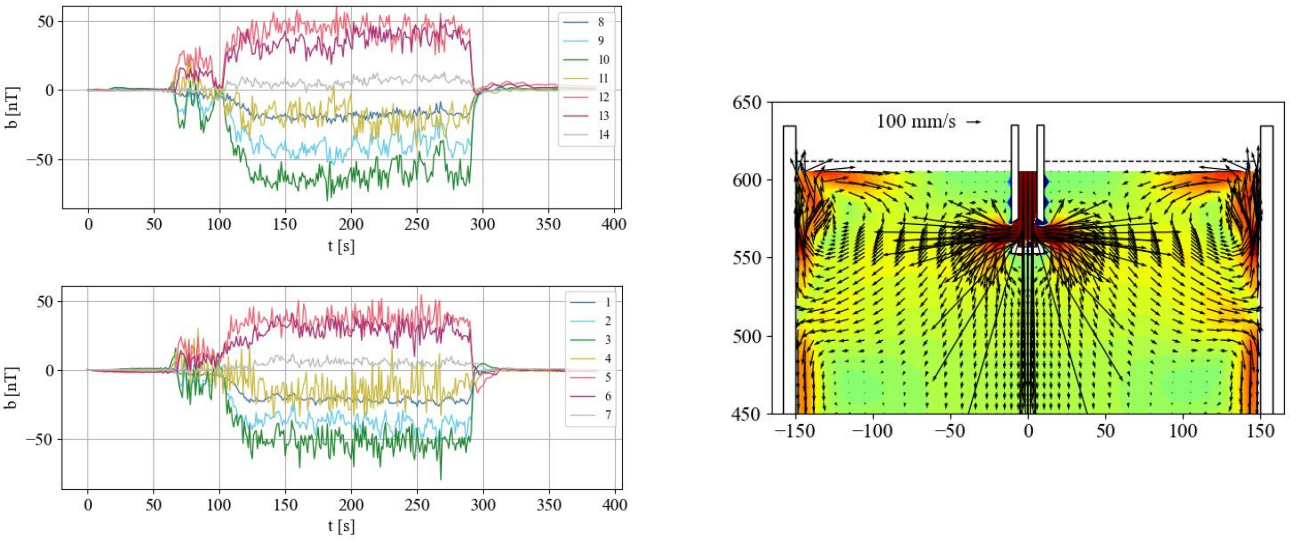

(a) (b)

Fig. 42: (a) Flow induced magnetic field. (b) Reconstruction of the velocities in the middle plane of the mould for average flow induced magnetic field for t_1 = 175 s to t_2 = 225 s

Before CIFT can be used to monitor the flow in dependence of the strength of the EMBr, the effects of changing the strong static magnetic field of the EMBr on the CIFT measurements have to be investigated. A set of experiments were conducted in order to identify the influ-

Dissemination Level: **Public**

This project has received funding from the European Union's Horizon 2020 research and innovation programme under the Marie Skłodowska-Curie Grant Agreement No. 764902.

ence of the strong magnetic field generated by the EMBr. An initial set of experiments has shown that the excitation magnetic field is slightly altered by the change of the magnetization vector in the ferromagnetic parts as a result of different amplitudes of the magnetic fields generated by the EMBr. The extent of the influence is shown in Fig. 43. Fig. 43 (a) presents the current through the brake in dependence of the time, while Fig. 43 (b) depicts the measured magnetic field changes at the CIFT sensors. For the highest current for the EMBr, the value of the magnetic field is more than 4000 nT, while the flow induced magnetic field is expected to be about 80 nT, as seen in Fig. 42. The reason of this strong change of the magnetic field measured by the sensor are the ferromagnetic parts. Due to their magnetic hysteresis, the depicted changes do not linearly depend on the current through the coils of the brake. To compensate for these effects, a numerical model of the hysteresis was implemented based on the Krasnosel'skii-Pokrowskii model of hysteresis, where the input is the current thorough the EMBr, and the output of the model is the compensation value for the EMBr that needs to be subtracted from the measurement values. Fig. 43 (c) shows a measurement without compensation and Fig. 43 (d) shows the same data set with compensation. The compensated data set is used for the reconstruction. Fig. 44 depicts two flow reconstructions for two different values of the current through the EMBr. It is obvious that the typical flow structure is reconstructed and the change of the jet impingement point at the right narrow wall (x = 150mm) is visualised.

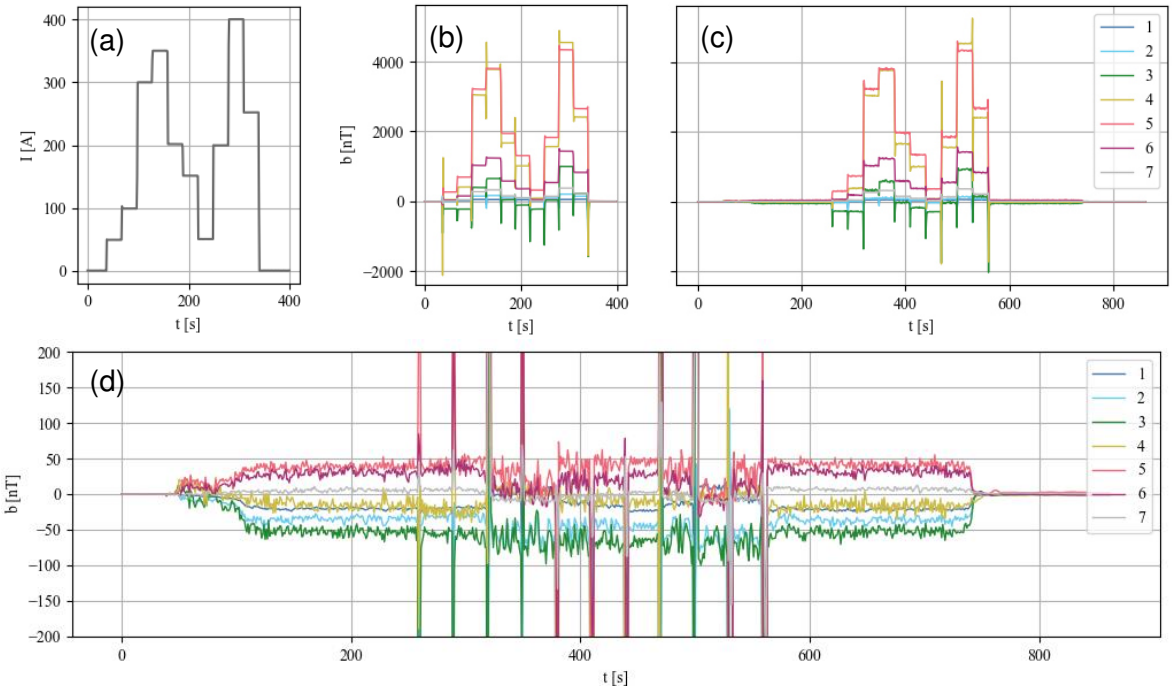

Fig. 43: (a) Set of values of the current of the EMBr. (b) Corresponding measured values at the first seven sensors without flow. (c) Measured values for a case with flow and arbitrary changes of the EMBr current. (d) Compensation of the flow induced magnetic field.

This project has received funding from the European Union's Horizon 2020 research and innovation programme under the Marie Skłodowska-Curie Grant Agreement No. 764902.

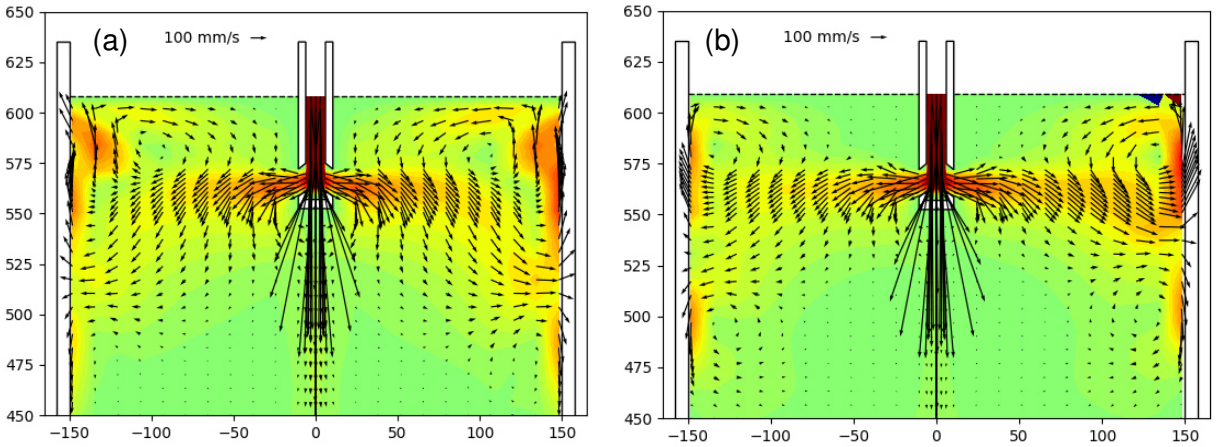

Fig. 44: Reconstruction of the flow field of the compensated flow induced magnetic field from Fig. 43 (d); (a) $t = 149$ s, $I_{EMBr} = 0$ A. (b) $t = 337$ s, $I_{EMBr} = 350$ A.

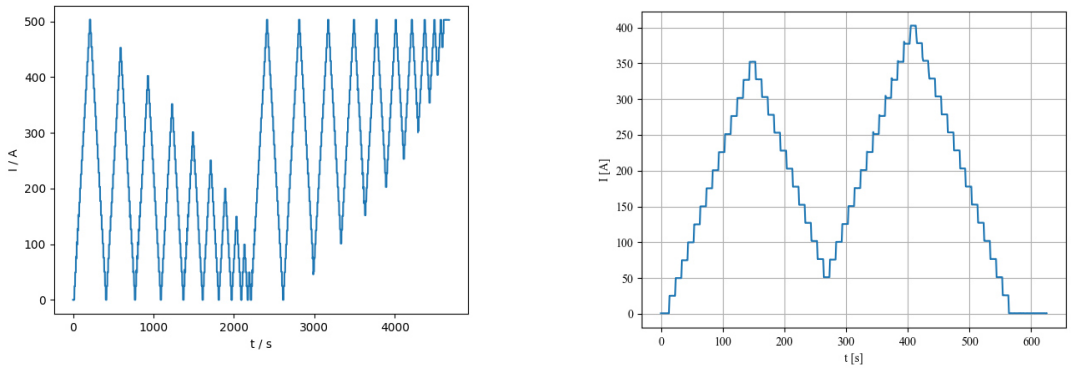

(a) (b)

Dissemination Level: **Public**

This project has received funding from the European Union's Horizon 2020 research and innovation programme under the Marie Skłodowska-Curie Grant Agreement No. 764902.

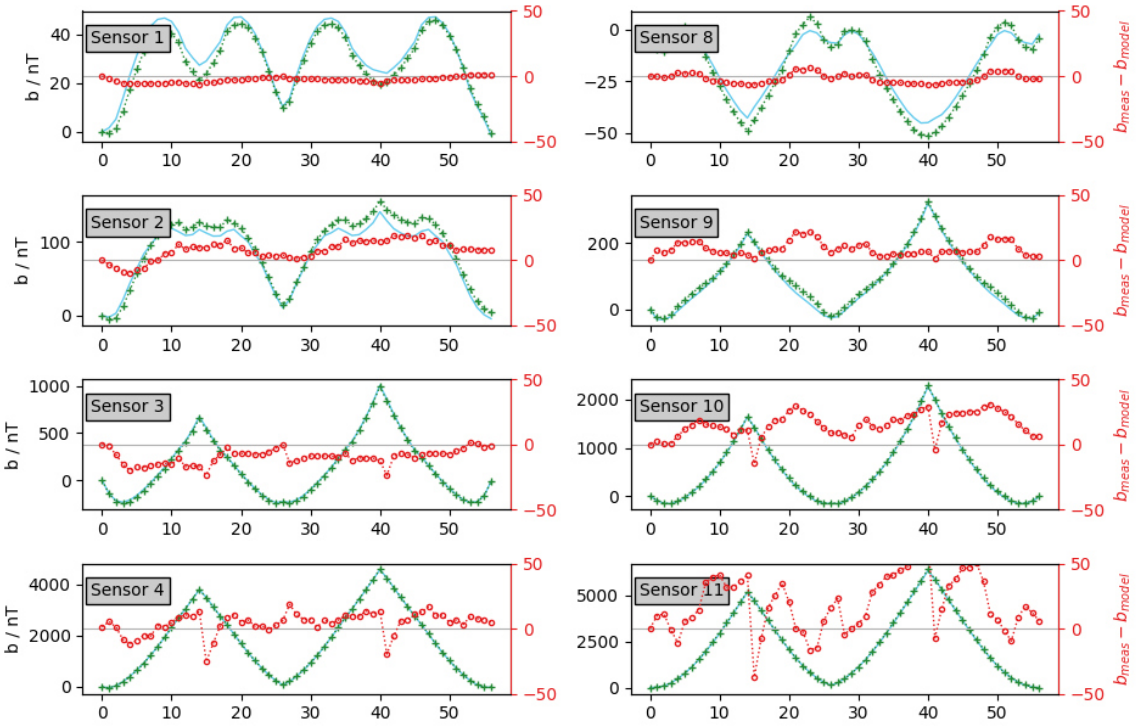

(c)

Fig. 45: (a) EMBr current training data set. (b) EMBr validation current data set. (c) The comparison between the predicted (green line) and the difference between the measured and modelled magnetic field (red line) in dependence of the current through the coils of the brake.

Because the influence of the EMBr is several orders of magnitudes larger than of the flow induced magnetic field, compensation must be performed with a high degree of accuracy. Best accuracy is achieved, if the current profile of the EMBr is known in advance and that current profile is used for compensation. For a case of an arbitrary sequence of changes of the current through the EMBr, a training phase must be performed without the flow of liquid metal. For the training, it is important to maximize the amount of sequences, in which the current increases and decreases. An example of a training sequence is shown in Fig. 45 (a). An analysis of precision of the compensation can be done with an arbitrary selected validation sequence as shown in Fig. 45 (b). For the given validation sequence, we compare the value of the measured signal to the one predicted by the hysteresis model and plot it in Fig. 45 (c).

The method for compensation of the effects of the EMBr is a crucial part in order to implement a functioning flow controller, because otherwise a reasonable reconstruction of the flow field is not possible. At the present state, the compensation works very well as a post-processing step, when all information is available and additional drifts can be compensated. From the reconstructed velocity field, the position of the impingement point can be extracted by analyzing the reconstructed vertical velocity component close to the narrow faces of the mould. The impingement point is characterised by a change of the sign of the vertical velocity. While above the jet the fluid flows upward, characterized by positive value of the vertical flow component, the fluid flows downward below the jet, resulting in a negative sign of the vertical velocity component. Fig. 46 shows the impingement point of the jet in dependence of

Dissemination Level: **Public**

This project has received funding from the European Union's Horizon 2020 research and innovation programme under the Marie Skłodowska-Curie Grant Agreement No. 764902.

the amplitude of the brake. These results fit well in the already designed control strategies, where the jet angle should be controlled and monitored.

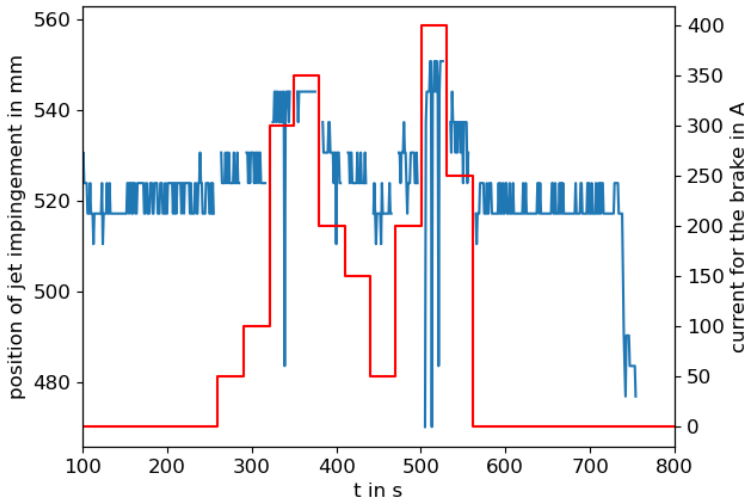

Fig. 46: Comparison of the evolution of the jet impingement at the narrow wall for varying the amplitude of the electromagnetic brake from a CIFT measurement at Mini-LIMMCAST

A real time compensation is already implemented and allows for a reliable reconstruction of the typical double roll of the flow in the mould for all amplitudes of the electromagnetic brake. From the reconstructed images, a real-time information of the impingement point of the jet can be provided, which is a basis for the flow controller described later.

3.4. Mutual inductance tomography

Magnetic induction tomography (MIT) is a technique to provide a cross-sectional imaging of conductivity distribution in a given sensing area. It makes use of eddy current principle and mutual induction measurement. The sensors are placed around the region of interest (ROI) providing a set of pairs combination data. A system of linear equation can be defined to provide a relationship between the measurement values and conductivity vector. Sensitivity matrix describes the change of measurement data related to the change of conductivity. The inversion process is then used to reconstruct the conductivity distribution. Fig. 47 illustrates this principle.

This project has received funding from the European Union's Horizon 2020 research and innovation programme under the Marie Skłodowska-Curie Grant Agreement No. 764902.

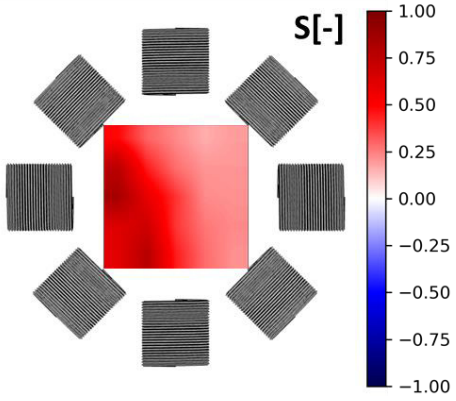

$$\nabla \times \frac{1}{\mu} \nabla \times \boldsymbol{A} + j\omega\sigma\boldsymbol{A} = \boldsymbol{J_s}$$

$$v_{det} = -j\omega M i_{exc}$$

$$\boldsymbol{V} = \boldsymbol{SK}$$

$$\boldsymbol{K} \approx \left(\boldsymbol{S^T S} + \lambda \boldsymbol{R}\right)^{-1} \boldsymbol{S^T V}$$

Fig. 47: Principle of magnetic induction tomography (MIT)

In order to obtain a set of induced voltages from mutual induction between coils in 8-coil array, the measurement system is designed. A multiplexer is required to perform a selective switching for virtually rotating the multi-channel sensors. Signal generation, switch control, and signal acquisition are the common functionalities for the MIT system.

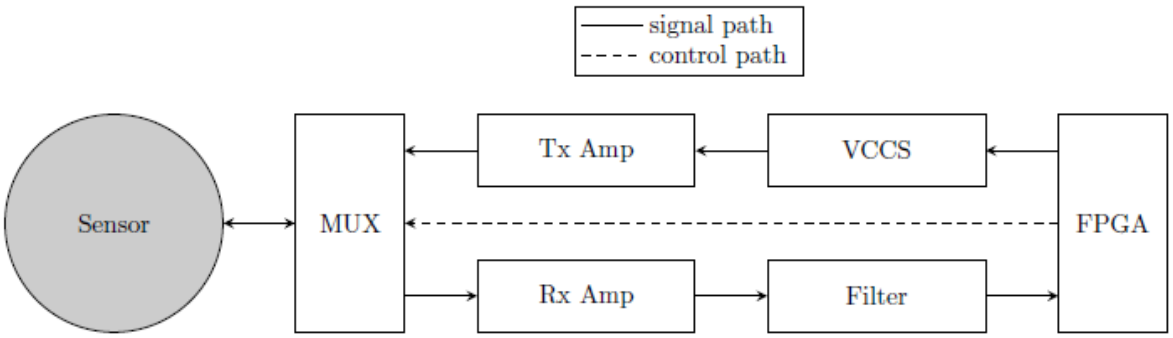

Fig. 48: Block diagram of the MIT hardware system

Fig. 48 shows the diagram of the hardware electronics. The field-programmable gate-array (FPGA) module has a capability of generating both source and reference signals to conduct a synchronous detection. Additionally, 14-bit analog-to-digital converters (ADCs) are integrated with a high sampling rate for a direct full-wave acquisition. The module also controls the multiplexer (MUX) through digital input-output ports. A transmission control protocol (TCP/IP) connection is established between the module and a computer for sending and receiving commands and data through ethernet.

This system consists of transmitting and receiving lines. At the transmitter, a voltage-controlled current-source (VCCS) converts the source's sinewave voltage into ac current. Since the module can only generate a sinewave with a maximum amplitude of 1 V, a subsequent current buffer (Tx Amp) should be added. This buffer provides a booster for the current to be injected into low-impedance load such as coils. On the other hand, the receiver part consists of an instrumentation amplifier (Rx Amp) for detecting an induced voltage on the coil. Besides gain function, the Rx Amp also has a DC cancellation to reject an offset which

This project has received funding from the European Union's Horizon 2020 research and innovation programme under the Marie Skłodowska-Curie Grant Agreement No. 764902.

may occur from the receiving signal. The stage is followed by passive filters that suppress the signal below set lower cut-off (100 Hz) and upper cut-off (100 kHz) frequencies.

The signal generation, switching control, and signal acquisition are dictated by python script. This software on the computer sets the frequency operation and the number of measurement cycle. Once the measurement is completed, the program will perform a demodulation and arrange the data accordingly. As a result, amplitude, phase, real, and imaginary components are obtained for all measurement indices. Since the demodulation is performed digitally in software after all the detection sensors' raw signals are acquired, with switching and interfacing time, the process takes approximately 10 s for a complete frame.

For the lab demonstration purpose, the MIT sensor is firstly tested in static condition. The submerged entry nozzle (SEN) with inner D=12 mm is filled with the liquid metal GaInSn (full) and then a plexiglass rod (d=6 mm) is inserted to simulate the gas void.

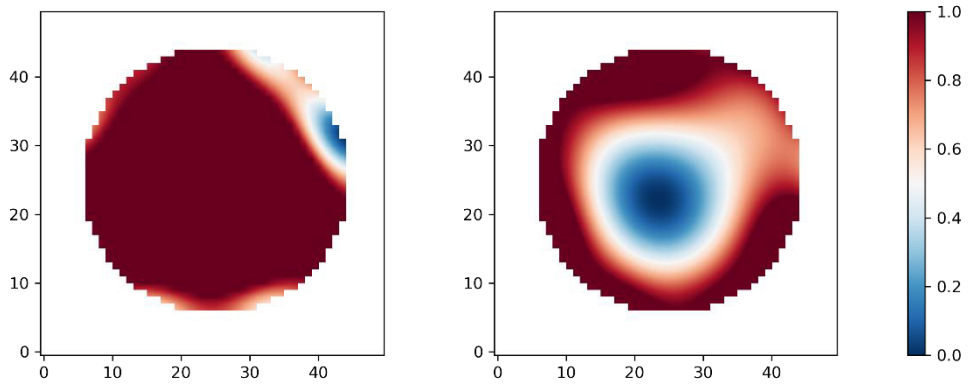

Fig. 49: Reconstruction in static experiments: (Left) Full liquid metal. (Right) Rod inclusion at the centre location.

Fig. 49 shows the reconstruction results where 50x50 pixels are illustrated into a circular imaging area of 1257 pixels ROI. By applying threshold, the liquid metal part is assigned the value of 1 (red) whereas the void/rod is 0 (blue). In the case of full liquid metal, some artifacts occur around the periphery which may be caused by reconstruction effect or the presence of gas/impurity/oxide entrapment inside the SEN. For a case with inclusion, subtraction is applied to the reconstruction image with full case and reconstruction image with inclusion case. The rod inclusion appears in the image of low value and the inferred area fraction of void is 0.35, which is close to the actual rod/SEN area fraction.

Static test results mean that the MIT system is capable of detecting and imaging the inner gas void in the liquid metal jet. This aims to quantify the gas/liquid fraction for two-phase liquid metal and argon gas flow experiments.

Installed on the Mini-LIMMCAST, the sensor is calibrated with an empty SEN (reference background). The measurement is conducted for 20 data frames, giving an average signal-to-noise ratio (SNR) of 51 dB. This SNR level along with synchronous demodulation (frequency-locked) is sufficient for the liquid metal measurement purpose.

This project has received funding from the European Union's Horizon 2020 research and innovation programme under the Marie Skłodowska-Curie Grant Agreement No. 764902.

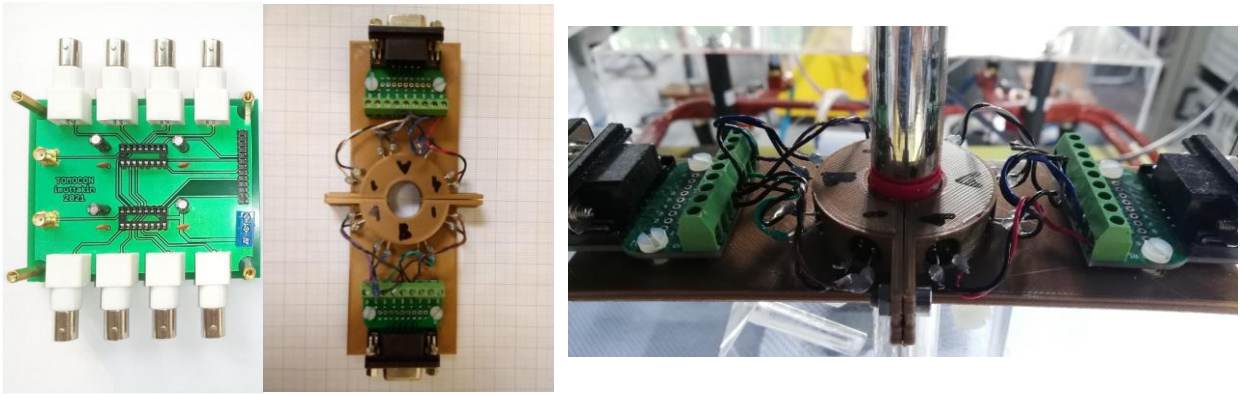

(a) (b)

Fig. 50: Top-view of the MIT electronics (a) and sensor setup installed on the SEN (b)

Fig. 50 shows the MIT sensor and system setup. Subsequent measurements are taken when starting the flow and when the flow is at the steady condition.

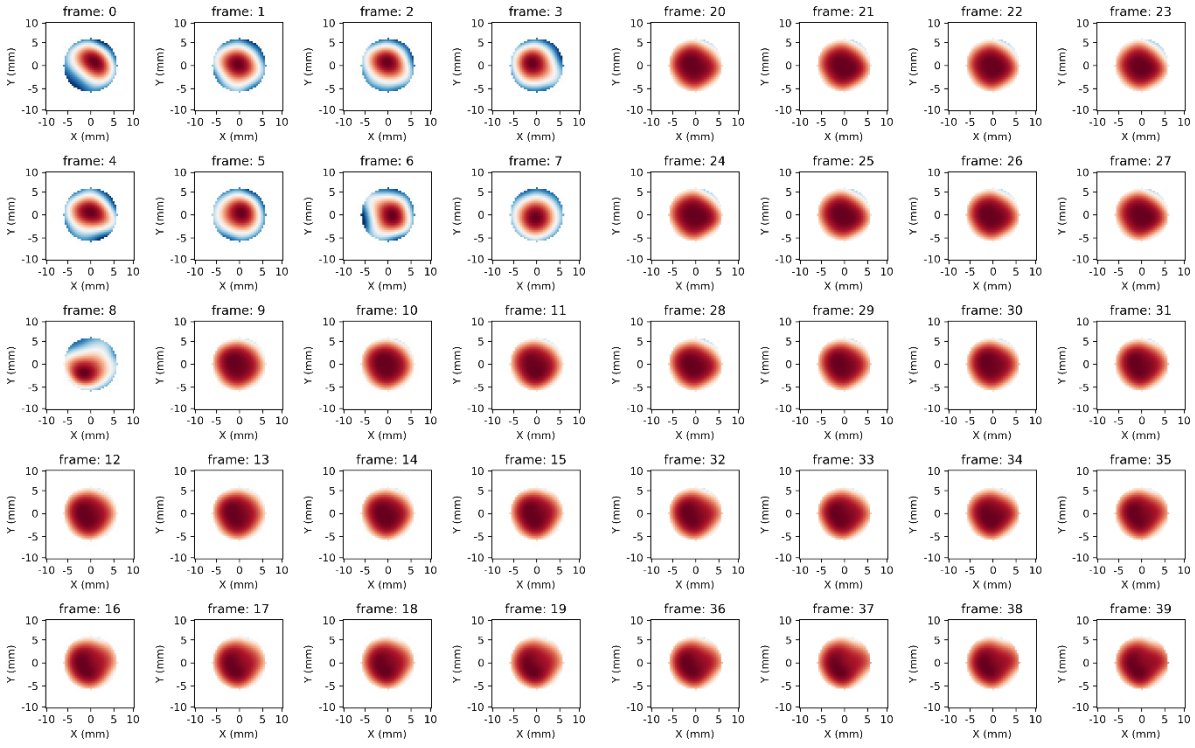

(a) (b)

Fig. 51: Captures of the reconstruction of flow in the SEN: (a) Starting flow, (b) Steady flow.

Fig. 51 shows frame captures of spatial reconstruction at the SEN cross-section. In the first 20 frames at starting flow (a), it can be seen that the SEN is being filled (frame-0 to frame-8) and becoming full at frame-9. Once the flow is steady, another 20 frames are captured (b), where the images consistently show the full SEN in a single-phase flow.

Dissemination Level: **Public**

This project has received funding from the European Union's Horizon 2020 research and innovation programme under the Marie Skłodowska-Curie Grant Agreement No. 764902.

Flow progression is also indicated on both norm data and reconstructed values (Fig. 52).

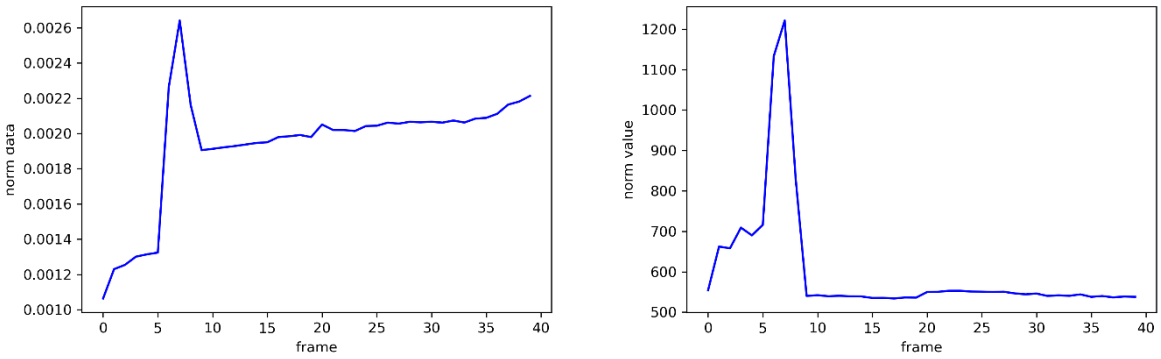

Fig. 52: Norm data (left) and norm reconstruction values (right)

The data is the difference between induced voltages during flow and induced voltages at calibration (empty SEN), whereas the reconstruction value is taken from the inversion result. A norm for vectors with the order of 2 is applied. On a frame-by-frame basis, the different trend for starting flow (changing) and steady flow (consistently full) can be seen.

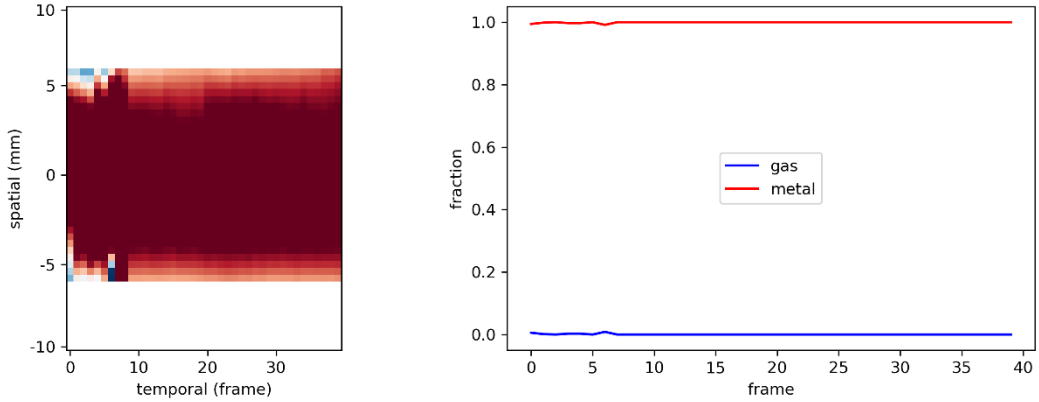

Fig. 53: Spatio-temporal flow (left) and metal-gas fraction (right)

Fig. 53 (left) depicts the spatio-temporal flow (sliced at Y=0) combining starting and steady flow frames. It shows the progress of the flow from partially filled to fully filled. The quantification of metal-gas is plotted in Fig. 53 (right) where both metal and gas fractions according to the frame number are shown in the graph.

The results demonstrate that the MIT sensor and system could provide (in principle and based on the attempted test) a cross-sectional imaging of the liquid metal flow and quantify the metal/gas fraction. Tomographic data/image as well as a SEN filling profile would be useful for control implementation. However, without another measurement or imaging system as secondary comparison, it is also difficult to verify the reconstructed flow because of the wetting and opacity of the SEN. Furthermore, the challenges remain for the dynamic liquid metal two-phase flow measurement.

Dissemination Level: **Public**

This project has received funding from the European Union's Horizon 2020 research and innovation programme under the Marie Skłodowska-Curie Grant Agreement No. 764902.

In order to penetrate into liquid metal with a high electrical conductivity, the operating frequency of the excitation-detection signal should be kept low. This leads to a relatively weak measured signal. If only outer interface or stratified flow detection is required, a higher frequency may be feasible. On the other hand, electromagnetic measurement demands a precise installation. In the case of 8-coil array circumventing a circular sensing space, any misalignment (e.g. coordinate, angle between coils) will distort the data. Artifacts could also come from a mechanical source such as movement/vibration. A possible solution is integrating the sensor construction with the SEN. Another issue is cross-sensitivity to devices in the demonstrator environment. There are other electromagnetic measurements and actuators that add 'noises' to the MIT sensor/system. A highly linear measurement electronics with the interference rejection method should be used.

For comprehensively capturing dynamic two-phase flow, where the liquid metal velocity reaches 1 m/s with small sensor's size (coil diameter 5 mm), around 200 fps (frame-per-second) measurement speed is required. A sequential measurement of 28 mutual induction values at 1 kHz could not catch the flow dynamic. Parallel measurement strategy and/or a different magnetic sensor can be considered. Moreover, small distributed inner bubbles are difficult to detect and reconstruct. The multi-frequency method, by-passing reconstruction, or machine learning approach for quantification are the future directions.

3.5. Control strategies

Because in the beginning of the project CIFT was not able to detect the flow features when the amplitude of the EMBr is changed, we used Ultrasound Doppler Velocimetry (UDV) data for the first design of the controller. UDV provides a fine spatial as well as temporal resolution of the velocity field in the melt. Based on the data set, two model predictive controllers (MPC) were successfully developed, which allow controlling the velocity close to the free surface or the angle of the jet leaving the ports of the SEN.
Recently, an implementation of the compensation procedure became available, which allows the investigation of the flow using CIFT. However, it turned out that the use of the controllers developed based on UDV data are not usable, because the reconstructed velocity by CIFT has a lower spatial resolution in comparison to UDV. Moreover, we cannot record the information of the flow during the current change of the EMBr due to the nature of inductive measurements. This makes it less viable to design a functional model predictive controller. Considering the aforementioned limitations of the measurement technique, the focus was shifted from designing the MPC to a controller tasked with disturbance rejection.
Introducing a disturbance that is significant enough to be detected by CIFT proved to be a challenging task due to inherent robustness of the laboratory setup. Commonly occurring disturbances of an industrial process that we are able to model, such as the increase of the flow rate, introducing Argon gas phase, and inducing level fluctuations did not yield in significant disturbances to the flow to develop a controller. However, introducing an obstacle that deflects the jet at a steeper angle generated an asymmetric flow that was possible to be detected by CIFT. The asymmetry was even more exaggerated when the EMBr was turned on. The drawing of the obstacle and its position in relation to the SEN is shown in Fig. 54.

Dissemination Level: **Public**

This project has received funding from the European Union's Horizon 2020 research and innovation programme under the Marie Skłodowska-Curie Grant Agreement No. 764902.

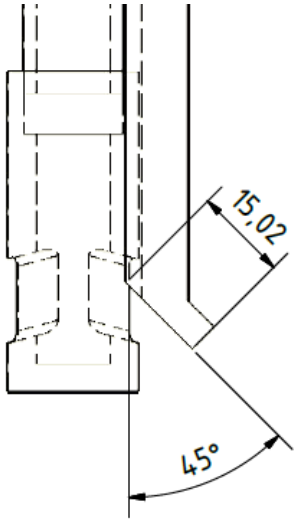

Fig. 54: Clogging model

The obstacle at the SEN outlet is designed to model the clogging of the outlet port. In literature, this clogging is usually modelled by reducing the port size [1-3]. However, by adding an additional deflection at 45° we exaggerated the observed asymmetry in the flow in order to easier detect it during real-time experiments.
A simple scenario of detecting the flow asymmetry is depicted in Fig. 55. In this experiment a dependence of clogging and EMBr current of 200 A was investigated. A clear asymmetry in flow can be observed once the clogging is introduced, and when the EMBr is active, this asymmetry is increased drastically.

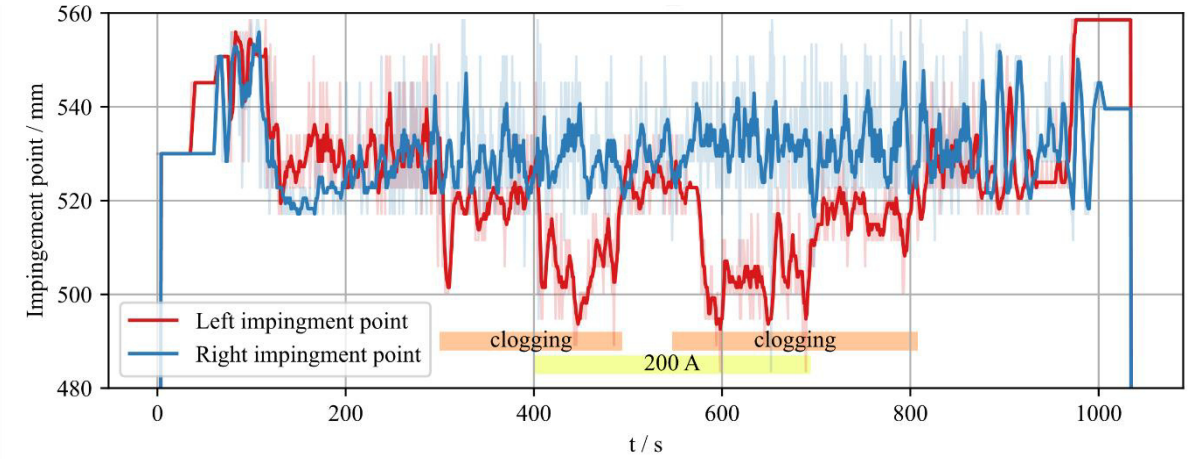

Fig. 55: Control scenario identification experiment. Jet impingement position at the left and right side of the mould with marked clogging and current time frames

In the industrial process of steel casting, the operating parameters of the EMBr are determined empirically either from plant measurements or numerical simulations, and are tied to product recipes. However, at any time during casting clogging of the SEN can occur so that the selected scenario is realistic to expect. Clogging generally increases over a period of time, but for convenience we model it as an instantaneous occurrence.

Dissemination Level: **Public**

This project has received funding from the European Union's Horizon 2020 research and innovation programme under the Marie Skłodowska-Curie Grant Agreement No. 764902.

Based on the identification experiments we designed a controller that will turn off the EMBr, when the EMBr is operating and clogging occurs. Fig. 56 presents the schematic of the controller implemented in MATLAB Simulink. The input of the controller is the position of the jet impingement extracted from the reconstructed velocity field for both narrow sides. The control decision is based on the absolute difference of the filtered impingement position for both the left and right side of the mould. Filtering of the difference is done by running a mean average filter. The absolute difference between the jet impingement position is the input to a relay operator, where the output is true, when the difference reaches given high threshold value, and it is false, when the input difference is below a given low threshold. The output from the relay operator is delayed for a set amount of measurement samples. If this and any other conditions are satisfied, a controller will change the EMBr current to a predetermined value.

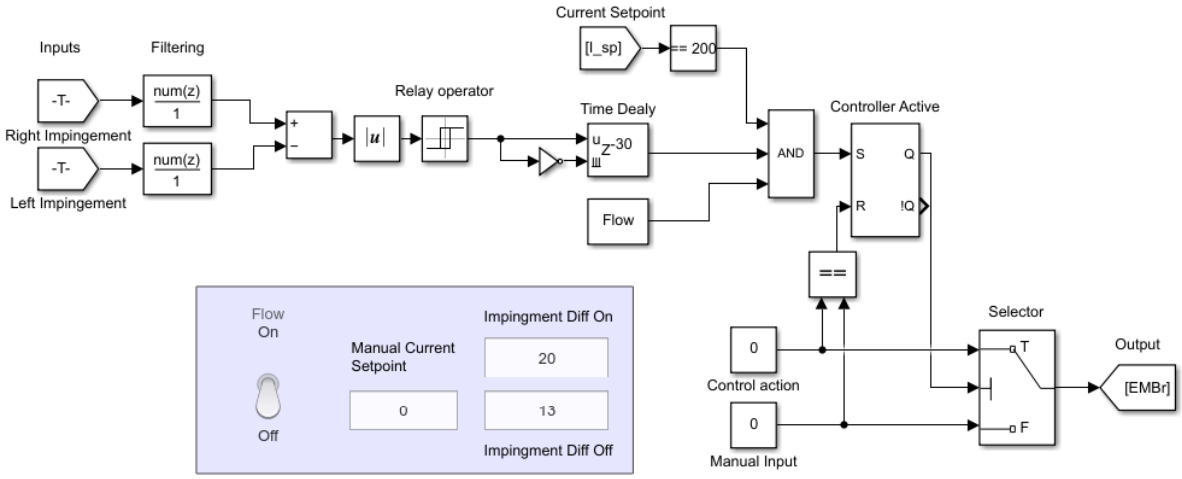

Fig. 56: Controller implemented in MATLAB Simulink

3.6. Results

In order to supply the data to the controller a real-time data evaluation pipeline has been established, as depicted in Fig. 57. The pipelines consist of three major parts: Real-time demodulation, real-time compensation of the EMBr, and real-time reconstruction and visualisation. Initially, the voltage induced in the coils is filtered using a low-pass filter. After filtering a real time demodulation is done by applying Lomb-Scargle procedure at the frequency of the excitation magnetic field. The resulting in-phase and out-phase voltage is converted to the magnetic field with the transfer function of the gradiometric sensing coils [5]. The sampling frequency of the demodulated magnetic field is determined by the selection of the number of periods used for demodulation. The in-phase component of the excitation magnetic field contains information about the flow. The in-phase and out-phase flow induced magnetic field is then sent to the real-time compensation of the EMBr which runs a real time discrete Krasnosel'skii-Pokrovski model of hysteresis. Based on the current and past values of the EMBr a compensation value is determined and subtracted from the flow induced magnetic field. The model inherently introduces some errors due to the difficulty to have a constant response of

Dissemination Level: **Public**

This project has received funding from the European Union's Horizon 2020 research and innovation programme under the Marie Skłodowska-Curie Grant Agreement No. 764902.

the current source of the EMBr both for training and for compensation. This error is increased with every current change of the EMBr. To increase the accuracy and reduce the required training time, we train our compensation model with the data that we predetermine for that experiment. The compensated flow induced magnetic field is then sent to the real-time reconstruction. The real-time reconstruction is done by precomputation of the inverse matrices for predefined regularization parameters [6]. In case of the Mini-LIMMCAST model the regularization parameter does not differ drastically from one time step to another, therefore only one regularization parameter is selected and used for all reconstructions. From the reconstructed velocity field we extract the information of the jet impingement position and send it directly to the controller implemented in Matlab SIMULINK. Fig. 57 depicts the data flow diagram.

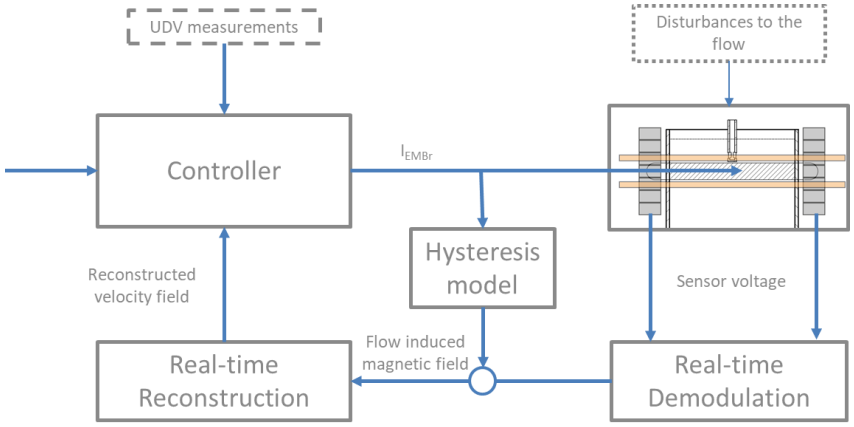

Fig. 57: Controller block diagram

Communication interfaces between the individual programs are done using TCP/IP sockets and are shown in Fig. 58. This sort of connection allows for an ease of getting information from any step of the data processing to another one. The hardware communication to the current sources for the EMBr is realized over a serial RS232 port. The total time delay between the change in the flow and the final reconstruction is approximately two seconds.

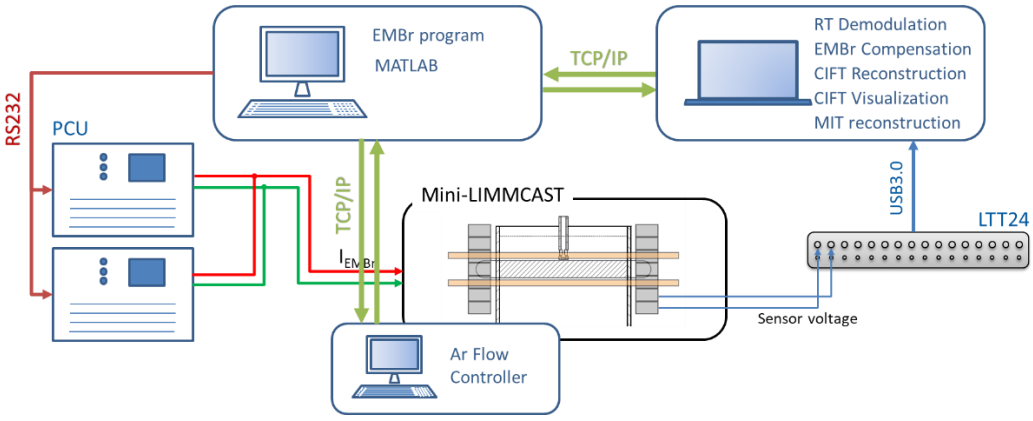

Fig. 58: Communication diagram

To validate the controller design and the functioning pipeline we set a test case where the EMBr current is set to 200 A, when the flow is stable. Then we introduce the obstacle for

Dissemination Level: **Public**

This project has received funding from the European Union's Horizon 2020 research and innovation programme under the Marie Skłodowska-Curie Grant Agreement No. 764902.

modelling clogging. If the difference remains over 15 s larger than 20 mm, then the EMBr is turned off (see also Fig. 56).

An exemplary recording of one of the experiments is shown in Fig. 59. In this experiment the EMBr is turned off by the controller at t = 347 s when clogging occurred at t = 312 s. During the second part the controller turned off the EMBr at t = 529 s, for clogging introduced at t = 500 s. The controller successfully managed to detect the asymmetry in the flow and turned off the EMBr.

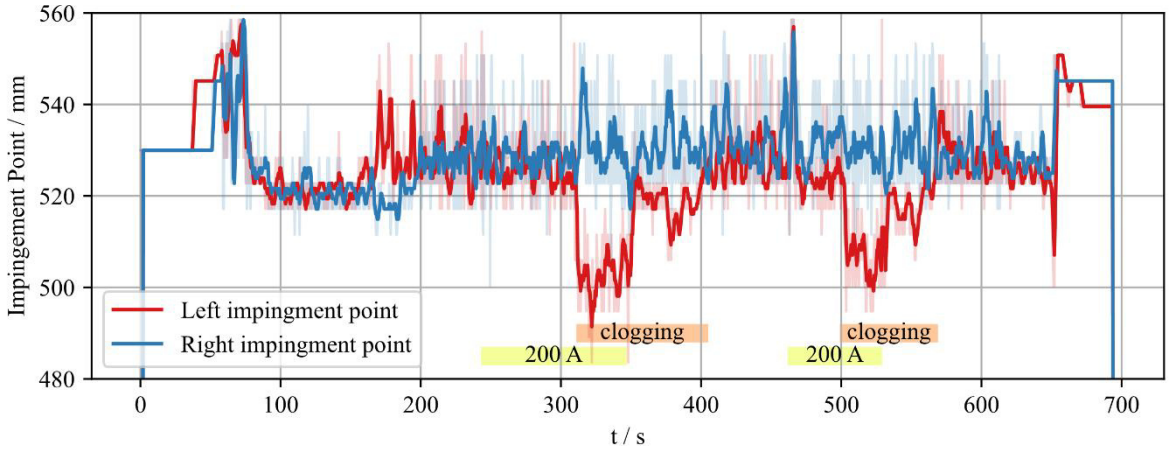

Fig. 59: Recording of the jet impingement position for a controller validation experiment

Besides the extraction of the impingement position from the reconstructed velocity field, the position can also be directly estimated from the measured magnetic field. When the induced magnetic field for one time instance is plotted in dependence of the vertical position of the magnetic field sensors, the magnetic field changes its sign close to the jet impingement position. A comparison of both methods is shown in Fig. 60. The straight lines indicate the position of the jet impingement extracted from the reconstructed velocity, while the dotted lines indicate the jet impingement position extracted directly from the magnetic field measurements without the use of the reconstruction. The agreement is quite remarkable so that both methods could be used. However, the reconstruction takes the entire flow field as well as the divergence of the flow into account. This considers the actual sizes of the upper and lower vortices, which determine the exact jet impingement point. Thus, it can be assumed that the extraction of the jet impingement point from the reconstructed velocity field is more accurate.

Dissemination Level: **Public**

This project has received funding from the European Union's Horizon 2020 research and innovation programme under the Marie Skłodowska-Curie Grant Agreement No. 764902.

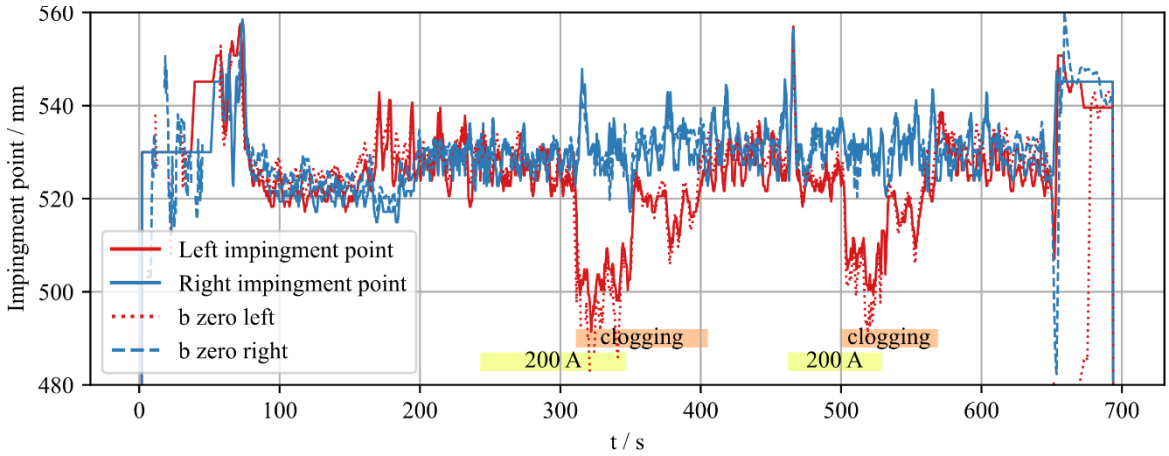

Fig. 60: Comparison between the jet impingement point from velocity field reconstruction and interpolation of position where the flow induced magnetic field is zero

The current implementation of the controller, albeit simple in nature, is a significant progress in using tomographic measurement techniques as a controller backbone. Up to now, no comparable flow measurement technique for continuous casting is available. CIFT offers unique insight into the flow structure of the mould, and with that, a new way to monitor and control the process.

Improving controller strategies further consists of increasing the measurement accuracy, robustness and speed, and identifying additional key flow features that are of interest for an efficient process. The next logical step is implementing a PI/PID controller and gradually increasing the complexity of the control algorithm as one of the popular methods for tuning PID controllers is based on the relay control similar to what is shown in our experiments [4].

3.7. Conclusions and outlook

The lab demonstration for the continuous casting model showed for the first time ever that an electromagnetic actuator can be controlled on the basis of the current flow structure in the mould. It could be shown that the contactless inductive flow tomography is able monitor the flow structure in real time in the mould of a continuous caster and can be integrated into a control loop for an EMBr of ruler type. The major challenge was the real time compensation of the effects of the change of the amplitude of the EMBr on the CIFT measurement system. These effects are up to three orders of magnitude larger than the flow induced signal. Furthermore, the precise real time demodulation of the measured induced magnetic field was implemented. The developed communication network based on TCP/IP allows for an easy extension of the control loop with additional sensors and actuators. The maximum time delay was 2 seconds. For continuous casting this delay is sufficient, because typical instabilities of the flow in the mould have a longer period. As a simple but realistic test case, nozzle clogging was simulated by introducing an obstacle, which partly blocked one of the outlet ports of the SEN. Under these circumstances, the impingement position of the jet moves downward, when the EMBr is active. This undesired lower position of the impingement point can be lifted again, if the EMBr is switched off. With this proof of concept, a working control loop implementation became available, which is a valuable tool to investigate more sophisticated control strategies.

Dissemination Level: **Public**

This project has received funding from the European Union's Horizon 2020 research and innovation programme under the Marie Skłodowska-Curie Grant Agreement No. 764902.

The focus of future investigations will be on the generation of a map of typical flow instabilities, which might be induced by higher liquid metal flow rates, argon gas flow rates, nozzle clogging, bulging of the strand. By using more sophisticated actuators, like local EMBrs, which can influence the flow on both sides of the SEN independently, or electromagnetic stirrers at the top or close to the outlets of the SEN, new control strategies tailored for the typical flow instabilities can be developed. Similar electromagnetic actuators are already available for continuous casters. Besides, new arrangements of the excitation coil and the magnetic field sensors for the CIFT sensor should be investigated. The new sensors should have the potential to be applied in an industrial environment and should be less sensitive to changes of the amplitude of the EMBr. Furthermore, the compensation of the effects generated by the ferromagnetic parts have to be investigated, including the enhancement of the magnetisation model and the development of an additional inductive sensor, which detects the present magnetisation of the yoke. Last but not least, a more sophisticated solution of the inverse problem might be developed by taking the viscosity or density of the fluid into account. The development of the MIT system at the SEN will need a parallel data acquisition system to allow for higher frame rates. An additional interesting feature would be the estimation of the liquid metal flow rate in the SEN. A validation of such a sensor could be done using x-ray radiography. Both sensors, CIFT and MIT, have the potential to be applied also in industry, because they do not need any contact to the hot metal and can easily operate in a dusty and hot environment.

3.8. References

[1] B. Rout, R. Singh, S. K. Choudhary, Development and Application of Nozzle Clogging Index to Improve the Castability in Continuous Slab Casting. *International Conference on Advances in Refractories and Clean Steel Making,* 2013.

[2] S.-M.Cho, S.-H. Kim, R. Chaudhary, B. G. Thomas, H.-J. Shin, W.-R. Choi, S.-K. Kim, Effect of Nozzle Clogging on Surface Flow and Vortex Formation in the Continuous Casting Mold. *Iron and Steel Technology*, 9 (7), pp. 85-95 (2012).

[3] L. Zhang, Y. Wang, X. Zuo, Flow Transport and Inclusion Motion in Steel Continuous-Casting Mold under Submerged Entry Nozzle Clogging Condition. *Metallurgical and Materials Transactions B*, 39, pp. 534-550 (2008), https://doi.org/10.1007/s11663-008-9154-6.

[4] C. C. Hang, K. J. Astrom, Q. G. Wang, Relay Feedback Auto-Tuning of Process Controllers — a Tutorial Review. *Journal of Process Control*, 12 (1), pp. 143–62 (2002), https://doi.org/10.1016/S0959-1524(01)00025-7.

[5] M. Ratajczak, T. Wondrak, Analysis, Design and Optimization of Compact Ultra-High Sensitivity Coreless Induction Coil Sensors. *Measurement Science and Technology*, 31 (6), 065902 (2020), https://doi.org/10.1088/1361-6501/ab7166.

[6] T. Wondrak, R. T. Jacobs, P. Faber, Fast Reconstruction Algorithm for Contactless Inductive Flow Tomography. *10th International Conference on Advanced Computer Information Technologies (ACIT)*, 217–20 (2020), https://doi.org/10.1109/ACIT49673.2020.9208853.

This project has received funding from the European Union's Horizon 2020 research and innovation programme under the Marie Skłodowska-Curie Grant Agreement No. 764902.

4. Tomography-Controlled Batch Crystallization

4.1. Objectives

There has been a recent growth in the demand for precipitation processes in chemical industries that lies on the requirement of energy-efficient operation and sustainability [1]. In reactive crystallization systems, the generation rate of supersaturation is very fast, and the reaction regimes are instantaneous that makes it difficult to achieve a robust process control in terms of solid particle stability and particle size distribution [2]; moreover, the implementation of practical and high-fidelity feedback control strategies such as nonlinear model predictive control becomes more challenging [3,4]. Instantaneous reactions are controlled by molecular diffusion [5], and reaction terms can also be neglected while conducting mass transfer modeling due to the inherent speed of the chemical reaction [6]. In liquid-phase precipitation, mass transfer resistance is even smaller than in gas-liquid contacting precipitation processes and the subsequent nucleation of crystals is usually very fast [7].
In the present report, electrical resistance tomography (ERT) and ultrasound computed tomography (USCT) techniques are utilized to monitor the fast-kinetic and micron-sized crystallization process of calcium carbonate ($CaCO_3$). Even though tomographic data can provide cross-sectional representation from within a stirred tank reactor, in the current investigation, the ERT reconstructions could not be utilized due to non-deterministic and insensitive data from the crystal suspensions. Employing them for fault identification does not efficiently characterize malfunction situations. Moreover, the complex nature of the topology-based visualization renders the real-time interpretation a challenging task. The transient correlation of the reconstructions to physico-chemical phenomena of the fast-kinetic crystallization process becomes extremely limited due to a relatively slow reconstruction time and the global resolution. In summary, more research efforts are needed for image reconstructions studies in detail. On the other hand, statistical analysis of the single- and multi-electrode current measurement of the ERT provides satisfactory information from the suspension and facilitates the development of a basic signal-based alarming technique for real-time fault detection and diagnosis. The measured electrical current of a single-electrode is used as input to an in-house developed LabVIEW program for dynamic signal analysis. The measurement consistency due to the use of a single electrode from a set of ERT electrodes for malfunction identification is experimentally and quantitatively investigated based on the sensors sensitivity and signal-to-noise ratio criteria.
Alongside the ERT-based process monitoring, the USCT system is used to investigate the fast-kinetic reactive crystallization process. The offline analysis of the USCT measurements and reconstruction provides insights into the bulk particle distribution inside the stirred tank reactor and can be used as a means to estimate the settling time of the particles, suspension homogenization, and mixing phenomena.

4.2. Experimental facility

The crystallization reactor is made of plexiglass with an inner diameter of 190 mm. A plastic-made Rushton impeller is used for agitation. In the micron-sized, liquid-liquid crystallization system, aqueous CO_3^{2-} as the reagent solution flows through an inlet pipe (diameter: 2 mm) into the crystallizer containing calcium chloride. A detailed description of the CO_2 capture system and its integration with the calcium carbonate crystallization process is given in [8] and [9], respectively. The chemical reaction governing the crystallization of calcium carbonate is presented in Eq. 7.

Dissemination Level: **Public**

This project has received funding from the European Union's Horizon 2020 research and innovation programme under the Marie Skłodowska-Curie Grant Agreement No. 764902.

$$CO_{3(aq)}^{2-} + 2\,Na^{+}_{(aq)} + CaCl_{2(aq)} \rightarrow CaCO_{3(s)} \downarrow + 2\,NaCl_{(aq)} \quad (7)$$

In the process under investigation, the semi-batch feed contains a dissociated CO_3^{2-}, OH^- and Na^+ ionic solution at a pH range of 12–12.1. Carbon dioxide absorbs into the liquid solution to form CO_3^{2-} through a well-established carbon dioxide instantaneous dissolution process in NaOH solutions. Fig. 61 and 62 show a photograph and schematics of the entire experimental setup in which the ERT system is utilized for crystallization monitoring and process fault detection analysis.

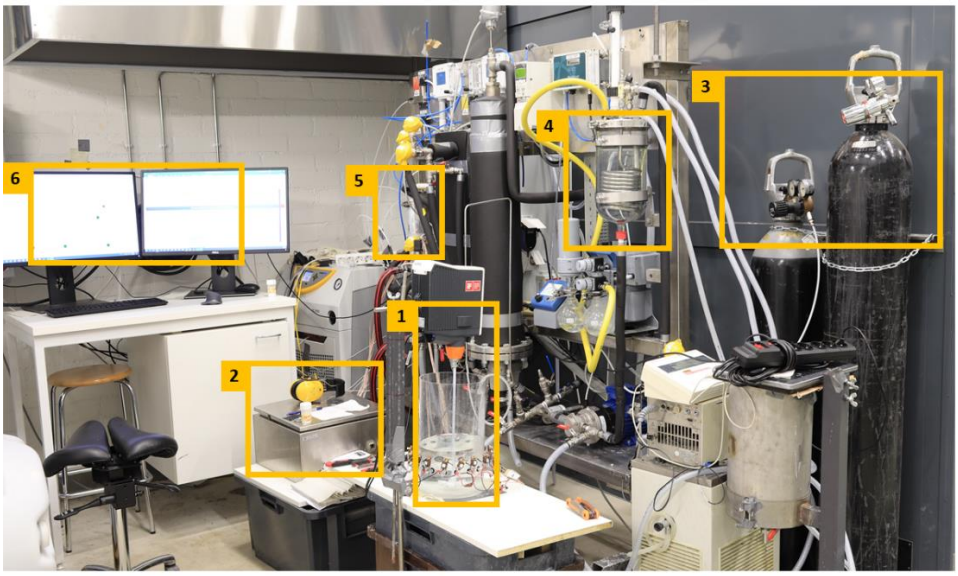

Fig. 61: Experiment facility at the LUT University pilot hall. (1) Electrical resistance tomography unit mounted around the stirred tank reactor equipped with a Rushton turbine, (2) Electronics for data acquisition and connection to a computer via Ethernet cable, (3) Air/N_2 and CO_2 bottles, (4) Glass vessel that contains absorbent liquid (NaOH) for CO_2 capture, (5) Commercial–grade hollow fiber membrane as the gas-liquid contactor, (6) Computer for process monitoring with LabVIEW software.

Dissemination Level: **Public**

This project has received funding from the European Union's Horizon 2020 research and innovation programme under the Marie Skłodowska-Curie Grant Agreement No. 764902.

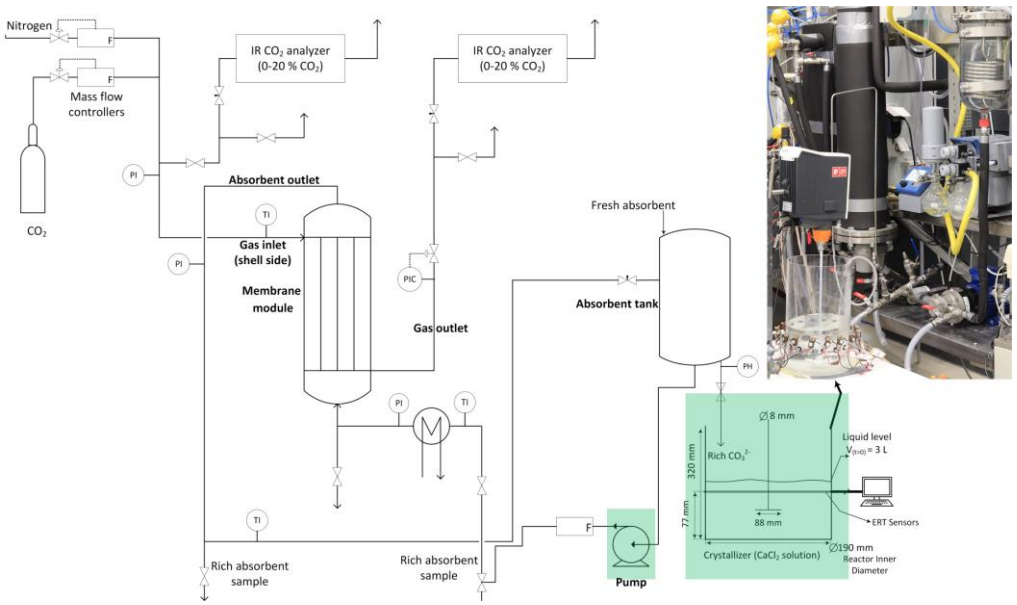

Fig. 62: Process schematics: Integrated CO_2 capture and calcium carbonate crystallization. A photograph that shows the electrical resistance tomography mounted around the crystallizer. The marked green boxes show the main components for FFD analysis.

Fig. 63 shows photographs of the experimental setup in which the USCT system is utilized to conduct process monitoring and dynamical analysis. Experiments are carried out at the Netrix facilities in Poland. Experimental plans and procedures are synchronized between the partners.

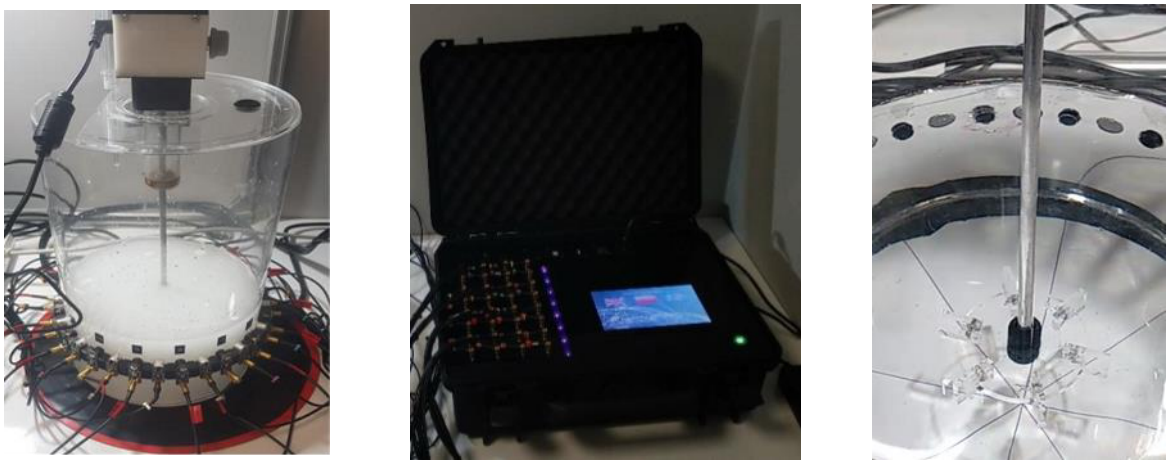

(a) (b) (c)

Fig. 63: Ultrasound experimental setup. (a) Tank, (b) measurement unit, (c) impeller.

4.3. ERT

The crystallization reactor is equipped with a single plane of 16 stainless steel electrodes mounted around the perimeter and connected to a data acquisition system (supplied by Rocsole Ltd, Finland). The utilized electrical resistance tomography is based on the injection

Dissemination Level: **Public**

This project has received funding from the European Union's Horizon 2020 research and innovation programme under the Marie Skłodowska-Curie Grant Agreement No. 764902.

of a constant electrical voltage of 2241.34 mV on one of the electrodes (i.e., source electrode), and simultaneously measuring the electrical current distribution on the remaining electrodes (i.e. sink electrodes). The source electrodes are consecutively switched from electrodes number 1 to 16 (see Fig. 64), and the measurement is recorded accordingly.
The frequency of operation is 156 kHz and the image capturing frame rate is 14.7 Hz. Even though the circular electrodes (diameter = 12 mm) are configured inside the wall of the reactor, they are non-intrusive and not interfering with the chemical reaction. Reference (background) measurements are taken for each experimental case and a Gauss-Newton is used for offline image reconstruction. Experiments are conducted at a temperature of 20 ± 2. A detailed description of the ERT system is provided in TOMOCON Deliverable No. 2.4 and in [10,11].

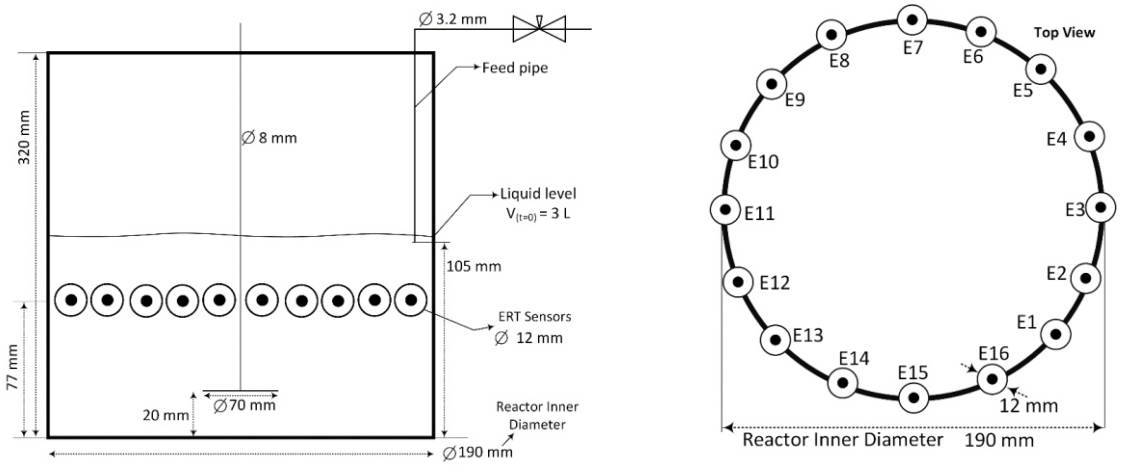

Fig. 64: Schematics of the experimental setup. (a) Dimensions of the plexiglass reactor and position of the ERT sensors. (b) Top view of the array of ERT sensors around the reactor. Feed addition pipe is located between electrodes 3 and 4 throughout the entire experiment. The initial solution volume in the tank is 3 L.

A plastic-made Rushton impeller is used for agitation; in comparison to the metal impeller, the plastic-made impeller reduces the induced noise intensity during the data acquisition process, which is favorable in terms of image reconstruction and statistical signal analysis. The impeller tip speed is kept constant at $0.37\ \mathrm{m\ s^{-1}}$ for all the experiments. Fig. 65 shows the resulting tomographs and the surface mesh of the impellers. Tomographs are obtained using the one-step Gauss-Newton reconstruction method.

Dissemination Level: **Public**

This project has received funding from the European Union's Horizon 2020 research and innovation programme under the Marie Skłodowska-Curie Grant Agreement No. 764902.

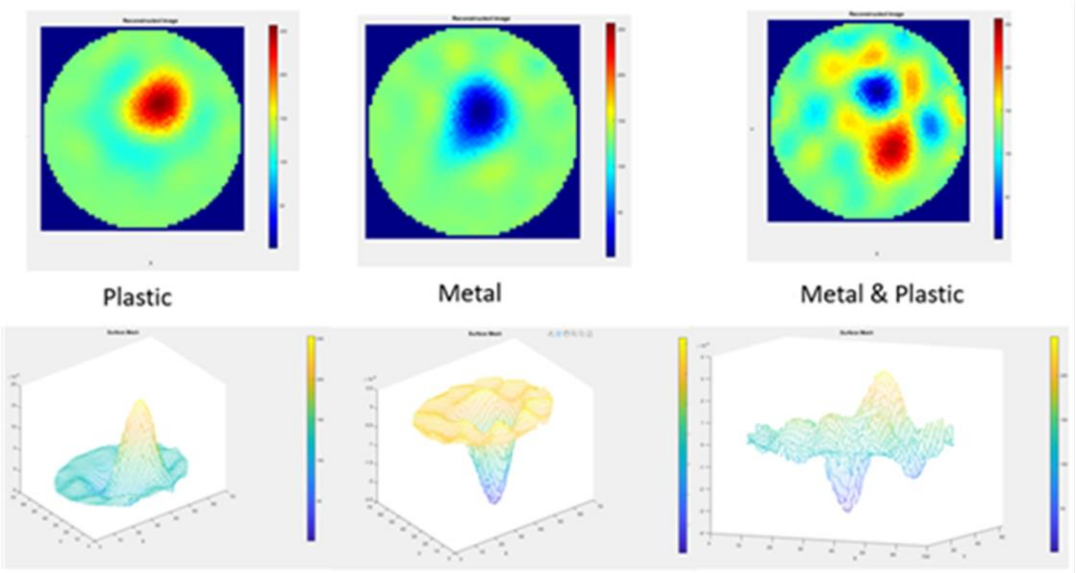

Fig. 65: Reconstructed images of the plastic impeller, metal impeller, and both the plastic and metal together along with the surface meshes. The images are reconstructed using the one-step Gauss-Newton reconstruction method and the background medium is water. It can be seen that there is a clear difference between the metal and the plastic stirrer.

4.4. USCT

The USCT imaging system consists of a circular ring of 16 transducers, an electronic hardware set-up for emitting and recording travel-time data of first arrival pulse, and computer software to analyze and reconstruct the recorded data. The main design features, structural parameters, and values of the utilized ultrasound tomography system are listed in Table 2.

Table 2: The main design features, structural parameters and values of the utilized ultrasound tomography system

Parameter	Value
Transducers' frequency	400 kHz
Number of pulses	6
Supply voltage	+72/-72 V
Pull to the ground after extortion	45.2 dB
Gain the first stage	1 V/V
Analog filter	Band-pass 350 kHz
Convert to envelope	HI
Offset-RAW signal	1.75 V
Offset-ENVELOPE signal	0 V
Number of channels	16

The developed travel-time transmission tomography method is based on the time-of-flight of the first arrival pulse. To generate the propagation model of the emitting energy, a computational model based on diffraction on the 1st Fresnel zone is utilized [12]. Fresnel

Dissemination Level: **Public**

This project has received funding from the European Union's Horizon 2020 research and innovation programme under the Marie Skłodowska-Curie Grant Agreement No. 764902.

volume or 'fat ray' tomography is an appealing compromise between the efficient ray theory tomography and the computationally intensive full waveform tomography [13]. Each recording comprises 256 measurements, accounting for 16 recordings for every one of the 16 emissions that take place. The system provides 5 frames of computed TOF values each second, hence, resulting in an overall temporal resolution of 4 frames per second (fps). Such a response over time is used for tomographic reconstruction execution in the present work and is considered adequate for a wide range of dynamical processes, like pipe-flow monitoring.
As the mixing phenomena greatly affects the dynamical state of the stirred tank reactor, it introduces noise to the system which disturbs the ultrasonic measurements. Noise is apparent in the measurements when the dynamics of the tank abruptly change. The main challenge regarding ultrasonic online measurements in mixing environments is the elimination of the "stirring noise" and the use of quantitative information without being extremely distorted. According to the experimental data, the system proved to work well in that regard. A detailed description of the ultrasound tomographic technique is provided in TOMOCON Deliverable 2.4 and [14].

4.5. Control

4.5.1. ERT-based process automation implementation for malfunction identification

An offline analysis of the tomographic reconstructions (ERT and USCT) provides ample information from the progression of the calcium carbonate crystallization process. However, the complex nature of the topology-based visualization renders the real-time interpretation and utilization of the tomographic reconstruction for an online process monitoring and control development a challenging task. In the current crystallization system, process-specific knowledge and statistical particle size distribution data obtained from several batches result in characterizing the process behavior and identifying the experimental correlation between the mixing speed, feed addition rate and $CaCO_3$ mean crystal size: An increase in the intensity of the agitation at a constant feed addition rate results in a relative increase in the average crystal size and vice versa. Hence, developing a process automation program for real-time fault detection and malfunction diagnosis when out-of-specification events occur throughout the process, delivers an efficient means to monitor the functionality of the chemical process—for instance, achieving a desired particle size distribution at specific stirring speed and feed flow rate by monitoring for the key equipment failure.
In this study, the process automation program is developed based on dynamic signal analysis (e.g. standard deviation and slope of the electrical current) from a single-electrode of the ERT system. The strategy for selecting a single ERT sensor is experimentally and quantitatively investigated based on the relative sensitivity and signal-to-noise ratio criteria. Theoretical calculations and experimental repetitions are used to analyze the statistical patterns in the measured electrical current to ensure the selection of the suitable sensor (electrode). The graphical user interface for data acquisition and fault identification is developed in the LabVIEW software environment (Fig. 66). Theoretical total ion balance modeling of the entire chemical reaction (Eq. 7) is conducted and validated based on the experimental results.

Dissemination Level: **Public**

This project has received funding from the European Union's Horizon 2020 research and innovation programme under the Marie Skłodowska-Curie Grant Agreement No. 764902.

Fig. 66: Snapshot of the main graphical user interface of the LabVIEW program, which acquires real-time ERT measurements for process automation and fault detection and diagnosis. (1) Moving average and user-controlled sample length, (2) FIFO buffer memory and visualization, (3) LabVIEW state machines, (4) The minimum runtime of the crystallization process and indicator for $CaCl_2$ status in the reactor, (5) Slope analysis and indicator for the pump status, (6) Standard deviation analysis for the operational status of the mixer.

Averaged single-electrode data from the ERT system are correlated to the mechanical failure of the stirrer through standard deviation (SD) evaluation. The measured electrical signals are averaged each 5 s and then a moving average with a time difference of 20 s is used for dynamic evaluation of the standard deviation, which provides a satisfactory performance for basic applications. According to the relation in Eq. 8, when the real-time calculation of the SD ratio criterion is greater than a pre-determined parameter, it is an indication of an abrupt change in the status of the mixer (e.g. mixer switched off):

$$\sigma_r = \frac{\sigma_{\text{mixer off}}}{\sigma_{\text{mixer on}}} \quad \text{where,} \quad \begin{cases} \text{Mixer on,} & \sigma_r < \varepsilon_{\text{mixer}} \\ \text{Mixer off,} & \sigma_r \geq \varepsilon_{\text{mixer}} \end{cases} \tag{8}$$

where σ_r denotes the mixer standard deviation ratio criterion obtained from experimental data, $\sigma_{\text{mixer off}}$ and $\sigma_{\text{mixer on}}$ are the signal standard deviation when the mixer is switched off and switched on, respectively. $\varepsilon_{\text{mixer}}$ denotes the trigger value that initiates the alert as the criteria are fulfilled. The adjustable parameters (i.e. σ_r, sampling times, etc.) are manually fine-tuned for each operating condition by trial and error procedures according to the stability and transient response of the experiment under investigation.

Dissemination Level: **Public**

This project has received funding from the European Union's Horizon 2020 research and innovation programme under the Marie Skłodowska-Curie Grant Agreement No. 764902.

Similarly, ascending and descending slope of the averaged electrical current from the designated electrode are used to monitor the pump and feed addition status. The formation of the solid particles in the solution decreases the mean electrical current of the solution throughout the feed addition window. The average slope of the electrical current is continuously determined as follows:

$$C = \frac{I}{\Delta t} \tag{9}$$

where I is the electrical current (microampere, μA), C is the average slope of the electrical current ($\mu A\ min^{-1}$) and Δt is the measurement time (minute). An abrupt decrease in the continuous slope measurement toward a plateau (i.e. zero slopes) indicates a situation where the feed addition pump is switched off, as expressed in Eq. 10:

$$K = \frac{C_{pump\ on}}{C_{pump\ off}} \quad \text{where,} \quad \begin{cases} \text{Pump on (feed addition)}, & K < \varepsilon_{feed} \\ \text{Pump off (no feed addition)}, & K \geq \varepsilon_{feed} \end{cases} \tag{10}$$

where K is the slope factor and ε_{feed} is the threshold value that triggers the alert concerning the pump statues. A time difference of 30 s is used to evaluate the moving average of the incoming electrical signals for the pump status. Table 3 lists the threshold values for ε_{mixer} and ε_{feed} that are used during the experimental investigation.

Table 3: Threshold values to trigger the alert system for mixer and feed addition pump malfunctions. Averaged values obtained from multiple experiments with their standard deviation are reported.

Equipment	Parameter	Threshold value	The time difference for moving average, s
Mixer	ε_{mixer}	1.9 ± 0.1	20 s
Pump	ε_{feed}	15 ± 4	30 s

4.6. Results of the lab demo

4.6.1. ERT sensitivity analysis and sensor selection

Fig. 67 displays the multi-electrode current measurements for different concentrations of the water-$CaCl_2$ system. The mean of averaged electrical current from 16 electrodes is used for an approximate quantification of the total current of the solution. Results show that the distinguishability and sensitivity range of the utilized ERT system becomes limited by operating at a relatively higher $CaCl_2$ concentration.

Dissemination Level: **Public**

This project has received funding from the European Union's Horizon 2020 research and innovation programme under the Marie Skłodowska-Curie Grant Agreement No. 764902.

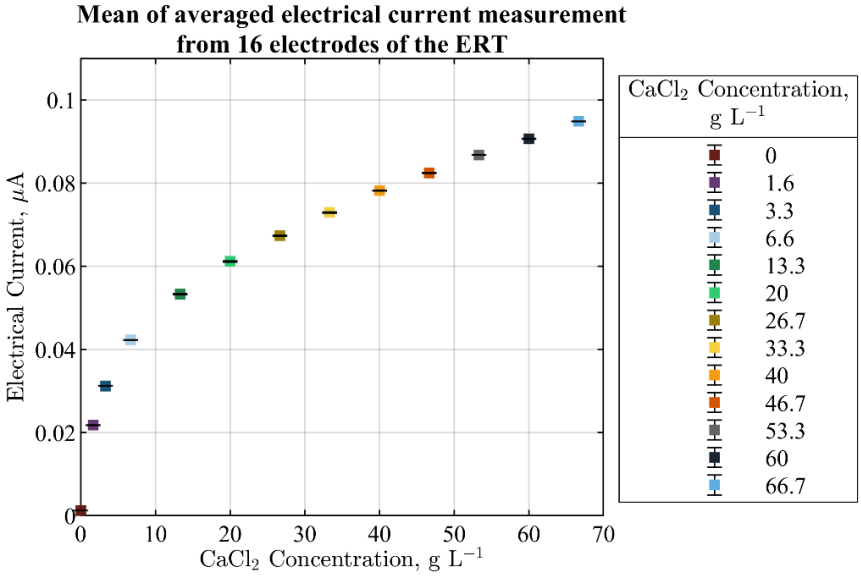

Fig. 67: Mean of averaged current measurement from 16 electrodes of the ERT for quantification of the total current of the solution. Different concentrations of $CaCl_2$ solutions are used for a 1-minute measurement. Solutions are stable with no mixing.

The additional statistical analysis of the electrical currents from the ERT electrodes demonstrates a continuous pattern in the acquired signals that can be linked to physio-chemical changes of the precipitation process. The effects of the mixer status (i.e. switched on/off) can be observed through standard deviation analysis. Fig. 68 shows the variation in electrical current measurement based on a single- and multi-electrode analysis induced by the change in stirrer conditions. Upon switching off the mixer at times 3, 6, 8, and 9.5 minutes into the process, an abrupt increase in the relative standard deviation of the measurement data is recorded. A threshold value of 1.9 ± 0.1 is assigned to the mixer SD ratio (σ_r) for monitoring and reporting the stirrer operating status (see Table 3). The assigned value to σ_r is obtained through experimental repetitions and trial and error procedures. If the dynamic SD ratio measurements rise above the threshold value, it triggers an alert indicating the mixer is switched off.

The rise in signal amplitude because of a change in the mixer status is robustly observed over electrode no. 2 (Fig. 68 b) – a quantitative analysis of the standard deviation of all the electrodes of the utilized ERT system for the selected batch experiment is presented in Table 4. Calculating the SD around the time that the mixer is switched off indicates the minimum SD ratio criterion is satisfied over electrode no. 2. Even though analogous patterns are spotted in other electrodes—including the total averaged value (Fig. 68 a) – the evaluated mixer SD ratio is consistent on the selected electrode throughout different experimental repetitions.

Dissemination Level: **Public**

This project has received funding from the European Union's Horizon 2020 research and innovation programme under the Marie Skłodowska-Curie Grant Agreement No. 764902.

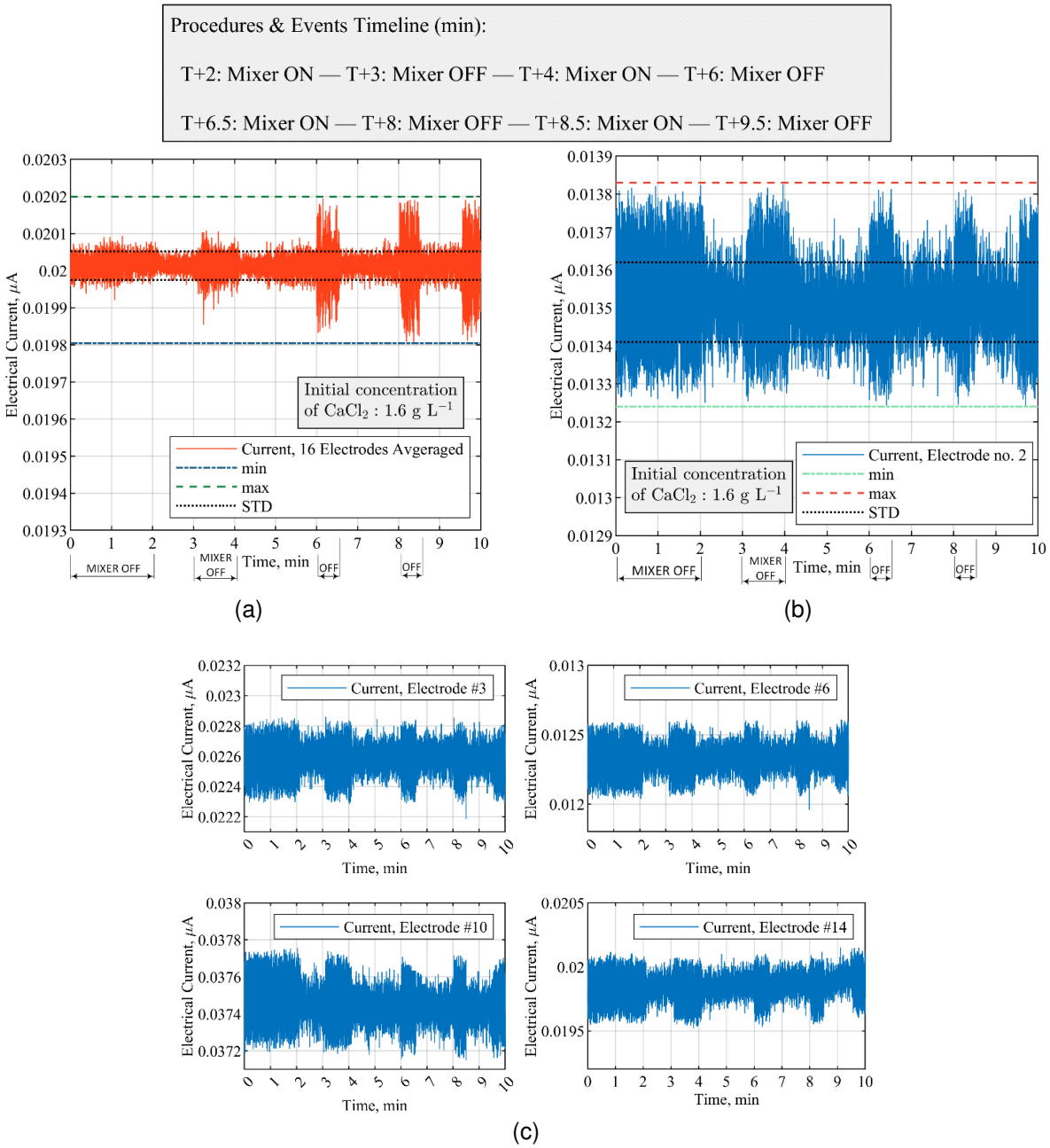

Fig. 68: Changes in electrical current measurement induced by switching on/off the stirrer at $CaCl_2$ concentration of 1.6 g L^{-1}, without any reagent addition. (a) Electrical current measurements by averaging 16 electrodes, (b) Mixer-induced variation in the signals acquired through electrode no. 2, (c) Comparison of electrical current measurements via a single-electrode located at 90° apart inside the stirred tank reactor. Quantitative information from all the electrodes is reported in Table 4.

This project has received funding from the European Union's Horizon 2020 research and innovation programme under the Marie Skłodowska-Curie Grant Agreement No. 764902.

Table 4: Standard deviation ratio analysis of all the electrodes of the ERT system. SD ratio (σ_r) are evaluated according to Eq. 8 and are reported around the time that the mixer switches off. $CaCl_2$ concentration is 1.6 $g\,L^{-1}$, without the feed solution addition. The mixer switches on at 100 RPM. Illustrations for selected electrodes are displayed in Fig. 68.

Electrode Index	3 – 3.5 min, (mixer off)	5.5 – 6 min	6 – 6.5 min, (mixer off)	7.5 – 8 min	8 – 8.5 min, (mixer off)
	σ_r	σ_r	σ_r	σ_r	σ_r
1	1.86	0.71	1.53	0.59	1.62
2	2.14	0.55	2.30	0.42	2.12
3	1.40	0.69	1.44	0.68	1.86
4	1.57	0.57	1.60	0.67	1.36
5	1.28	0.97	1.40	0.48	2.01
6	1.84	0.59	1.45	0.65	1.48
7	1.51	0.57	1.04	1.99	1.00
8	1.80	0.55	1.59	0.89	1.08
9	0.56	2.26	1.61	0.75	1.32
10	1.62	0.52	1.58	0.68	1.87
11	1.39	0.64	1.25	0.67	1.86
12	1.66	0.66	1.56	0.61	1.73
13	1.55	0.79	1.61	0.64	1.56
14	1.13	0.84	1.43	0.55	1.56
15	1.52	0.73	1.54	0.73	1.45
16	1.60	0.61	1.79	0.54	1.58

Fig. 69 shows tomographic images at critical times during the reactive crystallization process. Reconstructions are done by the single-step Gauss-Newton technique. The offline reconstructions do not meaningfully characterize the physico-chemical phenomena of the fast-kinetic crystallization process and no significant visual changes can be detected. In the current investigation, the ERT reconstructions could not be utilized due to non-deterministic and insensitive data from the crystal suspensions. Moreover, the relatively slow reconstruction time and the global resolution impairs the required performance for real-time monitoring. In summary, more comprehensive research efforts are needed for image reconstructions studies and their correlation to the experimental phenomena. While employing a single electrode to analyze the ERT measurements provides partial knowledge of the suspension and the precipitation process, it demonstrates a promising tool to investigate faults and malfunction throughout the crystallization process. In the present study, the measurement of the electrical current from electrode no. 2 is used to develop the FDD methodology. The selected electrode is located close to the feed point, has a relatively higher sensitivity and favorable signal-to-noise ratio.

Dissemination Level: **Public**

This project has received funding from the European Union's Horizon 2020 research and innovation programme under the Marie Skłodowska-Curie Grant Agreement No. 764902.

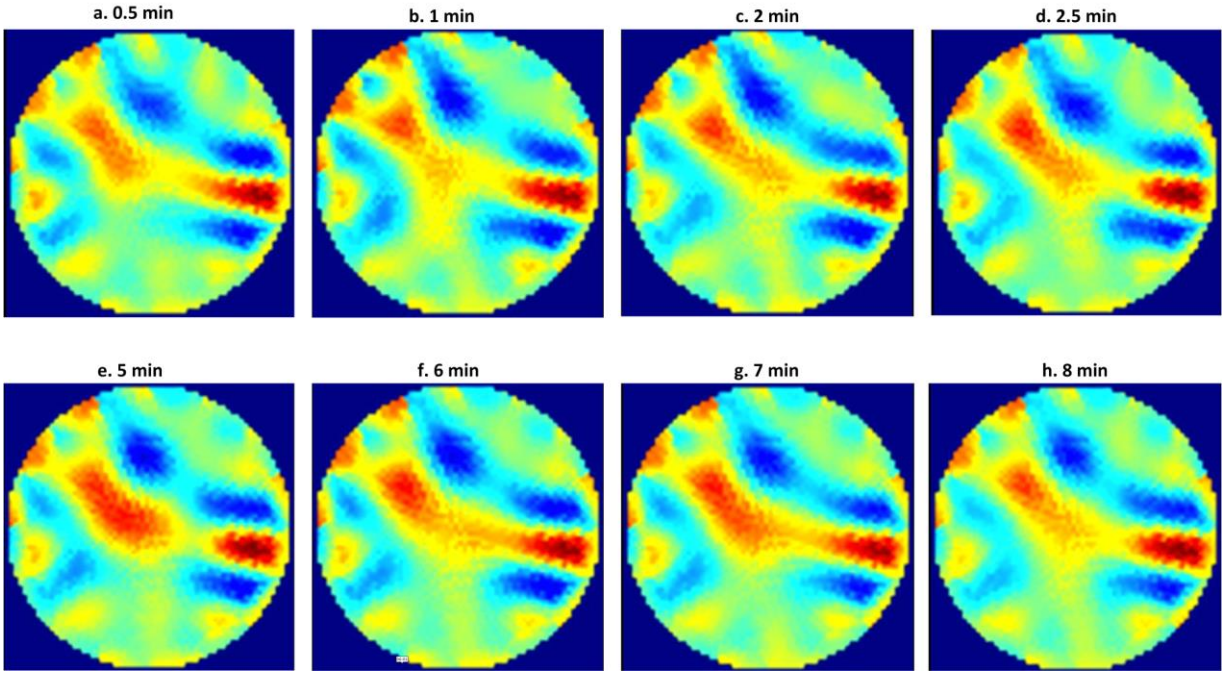

Fig. 69: ERT-based tomographic reconstruction of the $CaCO_3$ crystallization process. The following consecutive actions are applied during the ERT measurements: Switching on the mixer at T+2 min, switching on the pump at T+5 min (start of the crystallization), switching off the feed pump at T+7 min (no reagent addition), switching on the pump at T+8 min. The initial $CaCl_2$ concentration is 1.6 $\frac{g}{L}$, mixing speed is 100 RPM, and the feed addition rate is 40 $ml\ min^{-1}$. A detailed single-sensor analysis of the experiment is provided in Fig. 74, Fig. 75, and Table 8.

4.6.2. Measurements of $CaCO_3$ solid particles addition by ERT electrodes

To investigate the dynamical effects of solid calcium carbonate on the electrical field of the ERT system, two different amounts of solid particles are added into the reactor containing 3 L water. Solid samples of commercial calcite (provided by VWR, purity > 99%) are used for the measurement. Particles are added from the top of the reactor by hand.
Fig. 70 (a) and 70 (b) show the experimental measurement and procedures for the solid concentrations of 8.3 $g\ L^{-1}$ and 33.3 $g\ L^{-1}$. The solid particle addition occurs after 5 minutes (i.e. T+5 min) into the measurement when the mixer is switched off. No significant changes in the electrical current of the medium are observed before and after the addition of the non-conductive calcium carbonate. The electrical current of the solution slightly increases from an average value of $2.7 \pm 0.3 \times 10^{-3}$ µA to $3.3 \pm 0.2 \times 10^{-3}$ µA after switching on the mixer at T+6 min. The relative increase in the current is primarily due to the distribution of solids and distinct electrical properties of the suspension. Moreover, since the background medium is non-conductive in comparison to the $Ca^{2+}_{(aq)}$ solutions, the status of the mixer (e.g. on/off) is not substantially affecting the electrical field.

Dissemination Level: **Public**

This project has received funding from the European Union's Horizon 2020 research and innovation programme under the Marie Skłodowska-Curie Grant Agreement No. 764902.

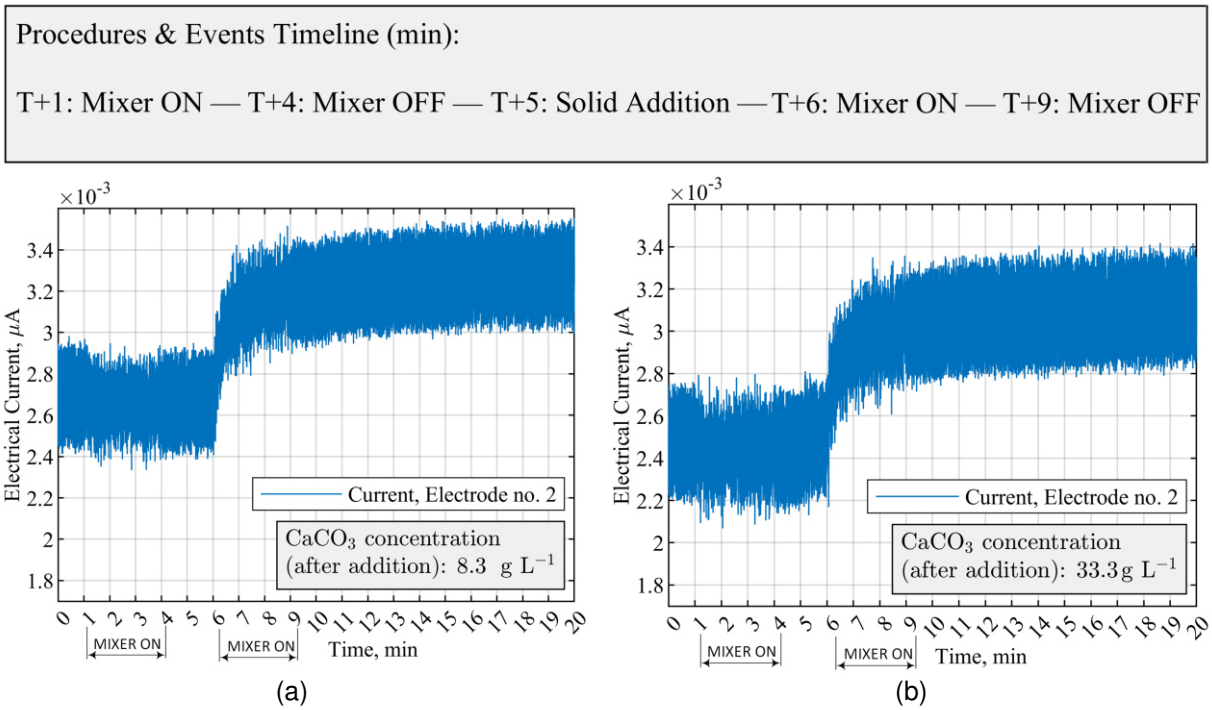

Fig. 70: Variation in the electrical current of $CaCO_3$ suspensions based on single-electrode measurements; (a) $CaCO_3$: 8.3 g L^{-1}, (b) $CaCO_3$: 33.3 g L^{-1}.

4.6.3. ERT-based malfunction identification

Fault tree analysis development

The fault tree analysis methodology is used to develop the system failure states irrespective of their severity. The FTA is a graphical logic representation of combinations of failures or events that may occur to a functional system and shows a map of failure paths. Depending upon the criticality of the process, each branch can be developed further.
Fig. 71 shows the FTA of the integrated crystallization–CO_2 capture system of the present study. The process under investigation consists of several important physical and chemical components such as feeding pump, stirrer, reagent solution, CO_2 gas absorbent solution concentration, and the amount of calcium chloride in the receiving reactor. Because there is a relatively large theoretical combination of such faults, the investigated cases represent the ones with practical interest to the entire process.

Dissemination Level: **Public**

This project has received funding from the European Union's Horizon 2020 research and innovation programme under the Marie Skłodowska-Curie Grant Agreement No. 764902.

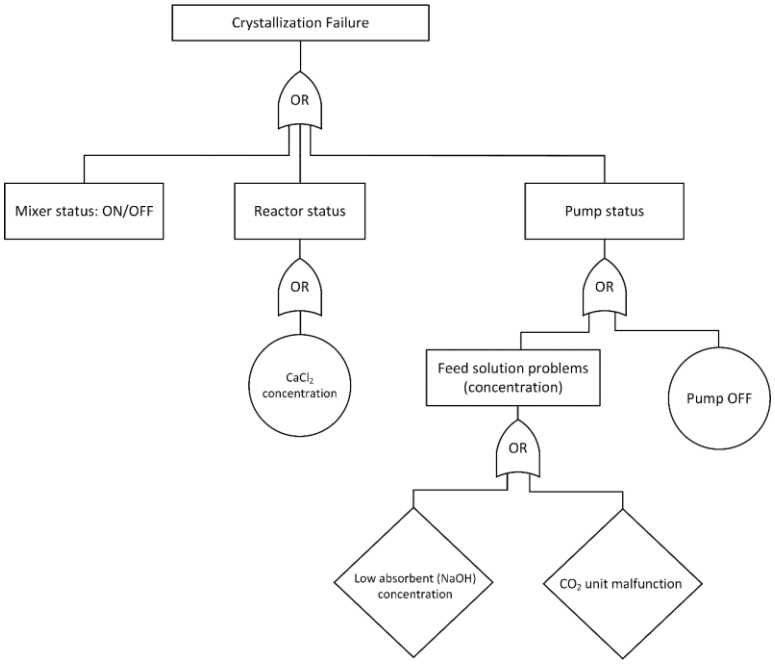

Fig. 71: Fault tree analysis diagram for the integrated CO_2 capture and reactive crystallization process of calcium carbonate.

Total ion balance modeling and the minimum runtime

The presence of different ionic compounds (see Eq. 7) during the calcium carbonate crystallization process results in the variation of the electrical current flow in the opaque solution. To enhance the accuracy of the process automation in terminating the crystallization (i.e. switching off the mixer and feed pump), a minimum runtime criterion is defined. The theoretical minimum runtime is determined by the total ion balance modeling of the entire process – that is the minimum amount the feed solution requires to consume a known calcium chloride concentration in the receiving tank. A final command to terminate the crystallization process is applied when both the experimentally measured slope factor criterion is satisfied, and the minimum run time has elapsed.
The data presented in Table 5 is used to perform the theoretical ion balance modeling over time for the investigated chemical reaction. The pumping capacity of the impeller, Q, can be used to quantify the flow pattern in the stirred tank reactor. As expressed in Eq. 11, Q is the volumetric flow rate passing through the mixing planes due to the rotation of the impeller [15].

$$\mathrm{Q} = \mathrm{N_q N D^3} \tag{11}$$

where $\mathrm{N_q}$ is the pumping number of the Rushton impeller [15], N is the stirring rate (rps), and D is the impeller diameter.

Table 5: Main operating parameters for the theoretical ion balance modeling and precipitation experiments

Parameter	Unit	Value
$CaCl_2$ concentrations	$\mathrm{g\ L^{-1}}$	0, 1.6, 3.3 and 6.6
NaOH concentration at the	$\mathrm{mol\ L^{-1}}$	12.1 ± 0.05

Dissemination Level: **Public**

This project has received funding from the European Union's Horizon 2020 research and innovation programme under the Marie Skłodowska-Curie Grant Agreement No. 764902.

feed		
$CO_{3(aq)}^{2-}$ concentration at the feed	$\mathrm{mol\ L^{-1}}$	0.14 ± 0.2
Impeller pumping capacity	$\mathrm{m^3\ s^{-1}}$	0.004
Impeller pumping number	–	0.70
Impeller diameter	m	0.07
Stirring rate	rps	1.67
Impeller tip speed	$\mathrm{m\ s^{-1}}$	0.37

As presented in Fig. 72, four different initial concentrations of calcium chloride are employed to conduct the calculations. When the initial concentration of $Ca_{(aq)}^{2+}$ in the receiving reactor is 0 $\mathrm{g\ L^{-1}}$, the addition of the ionic feed solution results in an immediate rise in the total ions in the crystallizer without the formation of any solid particles. Crystallization occurs when the initial concentration of $Ca_{(aq)}^{2+}$ is non-zero, which is an indication of a decrease in the super-saturation and formation of non-conductive solid particles. Depletion of the initial $Ca_{(aq)}^{2+}$ in the reactor results in a continuous descending trend for the global electrical current distribution of the solution.

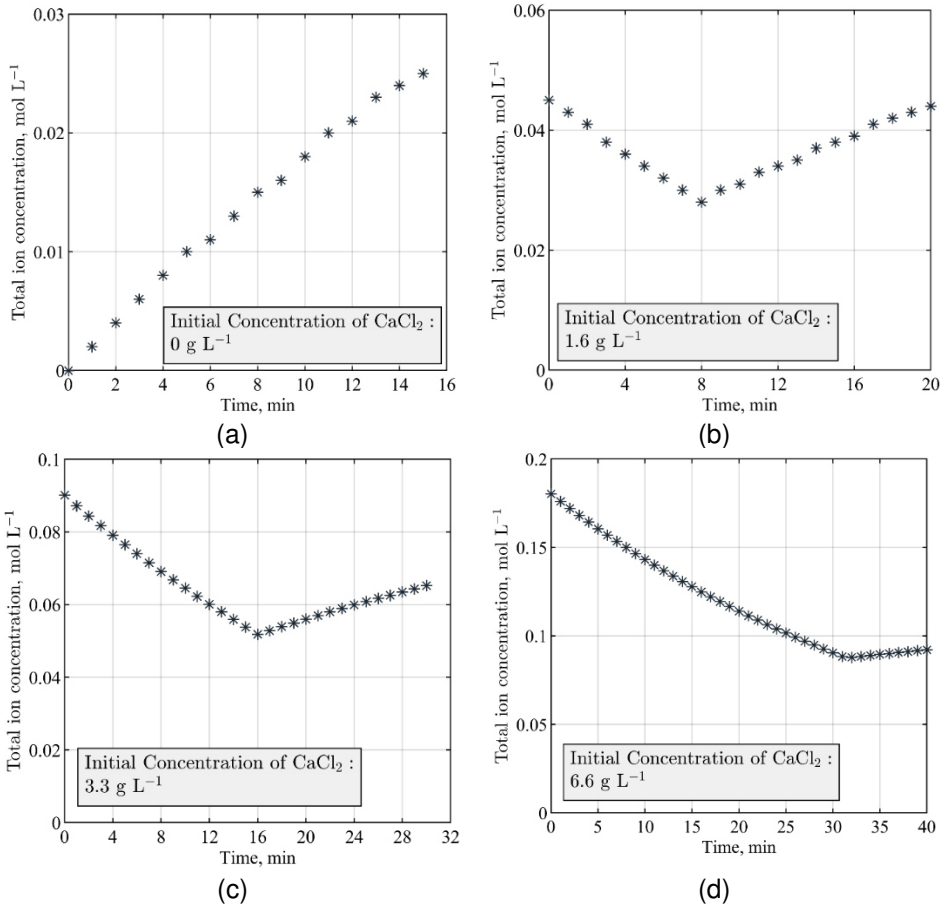

Fig. 72: Theoretical modeling and calculation of the total ion balance during the crystallization process. Constant parameters are feed solution pH: 12.1, CO_3^{2-} concentration: 0.14 $\mathrm{mol\ L^{-1}}$, feed addition

This project has received funding from the European Union's Horizon 2020 research and innovation programme under the Marie Skłodowska-Curie Grant Agreement No. 764902.

rate: $40\ \mathrm{ml\ min^{-1}}$. The initial solution volume in the reactor is 3 L. (a) No precipitation; (b) Precipitation until 8 minutes, afterwards calcium chloride is depleted; (c) Precipitation until 16 minutes, afterwards no calcium chloride is present; (d) Precipitation until 31 minutes, afterwards no calcium chloride is remaining.

Fault detection and malfunction scenarios

Different scenarios of the ERT-based malfunction investigation are listed in Table 6. Existing patterns in the signals measured by a single electrode of the ERT system are analyzed to determine the mechanical equipment condition throughout each batch operation.

Table 6: The investigated scenarios for fault detection and diagnostics with electrode no. 2 of the ERT system. All the experiments are carried out at a mixing speed of 100 RPM and a feed addition rate of $40\ \mathrm{ml\ min^{-1}}$.

Experiment index	Constantly operational	Malfunction(s) during the process
Case no. 1	Pump ON	Mixer ON & OFF
Case no. 2	Mixer ON	Pump ON & OFF
Case no. 3	Pump ON & Mixer ON	Feed is water (not carbonate ions)

In all the cases, the initial concentration of calcium chloride is 1.6 $\mathrm{g\ L^{-1}}$. The main operating parameters of the experiments are tabulated in Table 5. The end-to-end experimental procedure for each operating condition is repeated three times to ensure the validity and repeatability of the results. As presented in the total ion balance modeling of the process, the addition of the ionic reagent solution to the reactor leads to the precipitation of $\mathrm{CaCO_3}$ and the subsequent depletion of $\mathrm{CaCl_2}$. The formation of the non-conductive solid calcium carbonate is monitored in real-time by the ERT system and measured through electrode no. 2, which is located adjacent to the feeding point.

Fig. 73 displays a situation where operator-induced mixer malfunctions are enforced while the process is ongoing; mixer malfunctions of a duration of 30 seconds are applied at times T+7 min and T+10 min into the process. Switching off the stirrer results in a rapid variation of the electrical current and increases the mean standard deviation, which in turn notifies the operator via an alert system implemented in the process automation program. Currently, the return to the nominal operating mode following the fault is done by the operator; however, there is a possibility of full automation by further development of the experimental setup and the software.

Furthermore, as shown in Fig. 73, the slope of the measured electrical current has a descending trend because of the continuous reagent addition and formation of solids. The decreasing slope of the fitted linear line between 5–12 min, which equals to approximately $-2.12 \times 10^{-4}\ \mathrm{\mu A\ min^{-1}}$, indicates the consumption of $\mathrm{CaCl_2}$. After 13 minutes into the process, the value of the slope decreases ($-5.68 \times 10^{-6}\ \mathrm{\mu A\ min^{-1}}$) to a roughly plateau region. For the employed concentrations of species, both an abrupt change in the slope factor after 13 minutes and fulfilling the minimum experimental runtime, results in an automatic shutdown of the mixer and the feed pump. Quantitative data of the mean value of the slope between 5–12 min from different electrodes are presented in Table 7. The data addresses the reliability

Dissemination Level: **Public**

This project has received funding from the European Union's Horizon 2020 research and innovation programme under the Marie Skłodowska-Curie Grant Agreement No. 764902.

of the selected electrode in triggering the alert system concerning the stirrer malfunctions; in comparison to other electrodes, the steep of the slope in electrode no. 2 is greater.

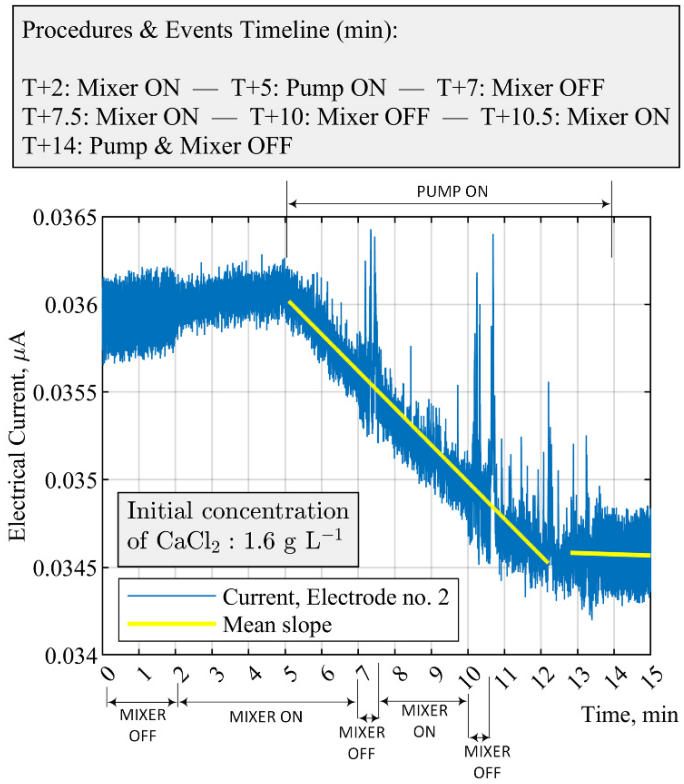

Fig. 73: Fault detection and malfunction scenarios for case no. 1 in Table 6. The feed pump is constantly switched on and the mixer switches on (100 RPM) and off (0 RPM) while the precipitation is ongoing. The entire experimental process automatically shuts down when $CaCl_2$ is depleted at approximately T+13 min. The constant feed flow rate is 40 $ml\ min^{-1}$.

Table 6: Assessment of the slope of the electrical current between 5–12 minutes from all the electrodes of the ERT system. The data describes the malfunction scenarios for case no. 1 in Table 6 and the associated Fig. 73.

The slope of the electrical current from all the electrodes of the ERT system between the time 5–12 minutes																
Electrode	1	2	3	4	5	6	7	8	9	10	11	12	13	14	15	16
Current ($\mu A\ min^{-1}$), × (-1×10^{-4})	1.93	2.12	1.04	0.47	0.96	0.14	0.18	0.26	0.19	0.14	0.03	0.11	0.21	0.79	1.51	1.54

Fig. 74 demonstrates the intermittent operation of the feed pump and its effect on the electrical current measurement of the ERT system (electrode no. 2). The mean value of the electrical current from T+5 min to T+7 min has a steeper slope angle in comparison to the period in which the pump is switched off (between 7–8 min). A rapid decrease of 20-25 times in the average slope factor of the electrical current towards a plateau, automatically triggers the

Dissemination Level: **Public**

This project has received funding from the European Union's Horizon 2020 research and innovation programme under the Marie Skłodowska-Curie Grant Agreement No. 764902.

alarm that indicates a malfunction in the pump – a time difference of 30 seconds is used to evaluate the moving average of the incoming electrical signals for the pump status. Since the precipitation and the real-time fault detection is dynamic and fast, the accuracy and efficiency of the decision-making of the process automation are promising enough to realize the overall trend of the experimental system.

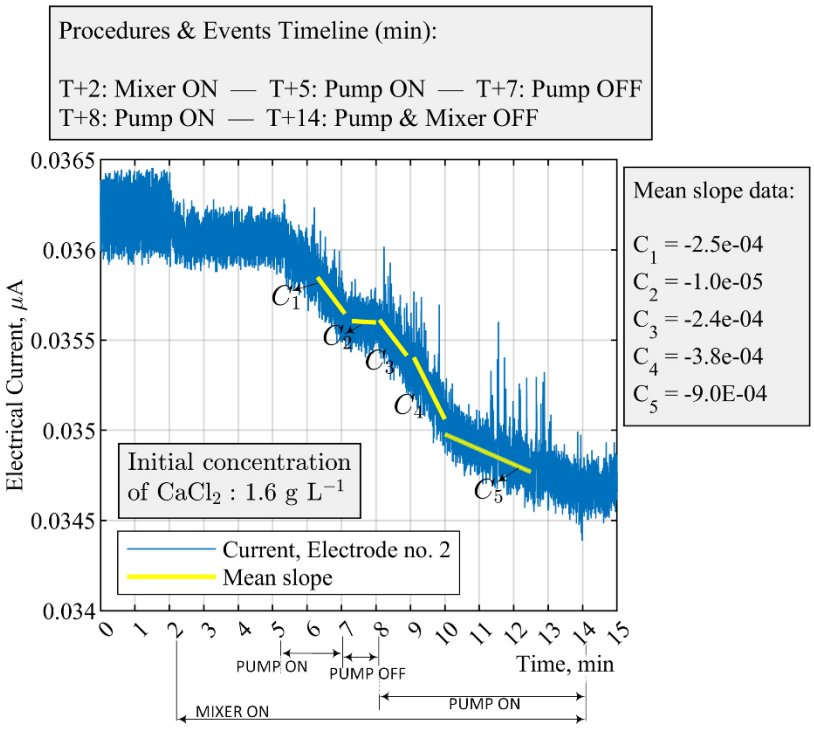

Fig. 74: Fault detection and malfunction situation for case no. 2 in Table 6. The stirrer is continuously on (100 RPM) and a malfunction is enforced on the pump at T+7 min. Precipitation is ongoing only when the feed pump is on. The feed flow rate is 40 $\mathrm{ml\ min^{-1}}$.

To ensure a satisfactory single-sensor operation during the precipitation process, the performance and sensitivity of different electrodes of the ERT system to pump failure are analyzed. As displayed in Fig. 75, measurements obtained from 4 equidistance electrodes, positioned at 90° apart inside the reactor – namely, sensors no. 3, 6, 10, and 14 – can be qualitatively compared with the data from electrode no. 2. In terms of the lower stochastic behavior of the acquired signals in different operating conditions, measurements obtained through sensor no. 2 are, in comparison, robust enough for a malfunction identification for the pump.
In addition, Table 8 presents the slope factor evaluation for all the electrodes of the ERT system at critical times during the process. The implemented methodology based on electrode no. 2. reacted well to significant variations in the slope factor, which is an indication of the pump malfunction.

Dissemination Level: **Public**

This project has received funding from the European Union's Horizon 2020 research and innovation programme under the Marie Skłodowska-Curie Grant Agreement No. 764902.

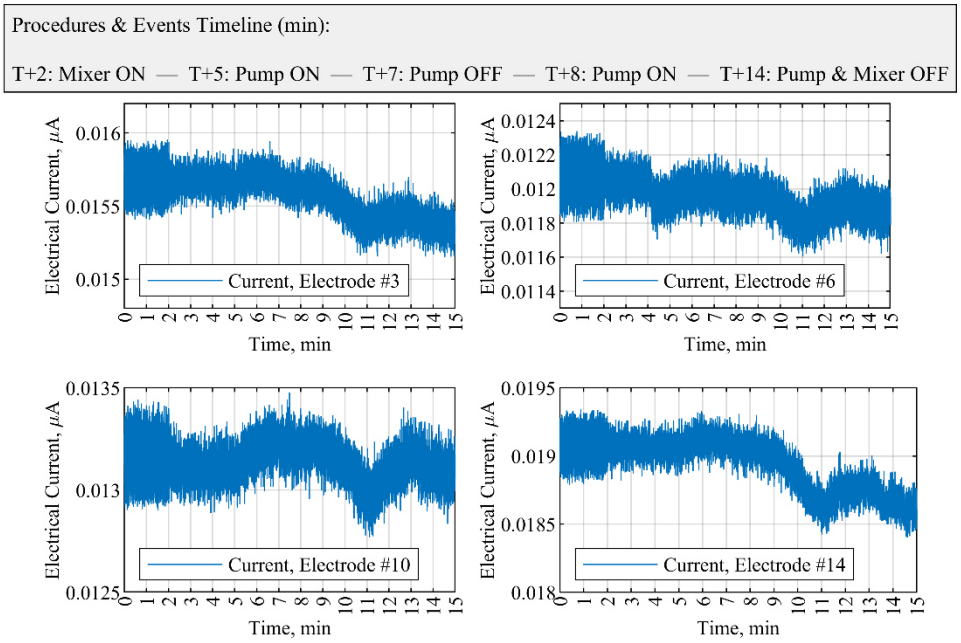

Fig. 75: Performance of different sensors during feed pump failure situations (case no. 2 in Table 6). Sensors are separated at 90° apart inside the crystallizer. The initial $CaCl_2$ concentration is 1.6 $g\,L^{-1}$. The feed flow rate is 40 $ml\ min^{-1}$ and the mixing speed is 100 RPM.

Table 8: Comparison of the slope of electrical current over all the electrodes of the ERT system. The slope factor, K, is calculated at the time that the pump is switched off, which triggers an alert based on electrode no. 2. The data illustrates the malfunction scenarios for case no. 2 in Table 6 and Fig. 74 and 75.

Electrode index	$\mathbf{t_1}$ = 6.3 – 7.1 min, (Pump on)	$\mathbf{t_2}$ = 7.2 – 8 min, (Pump off)	Slope factor, K	$\mathbf{t_3}$ = 8.1 – 8.9 min, (Pump on)
	C_{t_1} $(\times \mathbf{10^{-5}})$	C_{t_2} $(\times \mathbf{10^{-5}})$	$\mathbf{K} = C_{t_1}/C_{t_2}$	C_{t_3} $(\times \mathbf{10^{-5}})$
1	-23.38	-3.16	7.39	-22.98
2	-25.35	-1.01	25.09	-24.87
3	-11.00	-4.71	2.33	-3.15
4	-6.19	-2.98	2.07	-9.55
5	19.12	-10.14	-1.88	-5.62
6	-0.50	-4.04	0.12	0.50
7	1.43	-3.4	-0.42	0.659
8	1.38	-5.46	-0.25	-1.06
9	2.35	-4.6	-0.51	-1.61
10	1.40	-3.10	-0.45	-2.20
11	3.08	-2.10	-1.4	0.78
12	1.86	-2.76	-0.67	-0.48
13	0.16	-1.57	-0.03	-0.18
14	-2.50	-5.00	0.5	-5.61
15	-14.04	-4.58	3.06	-13.39
16	-19.9	-2.36	8.43	-21.29

Dissemination Level: **Public**

This project has received funding from the European Union's Horizon 2020 research and innovation programme under the Marie Skłodowska-Curie Grant Agreement No. 764902.

According to the FTA analysis, the content of the feed solution can lead to a reactive crystallization failure. Issues in the feed solution could be due to prior faults in the system; for instance, an inefficient CO_2 capture process leads to lower concentrations of the $CO_{3(aq)}^{2-}$ in the feed. Fig. 76 presents an operating condition where the feed concentration is not at the nominal level of 0.14 ± 0.2 $\mathrm{mol\,L^{-1}}$ of $CO_{3(aq)}^{2-}$ and instead, water is used to conduct the experiments. The addition of the non-ionic solution to the crystallizer containing 1.6 $\mathrm{g\,L^{-1}}$ of $CaCl_2$ results in a continuous decrease in the overall electrical current of the medium, as measured by electrode no. 2. The expected precipitation time after the start of the feed pump is 8 minutes; since no calcium chloride is consumed throughout the 8-minute window, the decrease in the overall electrical current is due to an increase in the solution volume and not the precipitation process.

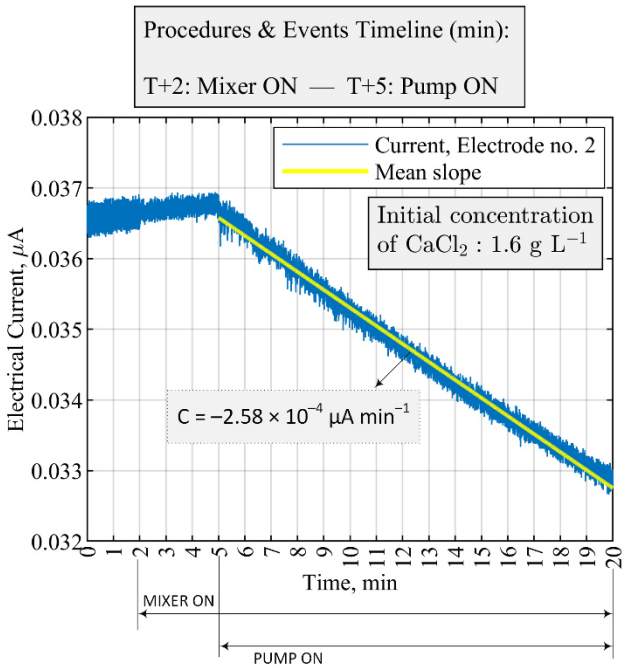

Fig. 76: Fault detection and malfunction scenario by a single sensor of the ERT system corresponding to case no. 3 in Table 6. A normal operation for the mixer (100 RPM) and pump ($40\ \mathrm{ml\ min^{-1}}$) but the feed solution that flows into the crystallizer contains 0 $\mathrm{g\,L^{-1}}$ $CO_{3(aq)}^{2-}$.

4.6.4. Ultrasound tomography: Application of USCT to detect particle beads

To establish the dynamical imaging based on particle concentration, circular particle beads of 4 mm in diameter are poured into the stirred tank reactor. The idea of the proposed experiment is to investigate the real-time changes in the dynamical states of the stirred tank reactor using USCT. A description of the experimental procedures is presented in Table 9.

Table 9: Particle beads detection experimental procedure

Steps	Tasks

This project has received funding from the European Union's Horizon 2020 research and innovation programme under the Marie Skłodowska-Curie Grant Agreement No. 764902.

1	T+0 min: Charge 3 L of water
2	T+0 min: Start measurements
3	T+1 min: Slowly add the tracer balls (100 g) during 1st minute
4	T+2 min: Start mixer (200 RPM) at 2 minutes
5	T+3 min: Stop mixer at 3 minutes
6	T+4 min: End of measurements at 4 minutes

Fig. 77 shows experimental photos and tomographic reconstruction, with respect to time during the experiment with 100 g particle beads. The addition of particles to the reactor filled with 3 L water and the effect of mixing are monitored. Fig. 77 (a), 17 (b) and 17 (c) present three distinguished states of the experiments during the first 2 minutes, namely, the beginning of particle addition, the mid-point, and the end of particle feeding, respectively. Particles' sedimentation is clear in the presented experimental photographs.
The 2D reconstructions show the gradually increasing values of the injection point as the particles are poured into the tank. The acoustic field inhomogeneities are introduced both due to the existence of particles within the sensors' field-of-view (FOV) and the disturbances that occurred due to pouring. Fig. 77 (e) presents the reconstructed volume of the region with relatively higher intensities of injection – the isosurface method was used for the reconstruction and the region-growth is depicted clearly. Fig. 77 (f) displays the tank's state immediately after the pouring and provides insights into the particles' settling over time.

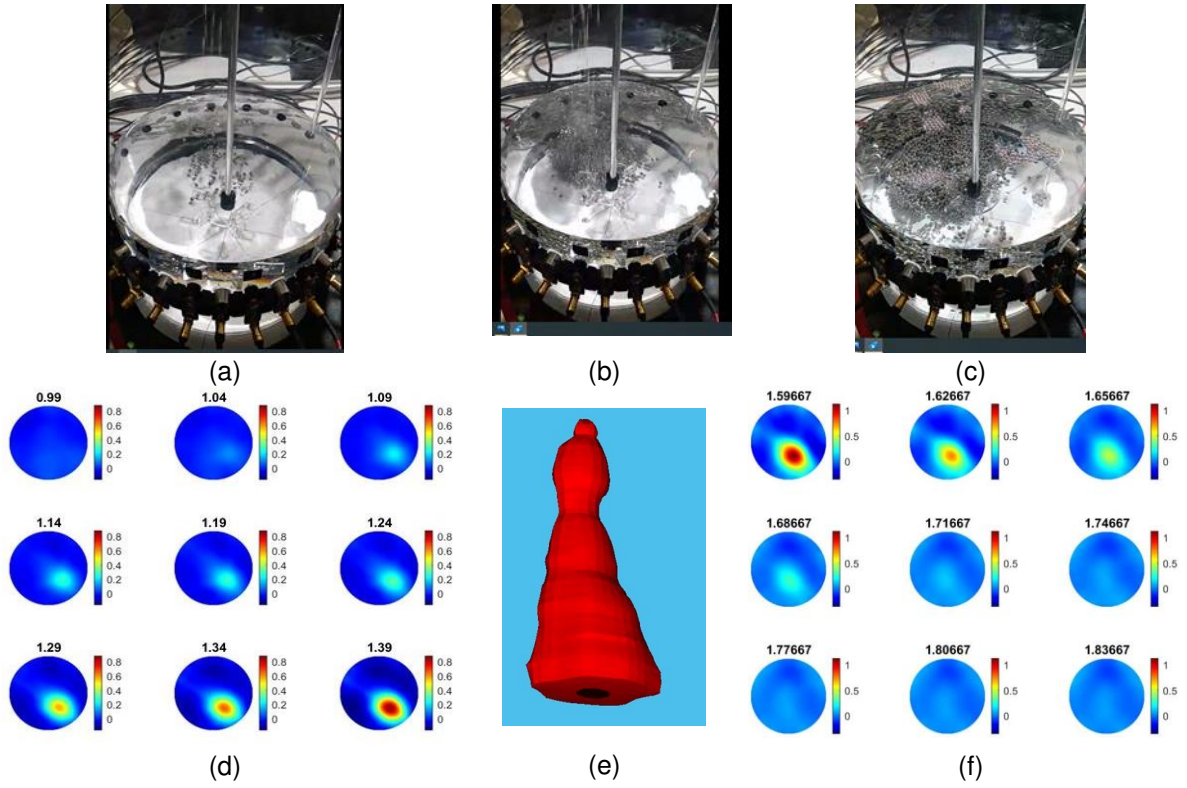

Fig. 77: (a), (b), (c) Photos from particle beads experiments demonstrating feeding and mixing (200 RPM) during the experiment. (d) Reconstructions between 0.99 min and 1.39 min. (e) Volumetric dis-

This project has received funding from the European Union's Horizon 2020 research and innovation programme under the Marie Skłodowska-Curie Grant Agreement No. 764902.

tribution of particle beads in the period of the start of feeding balls. (f) Reconstructions between 1.6 min and 1.84 min, balls feeding will gradually stop. Weight of particles: 100 g, water volume: 3 L.

As presented in Table 9, mixing at 200 RPM is switched on at approximately T+2 min. Thus, the whole solution turns into a dispersed liquid-solid state as addressed by the experimental photo in Fig. 78 (a). Tomographic reconstruction addresses the mixing-induced inhomogeneities by compromising the higher intensity values across the entire region-of-interest (ROI), as shown in Fig. 78 (c). According to Fig. 78 (b), the particles tend to gather in the tank's central area (where the stirring takes place) as long the mixing continues. Reconstructions in Fig. 78 (d) agree to that, as, after a while from the mixing starting point, higher inhomogeneities start gathering at the center of the tank. This effect may be caused by the centripetal force introduced by the stirrer and thus a tendency of particles to gather close to the tank bottom is recognized.

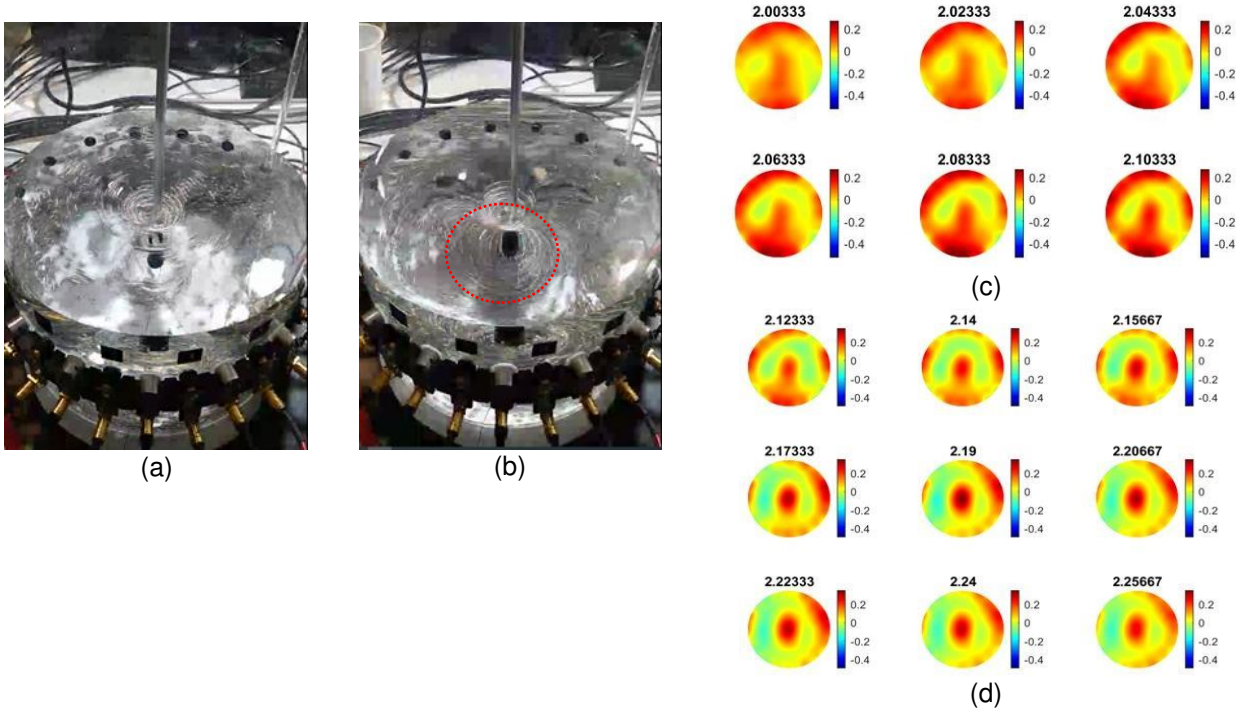

Fig. 78: (a), (b) Images from particle beads experiments demonstrating feeding and mixing (200 RPM) during the experiment. (c), (d) Images between 2:00 min and 2:56 min, showing the process of mixing. Amount of particles: 100 g, water volume: 3 L.

The exact experimental procedures as discussed above were conducted two more times, each time adding 100 g of additional particle beads to 3 L water and recording the measurements. Fig. 79 shows the dynamical analysis of the experiment using the mean value of the 256 measurements.

This project has received funding from the European Union's Horizon 2020 research and innovation programme under the Marie Skłodowska-Curie Grant Agreement No. 764902.

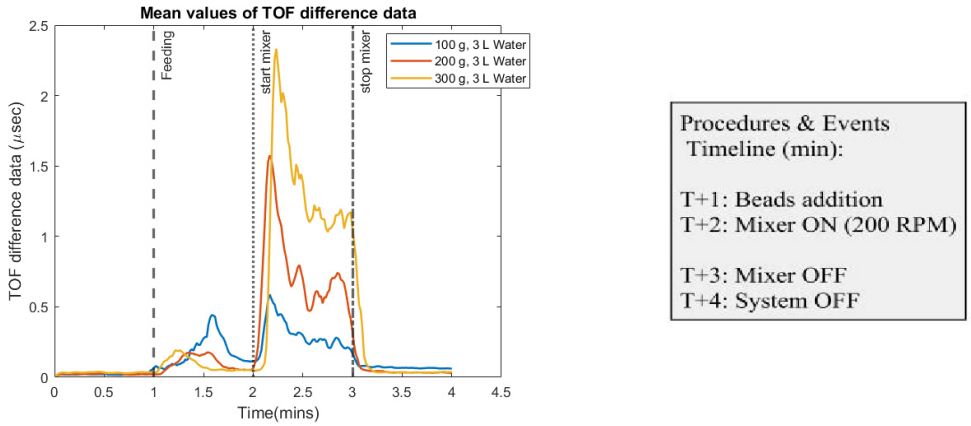

Fig. 79: Mean values of the time-of-flight delay for the three experiments with different beads concentrations

4.6.5. Characterizing $CaCO_3$ solid particles distribution by USCT

Four different concentrations of solid calcium carbonate suspensions are used to investigate the sound propagation. Samples of commercial calcite (provided by VWR, purity > 99 %) are added by hand from the top of the reactor containing 3 L water. Fig. 80 (a) presents the experimental procedure in sequence and Fig. 80 (b) and 80 (c) display the topology-based visualization by the ultrasound system, which provides satisfactory information from the opaque suspensions. The tomographic images are obtained for the concentration of 25 $\mathrm{g\,L^{-1}}$ at several key events and show the particle addition and the effect of mixing that leads the medium to a homogeneous state.

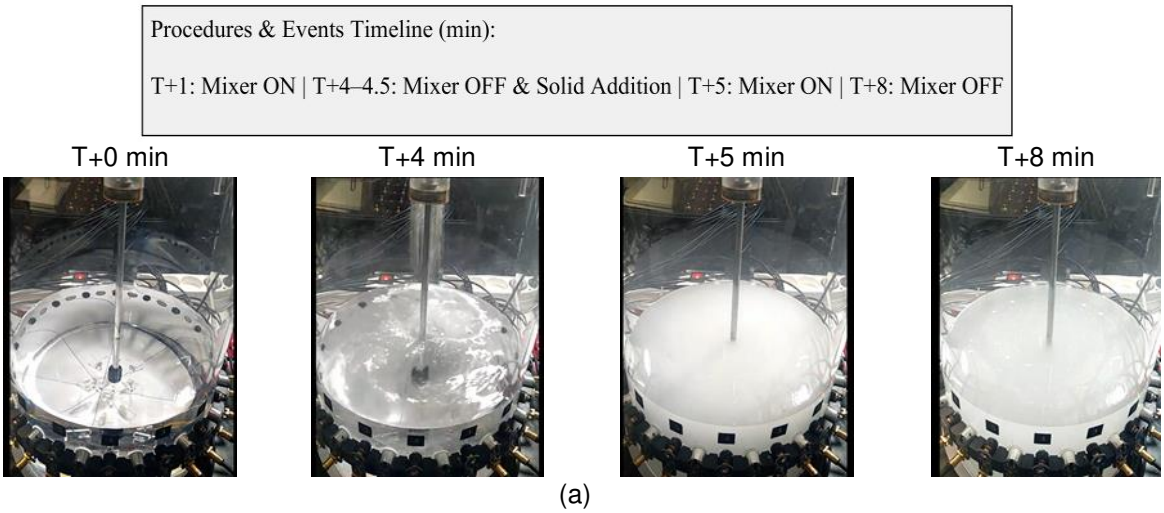

(a)

This project has received funding from the European Union's Horizon 2020 research and innovation programme under the Marie Skłodowska-Curie Grant Agreement No. 764902.

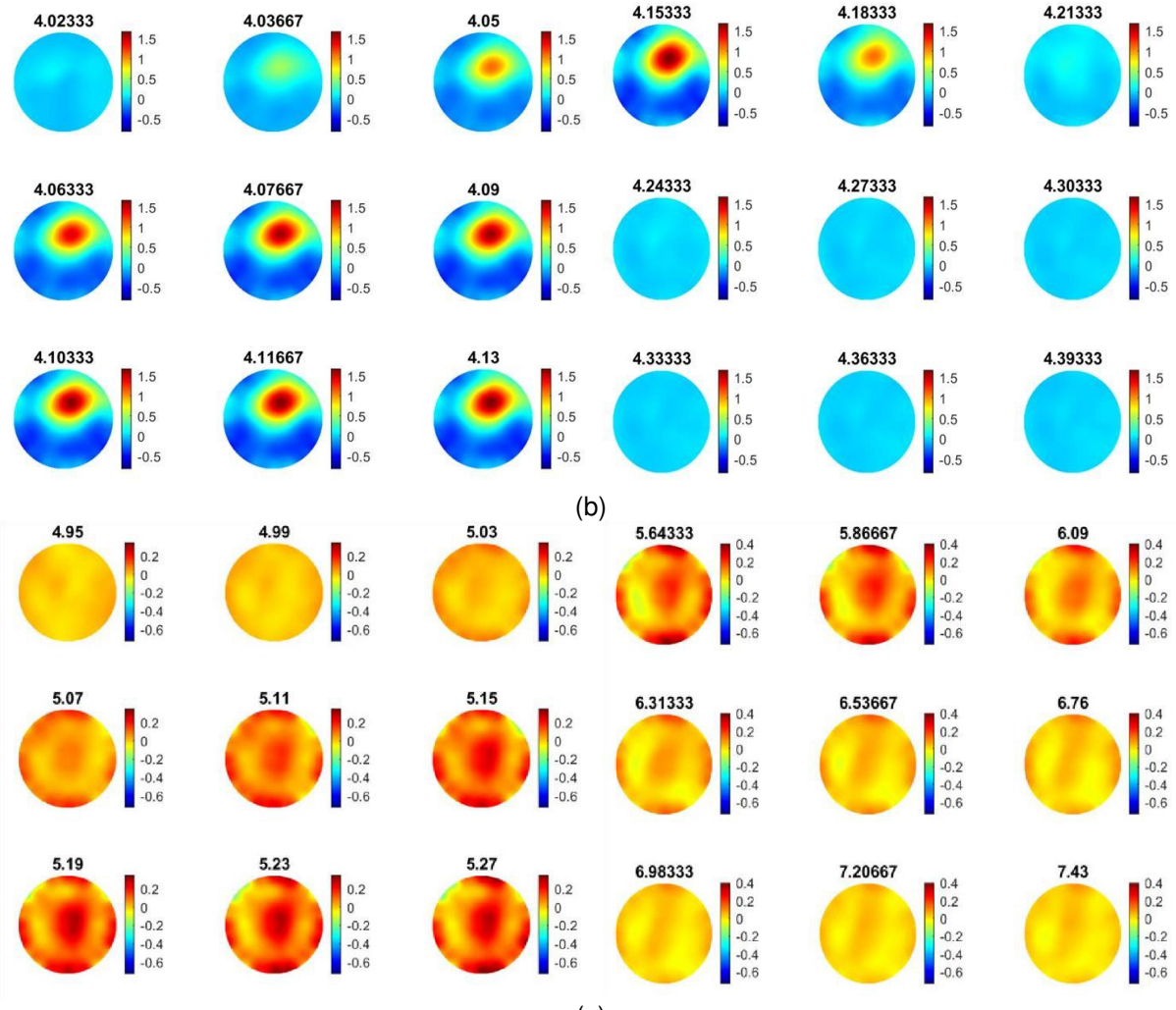

Fig. 80: Images on shown time step images of feeding. (b) Reconstruction between time 4.02 min to 4.39 min, describing feeding. (c) Reconstruction between time 4.95 min to 7.43 min during the mixing process.

As presented in Fig. 81, at relatively higher concentrations of solid calcium carbonate in the reactor, sound speed propagation decreases, thus resulting in higher TOF delays. The highest peak at the T+4 min in the USCT measurement is due to an abrupt change and disturbance in the reactor because of pouring the $CaCO_3$ particles. Switching on the mixer at T+6 min distributes the micron-sized particles in the suspension and causes a rapid increase in the TOF. The maximum peak after switching on the mixer is correlated to the overall concentration of the suspension. The TOF has a descending trend after reaching the maximum peak (approximately from T+5.5 min afterwards), which characterizes a relatively homogenous medium that facilitates sound propagation.

This project has received funding from the European Union's Horizon 2020 research and innovation programme under the Marie Skłodowska-Curie Grant Agreement No. 764902.

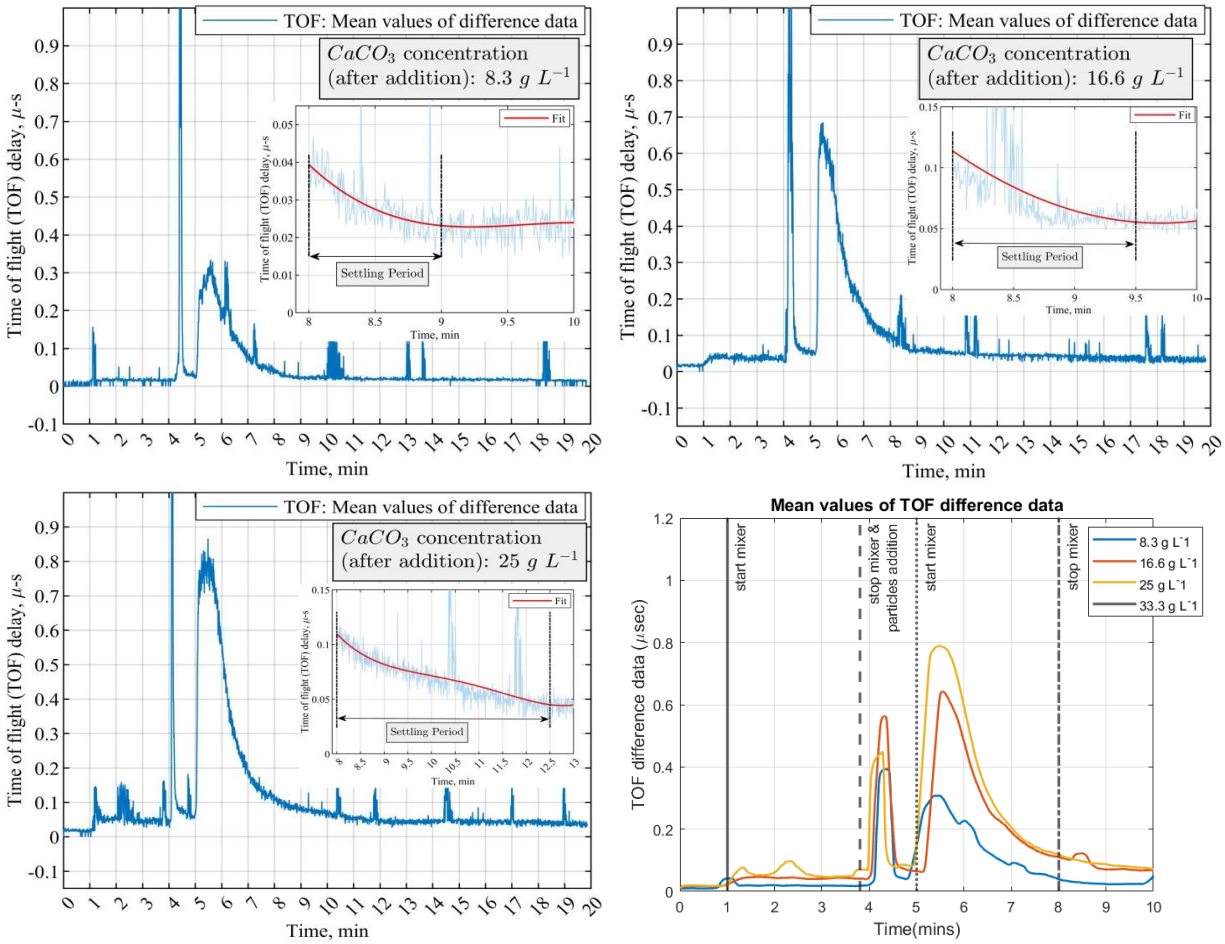

Fig. 81: Mean values of the time-of-flight difference data in four concentrations of $CaCO_3$ suspensions. Experimental procedures are the same for all the concentrations. The initial volume of water is 3 L. The settling period is defined to calculate the settling velocity of particles (see Table 10).

4.6.6. Quantification of particle settling time by USCT measurement

The settling velocity of particles is a function of the free settling velocity (terminal velocity): It decreases as solid particle concentration increases in the fluid domain. The free settling velocity of particles for the Stokes' regime, V_t, is determined based on the following expression:

$$V_t = \frac{g d_p^2 (\rho_\sigma - \rho_f)}{18\mu} \tag{12}$$

where ρ_f and ρ_s are fluid and solid density, respectively, d_p represents particle diameter, g is the gravitational acceleration and μ denotes the dynamic viscosity of the fluid (0.0089 Pa s for water). The value of free settling velocity is strongly dependent on higher volumetric concentrations of solids (ϕ); when a cloud of solid particles is settling in a quiescent liquid, additional interactions and hindering effects (i.e. increased drag caused by the proximity of particles) influence its settling velocity. A typical semi-empirical approach known as Richardson-Zaki is based on the power-law function of volume fraction,

$$V_{HS} = V_t(1-\varphi)^n \tag{13}$$

This project has received funding from the European Union's Horizon 2020 research and innovation programme under the Marie Skłodowska-Curie Grant Agreement No. 764902.

where V_{HS} denotes the hindered settling velocity, and n is the function of particle Reynolds number and dilution degree of the suspension: n = 6.5 for $Re_p < 0.2$.

In the present work, the settling period is approximated based on the ultrasound tomographic measurements and is defined as the time interval for a cloud of solid particles to reach from the suspension surface to the plane of the sensors after the mixer is switched off – distance from the suspension surface to the plane of the sensor is approximately 28 mm. A plateau in the measured mean value of the sound speed is obtained after the stirrer is switched off. The initial point of the plateau in the measurement is attributed to the time that solid particles are passing the sensor's plane. The settling period is relatively prolonged as the calcium carbonate concentration increases.

Table 10 presents the calculation of the approximated total settling time of particles in the reactor and the corresponding settling velocity. Even though an accurate experimental procedure is not performed to calculate the settling velocity, the current approach to estimate the settling phenomena from USCT measurement is in good agreement with experimental observations.

Table 10: Estimation of settling velocity of four different concentrations of calcium carbonate particles based on USCT measurement. Total suspension height: 105 mm, sensors height: 77 mm.

$CaCO_3$ concentration, $g\ L^{-1}$	Solid volumetric concentration, %	Settling period (USCT measurement), min	Approximated settling velocity, $mm\ s^{-1}$	Approximated settling time in the reactor, min
8.3	0.31	1	0.46	3.8
16.6	0.61	1.5	0.32	5.5
25	0.91	4.5	0.10	17
33.3	1.22	5	0.09	19

4.6.7. USCT-based tomographic analysis of the calcium carbonate crystallization process

Ultrasound-based tomographic measurement is used to detect localized particle suspensions and monitor the reactive crystallization of the calcium carbonate process according to the chemical reaction. Two instances of the mean value of sound speed are presented in Fig. 82. In all the investigated crystallization experiments, the initial concentration of calcium chloride is 1.6 g L^{-1}; the feed flow rate is 40 ml min^{-1} and the mixing speed is maintained at 100 RPM. The feed solution composition is NaOH at pH 12.1 ± 0.05 and $CO^2{}_3{}^-$ concentration of 0.14 ± 0.02 mol L^{-1}. The tomographic reconstruction in Fig. 83 shows the feeding points and the phase change throughout the process.

Dissemination Level: **Public**

This project has received funding from the European Union's Horizon 2020 research and innovation programme under the Marie Skłodowska-Curie Grant Agreement No. 764902.

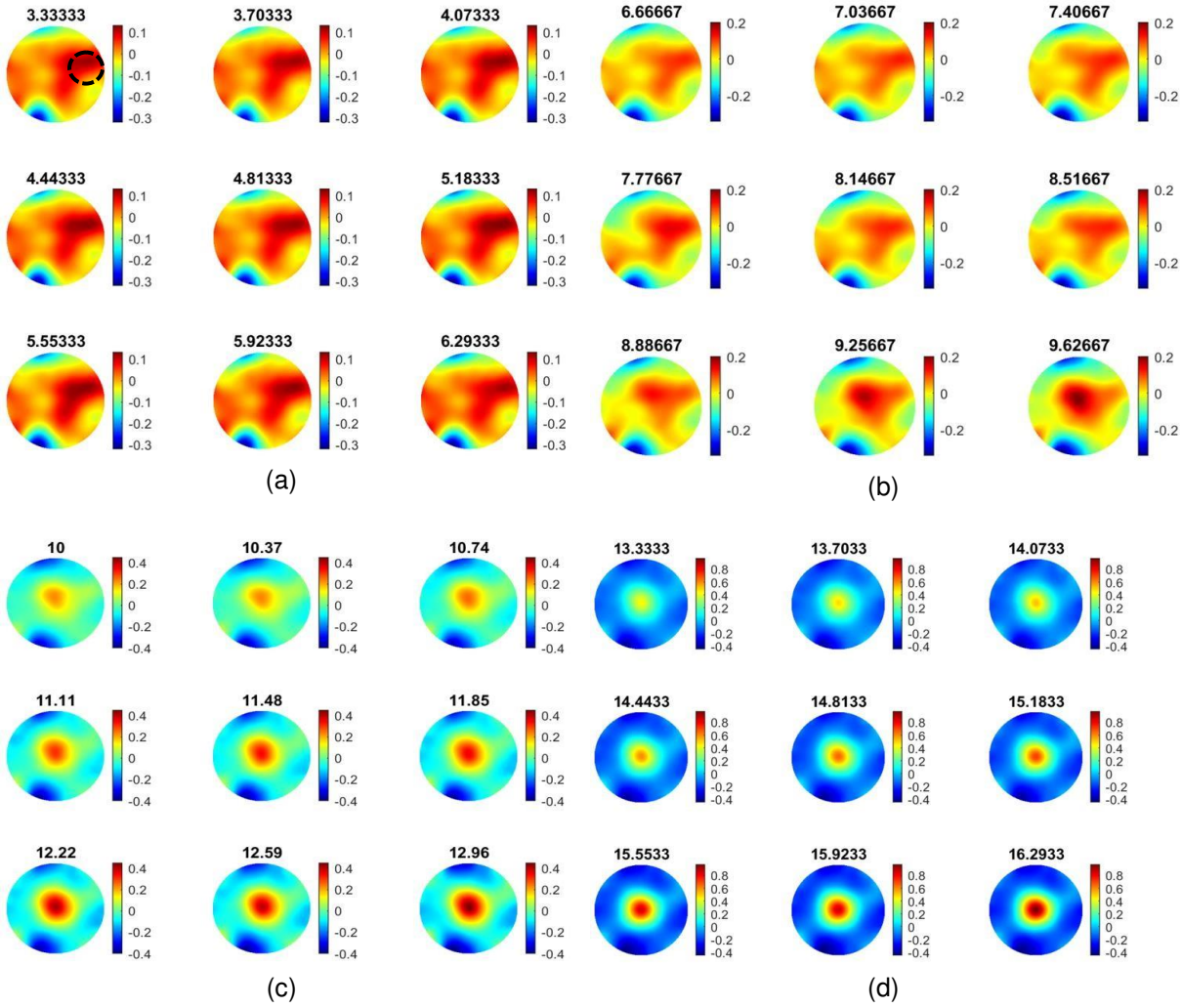

Fig. 82: Ultrasound reconstructions during the calcium carbonate crystallization process. Mixing speed of 100 RPM and feed addition rate of 40 ml. Parts (a) and (b) show the feeding points, and (c) and (d) represent the crystal formation. USCT reconstruction during experiments: (a) from T+ 3.3 min to T+6.2 min; (b) from T+6.6 min to T+9.6 min; (c) from T+10 min to T+12.9 min. (d) from 13.3 min to T+16.2 min.

This project has received funding from the European Union's Horizon 2020 research and innovation programme under the Marie Skłodowska-Curie Grant Agreement No. 764902.

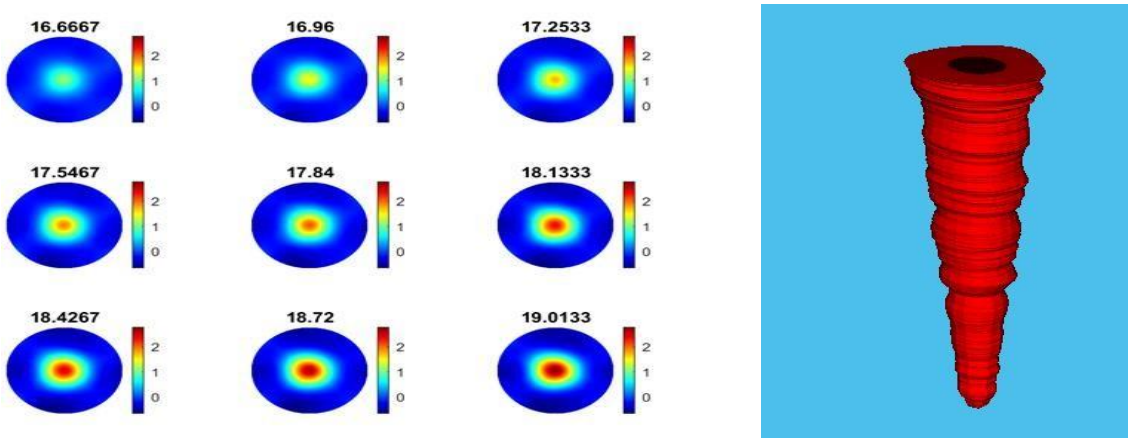

Fig. 83: Evolution of the particle concentration in the later stage of the experiments

In reactive crystallization, the time-of-flight USCT provides useful information on the feeding points and the later stage of the crystal growth. It is less clear to see the start and stop of the mixer and the start and stop of the pump. This may lead to some limitations for the time-of-flight data to be used in malfunction identification and process control. In [14] we have developed a full waveform USCT algorithm considering the acoustic attenuation as well as the time-of-flight data. Indeed, for the amplitude attenuation, the image reconstruction process follows a similar procedure as the transmission time of flight mode USCT. Hence, we do not want to repeat the amplitude attention imaging here.

Fig. 84 (a) and 84 (b) show the mean value of acoustic attenuation $\mathrm{AA} = \left(\frac{1}{\mathrm{fc}}\right)\log\left(\frac{\mathrm{A_{back}}}{\mathrm{A_{full}}}\right)$ dB/MHz for a central excitation frequency of 400 kHz. However, as one can see, the mean value plot for amplitude attenuation shows several clearer points of interest, such as the points that the mixer is switched on (2 minutes) and the pump is switched on (5 minutes), the stop of the stirrer (7.5 minutes) and the start of the stirrer (8 minutes). This suggests that the amplitude attenuation may provide complementary information for future control and malfunction analysis in the crystallization process. Fig. 84 (c) shows the amplitude attenuation reconstruction for similar time steps as Fig. 84. Similar imaging results can be seen between the TOF images and the amplitude attenuation images. A multi-modality USCT and image fusion [14] can then become a useful approach.

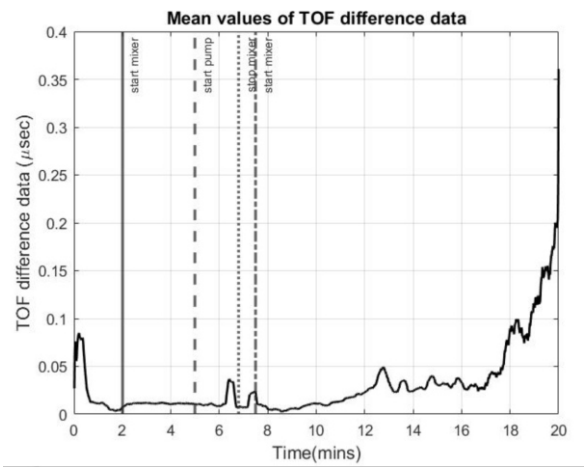

(a)

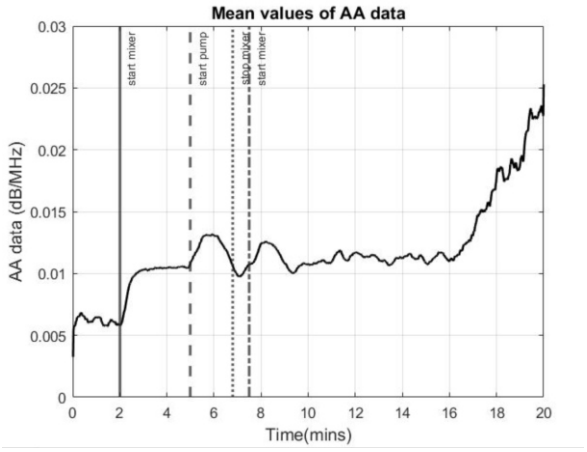

(b)

This project has received funding from the European Union's Horizon 2020 research and innovation programme under the Marie Skłodowska-Curie Grant Agreement No. 764902.

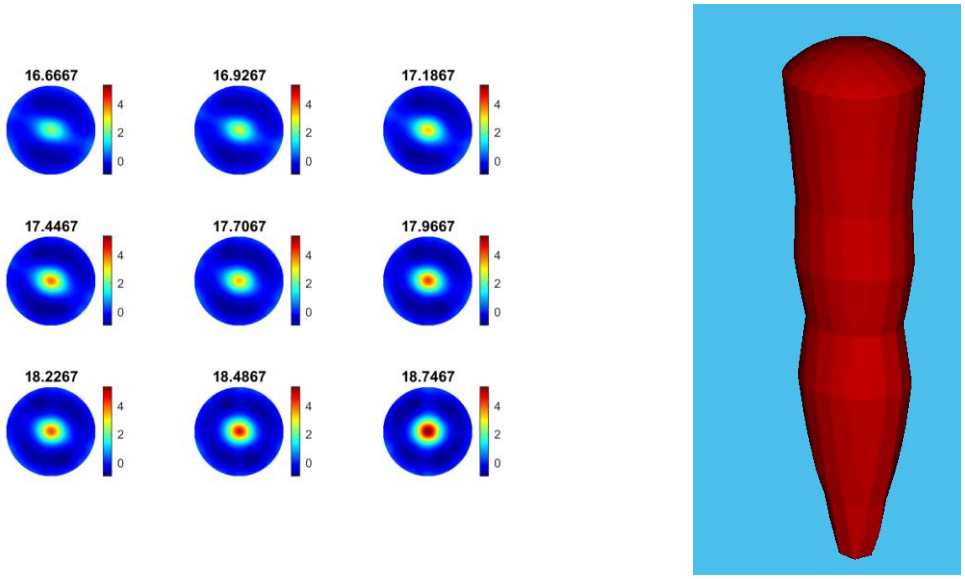

(c)

Fig. 84: (a) Mean value of TOF data. (b) Mean value of acoustic attenuation data (in dB/MHz). In both the cases, mixer on at 2 minutes and pump on at 5 minutes, stop of stirrer at 7.5 minutes and 8 minutes the stirrer starts again. (c) Image reconstruction for amplitude attenuation for time frames as Fig. 69.

4.7. Conclusions and outlook

In the present report, electrical resistance tomography (ERT) and ultrasound computed tomography (USCT) are used to investigate the fast kinetic $CaCO_3$ reactive crystallization process. In the semi-batch crystallization process, calcium chloride is used as a Ca^{2+} source in a stirred tank reactor, and the reagent solution rich in CO_3^{2-} stream is obtained through a carbon-capture process – The idea demonstrates important real-world applicability for carbon dioxide utilization and conversion to calcium carbonate, which has profound industrial importance.

Given that the occurrence of unfavorable faults and malfunctions in the key components of the process stream negatively impacts the final product and results in crystallization failure, the real-time statistical analysis of the electrical currents of the ERT is used to develop an automation program for fault detection and diagnosis (FDD) during the process. It has been shown that failures in the critical process parameters such as mixing, pump and concentrations can be effectively identified by the existing patterns of a single-electrode measurement. Stirrer operational condition is developed based on standard deviation analysis of the incoming signals, while the electrical current slope assessment is used for reporting the pump (feed addition) situation. To ensure a reliable single-electrode operation, experimental repetitions and quantitative analysis of the electrical signals are thoroughly investigated. The accuracy of the measurements in the present study can be further improved upon detailed developments in the utilized software codes and hardware.

Additionally, the USCT system is used to investigate the crystallization process; as a robust non-invasive and non-intrusive tool, USCT measurements and reconstruction provide key insights about bulk particle distribution inside the stirred tank reactor. USCT characterizes the medium by measuring the time of flight of the sound propagation, which represents the delay between the transmission and sound signal acquisition. Experiment with the particle beads offers insights into the system's functionality in high-dynamical scenarios. First, the

Dissemination Level: **Public**

This project has received funding from the European Union's Horizon 2020 research and innovation programme under the Marie Skłodowska-Curie Grant Agreement No. 764902.

efficiency of the utilized USCT system is investigated in detecting localized higher concentrations throughout pouring solid particles inside the stirred tank reactor. Then, quantification is achieved in different concentration tests, which makes it possible to estimate particle settling times. Finally, the USCT tomographs can characterize the particle beads assembling at the central vortex region of the stirred tank reactor. USCT utilization for reactive crystallization monitoring performed well in detecting the injection point of the reagent addition. Also, the real-time measurements of travel-time delays characterized the transient inhomogeneities of the solution.
Although the application of ERT-based tomograph reconstructions in reactive crystallization failed for the reasons stated in the present report, it was possible to develop a fully functional fault detection system using the sensor data. The most sensitive measurement point based on the experimental measurements was selected as sensor data transmitter to fault diagnosis.
Integrating both the ERT and USCT systems in a single reactor during the reactive crystallization process could also provide a potential multi-modality monitoring tool that can be the subject of future investigations. Given that the reaction kinetics is very fast, the effects of the feed addition rate on the resulting ERT/USCT tomographs can be the subject of further experimental studies. Understanding the behavior of the batch operation through experimental repetitions and data quantification is a key to the successful implementation and interpretation of the tomographic instruments.

4.8. References

[1] D. S. Sholl, R. P. Lively, Seven chemical separations to change the world. *Nature*, 532 (2016), https://doi.org/10.1038/532435a.

[2] S. Yu, Y. Zhang, X. Z. Wang, Improved understanding of cefixime trihydrate reactive crystallization and process scale-up with the aid of pat. *Organic Process Research & Development*, 23 (2019), https://doi.org/10.1021/acs.oprd.8b00190.

[3] Y. Yang, Z. K. Nagy, Advanced control approaches for combined cooling/antisolvent crystallization in continuous mixed suspension mixed product removal cascade crystallizers. *Chemical Engineering Science*, 127, pp. 362–373 (2015), https://doi.org/10.1016/j.ces.2015.01.060.

[4] M. A. McDonald, H. Salami, P. R. Harris, C. E. Lagerman, X. Yang, A. S. Bommarius, M. A. Grover, R. W. Rousseau, Reactive crystallization: a review, *Reaction Chemistry & Engineering*, 3 (2021), https://doi.org/10.1039/D0RE00272K.

[5] S. Tapio, M. Jyri-Pekka, W. Johan, Chemical reaction engineering and reactor technology. *Chapman and Hall/CRC*, Boca Raton, FL : CRC Press, Taylor & Francis Group (2019), https://doi.org/10.1201/9781315200118.

[6] W. Zhao, A. Buffo, V. Alopaeus, B. Han, M. Louhi-Kultanen, Application of the compartmental model to the gas-liquid precipitation of CO2 -Ca(OH)2 aqueous system in a stirred tank. *AIChE Journal*, 63, pp. 378–386 (2017), https://doi.org/10.1002/aic.15567.
[7] Y. Qu, J. Cheng, Z.-S. Mao, C. Yang, A perspective review on mixing effect for modeling and simulation of reactive and antisolvent crystallization processes. *Reaction Chemistry & Engineering*, pp. 183–1966 (2021), https://doi.org/10.1039/D0RE00223B.

This project has received funding from the European Union's Horizon 2020 research and innovation programme under the Marie Skłodowska-Curie Grant Agreement No. 764902.

[8] H. Nieminen, L. Järvinen, V. Ruuskanen, A. Laari, T. Koiranen, J. Ahola, Insights into a membrane contactor based demonstration unit for CO2 capture. *Separation and Purification Technology*, 231, 115951 (2020), https://doi.org/10.1016/j.seppur.2019.115951.

[9] S. Aghajanian, H. Nieminen, A. Laari, T. Koiranen, Integration of a calcium carbonate crystallization process and membrane contactor–based CO2 capture. *Separation and Purification Technology*, 274, 119043 (2021), https://doi.org/10.1016/j.seppur.2021.119043.

[10] G. Rao, S. Aghajanian, T. Koiranen, R. Wajman, L. Jackowska-Strumiłło, Process monitoring of antisolvent based crystallization in low conductivity solutions using electrical impedance spectroscopy and 2-D electrical resistance tomography. *Applied Sciences*, 10, 3903 (2020), https://doi.org/10.3390/app10113903.

[11] G. Rao, M. A. Sattar, R. Wajman, L. Jackowska-Strumiłło, Quantitative evaluations with 2d electrical resistance tomography in the low-conductivity solutions using 3d-printed phantoms and sucrose crystal agglomerate assessments. *Sensors*, 21, 564 (2021), https://doi.org/10.3390/s21020564.

[12] P. Koulountzios, T. Rymarczyk, M. Soleimani, Ultrasonic time-of-flight computed tomography for investigation of batch crystallisation processes. *Sensors,* 21, pp. 1-19 (2021), https://doi.org/10.3390/s21020639.

[13] M. L. Buursink, T. C. Johnson, P. S. Routh, M. D. Knoll, Crosshole radar velocity tomography with finite-frequency Fresnel volume sensitivities. *Geophysical Journal International*, 172, pp. 1-17 (2008), https://doi.org/10.1111/j.1365-246X.2007.03589.x.

[14] P. Koulountzios, T. Rymarczyk, M. Soleimani, A Triple-Modality Ultrasound Computed Tomography Based on Full-Waveform Data for Industrial Processes. *IEEE Sensors Journal*, 21 (2021), https://doi.org/10.1109/JSEN.2021.3100391.

[15] H. A. Jakobsen, Agitation and Fluid Mixing Technology. *Chemical Reactor Modeling*, Springer International Publishing, Cham (2014), https://doi.org/10.1007/978-3-319-05092-8_7.

[16] N. Sutudehnezhad, R. Zadghaffari, CFD Analysis and Design Optimization in a Curved Blade Impeller. *International Journal of Chemical Reactor Engineering*, 15 (2017), https://doi.org/10.1515/ijcre-2016-0119.

This project has received funding from the European Union's Horizon 2020 research and innovation programme under the Marie Skłodowska-Curie Grant Agreement No. 764902.